DIGITAL ACCESS TO SCHOLARSHIP AT HARVARD
DASH.HARVARD.EDU

HARVARD LIBRARY
Office for Scholarly Communication

Ice Stream Variability and Links to Climate

Citation

Robel, Alexander Abram. 2015. Ice Stream Variability and Links to Climate. Doctoral dissertation, Harvard University, Graduate School of Arts & Sciences.

Permanent link

http://nrs.harvard.edu/urn-3:HUL.InstRepos:23845475

Terms of Use

This article was downloaded from Harvard University's DASH repository, and is made available under the terms and conditions applicable to Other Posted Material, as set forth at http://nrs.harvard.edu/urn-3:HUL.InstRepos:dash.current.terms-of-use#LAA

Share Your Story

The Harvard community has made this article openly available.
Please share how this access benefits you. Submit a story .

Accessibility

©2015 – Alexander Abram Robel
all rights reserved.

Thesis advisor: Professor Eli Tziperman Alexander Abram Robel

Ice Stream Variability and Links to Climate

Abstract

This dissertation explores the variability and climatic importance of ice streams, regions of fast flow in ice sheets. Observations indicate that ice stream variability plays an important role in the current mass balance of the West Antarctic Ice Sheet and may be related to periods of rapid climatic change in the past, such as Heinrich Events and glacial-interglacial transitions.

We first explore a thermal-regulation mechanism to explain centennial- to millennial-scale ice stream temporal variability based on a simple model which couples ice stream dynamics to subglacial meltwater production. High geothermal heat flux or warm ice surface temperature lead to steady streaming flow, while low geothermal heat flux or cold ice surface temperature lead to thermally-regulated oscillations in ice stream flow. There is a hysteretic transition between these two regimes associated with a subcritical Hopf bifurcation. This simple model can reproduce the time scale and amplitude of ice stream variability associated with Heinrich Events, as well as modern Siple Coast ice streams which appear to be in an oscillatory parameter regime near the transition to a steady-streaming mode.

To understand how this thermally-regulated ice stream variability is manifested at the grounding line, we use a purpose-built flowline model with lateral shear stresses and freely-varying bed properties. Unforced internal variability in ice streams causes rapid migrations in grounding line position with amplitude over 100 km at rates that can exceed 1 km/yr. An ice stream with net positive mass balance may still undergo retreat over a prograde slope due to thinning near the grounding line as part of unforced oscillatory behavior.

Ice streams exhibiting unforced internal variability are far from a steady-state and their behavior cannot be explained with conventional theories of grounding line stability. The grounding line of a stagnant ice stream may persist on a retrograde slope for hundreds to thousands of years before reversing direction on the same slope. This behavior indicates that identifying whether an ice stream is in an oscillatory regime is critical for evaluating whether a grounding line that is observed to retreat onto a retrograde slope is likely to undergo irreversible retreat.

Ice streams may have played a role in the rapid deglaciations which ended past glacial cycles. We use an idealized configuration of a 3D thermomechanical ice sheet model, which explicitly resolves ice streams, to simulate deglaciation in response to a change in climate motivated by Milankovitch forcing. We show that a large ice sheet, which is able to develop ice streams, is more sensitive to a change in climate forcing. This explains why ice sheets experience several precession and obliquity cycles before responding with a full deglaciation only when they reach a sufficiently large size. The rapid deglaciation of large ice sheets is primarily caused by accelerated calving at ice stream marine margins, which is, in turn, caused by enhanced driving stresses in ice stream onset zones. We therefore conclude that accurately resolving ice streams is critical for simulating deglaciations.

Contents

Author List

The following authors contributed to:

- Chapter 1: Alexander Robel
- Chapter 2: Alexander Robel, Eric DeGiuli, Christian Schoof, Eli Tziperman
- Chapter 3: Alexander Robel, Christian Schoof, Eli Tziperman
- Chapter 4: Alexander Robel, Christian Schoof, Eli Tziperman
- Chapter 5: Alexander Robel, Eli Tziperman
- Chapter 6: Alexander Robel
- Appendix A: Alexander Robel, Eric DeGiuli, Christian Schoof, Eli Tziperman
- Appendix B: Alexander Robel, Christian Schoof, Eli Tziperman

Listing of figures

This work is dedicated to my grandparents.

Acknowledgments

This dissertation and the completion of my doctorate would not have been possible without the support of many, many people. Thanks to Eli, who convinced me to switch from the tropics to the poles and from short to long (climatic) time scales. Your advice, good humor and enthusiasm have made this entire dissertation possible and set me on a path towards (hopefully) being a creative and conscientious scientist, like yourself. Also thanks to Christian, my co-advisor and ice dynamics lifeline for reading a thousand revisions and providing a West Coast home for me in Vancouver. Thanks to current and former members of my committee: Jim Rice, Rick O'Connell, Peter Huybers and Jerry Mitrovica for advice and guidance along the way. To past advisors, teachers and professors who brought me to this point in my career: David Enfield, Wafa Khalil, Julie Hood, Dana Yancoskie, Gabi Hegerl, Joshua Socolar and a huge, HUGE thanks to Susan Lozier.

To the administrative staff of EPS for making the process of starting and finishing a PhD smooth (as can possibly be hoped). Thanks to the Duke Endowment, the Mellon-Mays Foundation, Harvard University, the National Defense Science and Engineering Graduate Fellowship and the National Science Foundation Graduate Research Fellowship for funding my undergraduate and graduate educations.

A BIG thanks to my peers and friends in and outside of EPS for walking down this road with me. Thank you to my grandparents, who fought hard so that I could have this opportunity. To my parents and sister, who taught me the values of hard work, resilience and inquisitiveness. And to Danielle, who made this journey ten times lighter and with whom I cannot wait to go on a hundred more journeys.

1

Introduction

Land ice forms where a persistent accumulation of snow compacts over time. Ice flows down gradients of ice surface elevation, until removed either by surface melting or calving (breaking into icebergs) into the ocean. Historically, it had been thought that flow in ice sheets transported ice from accumulation regions in the continental interior to ablation regions near the marine margin via slow (1-10 m/yr) deformational flow. Beginning in the 1950's, field observations (Swithinbank, 1954) made it clear that there are regions where ice flows at much higher velocities (100-1000 m/yr) primarily through sliding at the base. These "ice streams" have become a major focus of glaciological research as they are responsible for most of the transport of ice mass within ice sheets (Bamber et al., 2000). Subsequently, it has been shown through satellite and geological observations that ice streams are present and widespread within both modern and past continental-scale ice sheets (Stokes and Clark, 2001; Rignot et al., 2011b). The purpose of this thesis is to investigate temporal variability of ice stream flow due to internal thermal regulation of subglacial meltwater production (chapters 2-4) and external forcing associated with orbital variations (chapter 5).

Almost all large-scale ice flow on the Earth's surface can be represented as an incompressible Stokes flow where inertial and rotational terms are small compared to viscous terms and density is approximately constant, shown here in expanded form,

$$\frac{\partial}{\partial x}\left(\nu_{eff}\frac{\partial u}{\partial x}\right)+\frac{\partial}{\partial y}\left(\nu_{eff}\frac{\partial u}{\partial y}\right)+\frac{\partial}{\partial z}\left(\nu_{eff}\frac{\partial u}{\partial z}\right)=\frac{\partial p}{\partial x} \tag{1.1}$$

$$\frac{\partial}{\partial x}\left(\nu_{eff}\frac{\partial v}{\partial x}\right)+\frac{\partial}{\partial y}\left(\nu_{eff}\frac{\partial v}{\partial y}\right)+\frac{\partial}{\partial z}\left(\nu_{eff}\frac{\partial v}{\partial z}\right)=\frac{\partial p}{\partial y} \tag{1.2}$$

$$\frac{\partial}{\partial x}\left(\nu_{eff}\frac{\partial w}{\partial x}\right)+\frac{\partial}{\partial y}\left(\nu_{eff}\frac{\partial w}{\partial y}\right)+\frac{\partial}{\partial z}\left(\nu_{eff}\frac{\partial w}{\partial z}\right)=\frac{\partial p}{\partial z}+\varrho g \tag{1.3}$$

$$\nabla\cdot\vec{u}=0 \tag{1.4}$$

where (u, v, w) are components of the velocity field, ν_{eff} is the effective ice viscosity, p is pressure and the ϱg is gravitational driving. The constituitive relationship for glacial ice was deduced by Glen

through laboratory experiments and later generalized by Nye (Glen, 1955; Nye, 1957),

$$\dot{\varepsilon}_{jk} = A\tau_E^{n-1}\tau_{jk} \tag{1.5}$$

where $\dot{\varepsilon}$ is the strain rate, τ is stress, n is an empirical flow law exponent, A is a flow parameter that is a function of temperature and other material ice properties and τ_E is the second invariant of the stress tensor. This constitutive relationship shows that one component of strain is coupled to the other components through the strain invariant, leading to an estimate of the effective viscosity,

$$\nu_{eff} = A^{-\frac{1}{n}} \left(\frac{1}{2} \left[\left(\frac{\partial u}{\partial x} \right)^2 + \left(\frac{\partial v}{\partial y} \right)^2 + \left(\frac{\partial w}{\partial z} \right)^2 \right] + \left(\frac{\partial u}{\partial z} \right)^2 + \left(\frac{\partial u}{\partial y} \right)^2 + \left(\frac{\partial v}{\partial z} \right)^2 \right)^{\frac{1-n}{2n}}. \tag{1.6}$$

Under further conditions, the Stokes flow equations can be simplified to find approximate solutions for ice velocity fields. One classical approach is to assume that horizontal velocities dominate, ice is frozen to the bed and the vertical shear on the horizontal velocity dominates other shear components. The resulting creep flow solution is referred to as the shallow-ice approximation (Fowler and Larson, 1978; Greve and Blatter, 2009) and it is still widely used as a simple, efficient model for certain types of glacial flow. Alternately, if the transverse shear of the horizontal velocity dominates other shear components and there is slip at the bed, the result is the shallow shelf approximation (Morland, 1987; MacAyeal, 1989). This "plug flow" simplification of the Stokes equations has more recently been used as a model for ice shelf flow.

Deriving a comprehensive theory for ice flow on the Earth's surface has been greatly complicated by ice sliding over the bed, and particularly by the basal sliding of ice streams. An active ice stream is a region of fast plug flow, similar to an ice shelf, embedded within a region of slow creep flow. Thus, neither the shallow ice nor the shallow shelf approximation can completely describe an ice sheet with embedded ice streams. Numerical strategies for joining the shallow ice and shallow shelf

approximations have been proposed to model ice sheets with ice streams (Bueler and Brown, 2009). However, further mathematical and numerical innovations are required as observations continue to reveal additional complexities of ice stream flow, such as margin migration (Schoof, 2012b) and deformation-induced melting in shear margins (Suckale et al., 2014; Perol and Rice, 2015).

One complication presented by ice streams is their seeming separation into two different classes. "Topographic" ice streams are constrained by bed topography and exhibit fast flow due to high gravitational driving and some lubricated basal slip. The Greenland Ice Sheet rests atop hard bedrock with strong topographic variation and so has many topographic ice streams, otherwise known as "outlet glaciers". Conversely, "pure" ice streams have low driving stresses and exhibit fast high basal velocities (typically) due to the presence of deforming water-filled subglacial till. The West Antarctic Ice Sheet rests atop a low-slope, deforming bed and so is drained by many pure ice streams (Figure 1.1). At a location referred to as the "grounding line", ice streams have thinned sufficiently to reach flotation and they flow into floating ice shelves. It is at this point that land ice begins to contribute to global mean sea level.

1.1 Observations and theories of ice stream temporal variability

Observational evidence indicates that ice stream flow exhibits significant temporal variability on time scales ranging from days to millennia. At short time scales (fortnightly), some ice streams are observed to exhibit flow variability associated with tidal flexure of ice shelves (Gudmundsson, 2006; Tsai and Gudmundsson, 2015). At longer time scales (sub- to interannual) variations in bed properties due to the filling and drainage of subglacial cavities (Winberry et al., 2009) and subglacial lakes (Fricker et al., 2007) can produce transient changes in ice stream flow speed (Stearns et al., 2008). Stick slip behavior associated with sub-ice stream "sticky spots" has also been observed in Whillans Ice Stream, with modulation by tidal forcing (Bindschadler et al., 2003) and measured through the

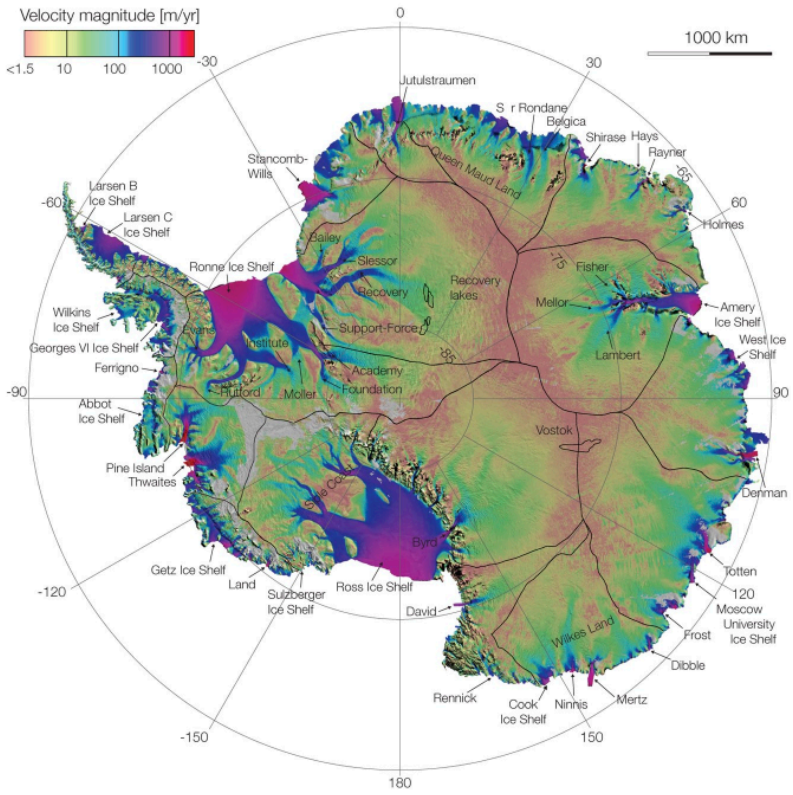

Figure 1.1: Surface ice velocities of the Antarctic Ice Sheet from Rignot et al. (2011a), derived from a composite of satellite radar interferometry, overlaid on a MODIS mosaic of the Antarctic Ice Sheet and colored on a logarithmic scale. Black lines indicate major ice divides.

generation of local seismic activity (Tsai et al., 2008).

Ice stream flow variability on time scales of centuries to millennia has a significant impact on the long-term mass balance of ice sheets (Wingham et al., 1998; Joughin and Tulaczyk, 2002; Pritchard et al., 2009) and a potentially important influence on climate (Hemming, 2004; Alley and Clark, 1999). Retzlaff and Bentley (1993) provided the first direct evidence of such variability, in finding buried crevasses in the relict shear margin of currently stagnant Kamb Ice Stream in the Siple Coast region of the West Antarctic Ice Sheet. These crevasses indicate that the shear margin, and by extension the ice stream, were active as recently as 150 ± 25 years before present. In a series of integrated data-model studies, Hulbe and Fahnestock (2004, 2007) were able to infer from streaklines on the Ross Ice Shelf that multiple ice streams in the Siple Coast region have switched between active and stagnant flow states in the past 1000 years. Indirect geomorphological evidence also indicates that paleo-ice streams in many of the major ice sheets exhibited flow variability on time scales of hundreds to thousands of years (Stokes and Tarasov, 2010; Winsborrow et al., 2012; Stokes et al., 2012; Kleman and Applegate, 2013; Margold et al., 2015). Perhaps the most prominent example of ice stream variability are Heinrich events, periods of increased iceberg discharge in the North Atlantic linked to the Hudson Strait Ice Stream, which is hypothesized to have dominated ice flow in the northeastern portion of the Laurentide Ice Sheet during the last glacial period (Hemming, 2004).

Many physical mechanisms have been proposed to explain observations of centennial- to millennial-scale ice stream variability (for review, see Bennett, 2003). Switching of subglacial drainage network configuration is thought to be the cause of surging in many mountain glaciers (Kamb et al., 1985) and thus studies (Rose, 1979) have attempted to draw an analogy with ice streams. However, limited observations of drainage networks beneath ice streams exist and the duration of hydraulic surges tend to be very different than those inferred for ice stream active periods (Anandakrishnan et al., 2001). A triple-valued law for glacier sliding will also cause oscillations in the flow of mountain glaciers and ice stream, as shown in numerical models (Fowler and Johnson, 1996; Sayag and

Tziperman, 2009). Other studies of ice stream variability have focused on the potential interaction between adjacent ice streams. In some numerical simulations of ice streams, the transient capture of an ice catchment by one ice stream chokes off the supply of mass to nearby ice streams (Payne and Dongelmans, 1997; Sayag and Tziperman, 2011) and may consequently lead to apparent ice stream spatiotemporal variability (though there is no regularity in the recurrence). A similar theory focuses on the capture of a catchment of subglacial meltwater production due to subtle changes in ice surface topography (Anandakrishnan and Alley, 1997). However, the available observational evidence seems to indicate that adjacent variable ice streams can remain active simultaneously while sharing a single upstream mass source (Joughin et al., 1999). These theories also fail to explain the potential for variability of a single ice stream (e.g. the Hudson Strait Ice Stream).

Thermally-regulated surging is perhaps the most prominent theory for centennial to millennial scale variability in ice streams (and decadal-scale variability in mountain glaciers). The essential idea is that meltwater production at the bed is regulated by ice thickness through vertical conduction of heat and the advection of cold ice from the surface. When the glacier is thick, the bed is insulated, meltwater is produced and velocity increases. Increasing velocity increases frictional heating, which produces meltwater, further weakening the bed and increasing velocity, in a positive feedback loop. High velocities cause the ice sheet to thin, increasing vertical heat conduction, which decreases meltwater production at the bed and eventually leads to the end of the surge. This mechanism has roots that extend back to Forel's (1895) observation that mountain glacier variations are accompanied by displacement of the 0°C isotherm. Robin (1955) later formalized this into a theory for the cyclical nature of surges involving onset through a creep instability. It was subsequently shown that the creep instability mechanism for surge activation was unnecessary (Hoffmann and Clarke, 1973) and that cold glacier thermal surging could be explained simply by appealing to surface accumulation (Clarke, 1976). This thermal mechanism has since been shown to occur in a wide range of ice stream and ice sheet models (Oerlemans, 1982a; Fowler, 1987; MacAyeal, 1993; Payne, 1995; Bougamont

et al., 2011; Dunse et al., 2011; Van Pelt and Oerlemans, 2012; van der Wel et al., 2013) and observations (Bindschadler et al., 1976; Jiskoot et al., 2000), producing oscillations in flow velocity and ice thickness.

In this dissertation, we first describe and analyze a simple theory for thermally-regulated ice stream temporal variability. Then, in a more complex flowline model, we show how such unforced ice stream variability causes rapid migrations of the grounding line. These results then provide a useful framework through which to understand the behavior of earlier numerical model studies and to interpret glaciological and geological observations of ice stream variability.

1.2 Ice sheet feedbacks and instabilities

This dissertation is also concerned with the role of ice streams in ice sheet stability and variability. Large continental ice sheets have waxed and waned as a major feature of the Earth's surface during the past 30 million years. During the last glacial period, the Laurentide Ice Sheet and (to a lesser extent) the Patagonian and Eurasian Ice Sheets composed a significant portion of the land ice on the Earth's surface. Since the end of the last glacial period, approximately 12,000 years ago, almost all of Earth's land ice has been found in the Antarctic and Greenland Ice Sheets. The deglaciation from the glacial to the current interglacial period included a significant change in global climate which coincided with melting of the Laurentide, Eurasian and Patagonian ice sheets and global mean sea level rise of approximately 120-130 meters (Bard et al., 1990; Austermann et al., 2013).

Many processes besides ice streams have been proposed to contribute to glacial cycles and specifically to deglaciations. Perhaps the most prominent theory involves Milankovitch forcing, which is known to pace glacial cycles (Hays et al., 1976; Hyde and Peltier, 1987; Gildor and Tziperman, 2000; Tziperman et al., 2006). However, Milankovitch forcing cannot explain the asymmetry between slow glaciation and rapid deglaciation or the 100-kyr periodicity of glacial cycles (since the

mid-Pleistocene transition), with deglaciation only occurring after ice sheets have experienced several precession and obliquity cycles (Imbrie et al., 1993). Consequently, it is thought that amplifying feedbacks within the cryosphere-climate-Earth system must also play an important role in producing glacial cycles. A variety of climate processes were cited as being the critical feedback in simulations of glacial-interglacial cycles, including the ice-albedo feedback (Budyko, 1969), thermohaline circulation instabilities (Broecker and Denton, 1989), CO_2 ventilation from the deep ocean (Toggweiler, 1999), atmospheric dust loading (Peltier and Marshall, 1995), sea ice effects on accumulation (Gildor and Tziperman, 2000), and isostatic adjustment of the Earth surface (Pollard, 1982; Oerlemans, 1980; Abe-Ouchi et al., 2013).

One well-studied ice sheet process that plays a prominent role in this dissertation is the height-mass balance feedback, wherein a lowering of ice surface elevation increases surface melting and causes further surface lowering. This feedback can amplify secular changes in ice sheet mass balance and lead to a new equilibrium or can lead to a runaway instability and complete ice sheet collapse (Weertman, 1961; Oerlemans, 2003; Gregoire et al., 2012). Consequently, many theories of glacial-interglacial cycles rely on the height-mass balance feedback as a large amplifier of climatic changes during abrupt deglaciation (Pollard, 1978; Oerlemans, 1980; Abe-Ouchi et al., 2013).

There are also internal dynamical processes within ice sheets which can lead to rapid deglaciation. Early concerns arose over the stability of the West Antarctic Ice Sheet, from evidence that it may have been considerably smaller during past warm periods in Earth's history (Mercer, 1968), is currently out of equilibrium and disintegrating (Hughes, 1973), and perhaps close to a threshold leading to a collapse (Mercer, 1978). Theoretical work by Weertman (1974) showed that a thick, unbuttressed ice sheet resting on a rigid bed with either a flat or retrograde slope (upward in the direction of flow) was inherently unstable. This "marine ice sheet instability" (so-called because marine ice sheets resting below sea level tend to have retrograde slopes) may be one candidate for initiating rapid deglaciation. Studies utilizing numerical models with accurate representations of the ground-

ing line have since argued that major arteries of Antarctic ice flow, such as Pine Island and Thwaites glaciers, are susceptible to an irreversible retreat (Favier et al., 2014; Joughin et al., 2014). However, Weertman's (1974) instability does not seem to have been a major player in the rapid Laurentide deglaciation, with only limited evidence to the contrary (Briner et al., 2009). Recent numerical modeling and observations also indicate that ice streams may slowly retreat or achieve stability on retrograde slopes under certain conditions (Alley et al., 2007; Gomez et al., 2010a; Jamieson et al., 2012). Consequently, though the marine ice sheet instability has the potential to cause rapid deglaciation, there is still no consensus on its precise limitations or applicability.

In this dissertation, we explore how unforced ice stream variability leads to grounding line behavior that is not explained by conventional theories of grounding line stability on retrograde slopes. When temporal variations in bed properties cause ice streams to fluctuate far from a steady-state, they can persist on retrograde slopes for long periods of time. Understanding the range of behaviors made possible by allowing variable bed properties is key to assessing the potential for irreversible grounding line retreat in ice streams currently undergoing rapid change.

There is also strong evidence that ice streams played a role in the final deglaciation of the Laurentide. In this dissertation we will explain how ice stream dynamics contribute to the deglaciation in response to climate forcing motivated by orbital variations. Indeed, Marshall and Clark (2002) argued that gradual warming of the bed led to widespread temperate basal conditions ideal for ice stream formation near the end of the growth of the Laurentide Ice Sheet during the last glacial period. Subsequent observations have suggested that ice streams participated in setting temporal and spatial structure of the deglaciations of both Laurentide (Stokes and Tarasov, 2010; Stokes et al., 2012; Margold et al., 2015) and Eurasian (Winsborrow et al., 2012) ice sheets. Despite these suggestions of the potential role of ice streams in glacial cycles, current theories rely on much oversimplified representation of ice dynamics and nearly completely ignore ice streams.

This dissertation is organized as follows. In chapter 2, we describe and analyze a simple mech-

anism for ice stream temporal variability, involving thermal regulation of subglacial melt water production. We show that a corresponding simple model matches the behavior of more complex models and observations of past and ongoing ice stream variability. In chapter 3, we explore how ice stream variability is manifested at the grounding line. We use a purpose-built ice stream flowline model with freely-varying temperature and till water content. Ice stream activation initiates rapid grounding line excursions of over 100 km at migration rates exceeding 1 km/yr. We discuss the implications of such rapid migration for interpreting glaciological and geomorphological indicators of past grounding line positions. In chapter 4, we demonstrate how temporal variation in bed properties lead to ice stream behavior that is not explained by conventional theories of grounding line stability. An ice stream exhibiting unforced variability may persist on a retrograde slope before reversing direction of migration on that same slope. Such behavior must be considered as a possibility when evaluating potential evidence for irreversible grounding line retreat in present-day ice stream observations. In chapter 5, we explore the role of ice streams in deglaciations. Using an idealized configuration of a complex 3D thermomechanical ice sheet model, we show how ice stream acceleration is triggered by climate forcing motivated by orbital variations, and plays an important role in the rapid deglaciation of large ice sheets. Small, cold ice sheets and ice sheets without properly resolved ice streams respond more weakly to such Milankovitch-motivated forcing, indicating that ice streams are an important amplifying feedback in producing rapid deglaciations of large ice sheets. In chapter 6, we offer some concluding thoughts.

2

Modes, Scales and Hysteresis of Ice Stream Temporal Variability

2.1 Introduction

Ice streams are regions of ice sheets that flow 2-3 orders of magnitude faster than typical glacial ice and currently account for over 90% of the mass flux from the interior of the Antarctic ice sheet to the margins, though covering less than 5% of its total area (Bamber et al., 2000). The variability of ice stream flow on time scales of tens to thousands of years plays an important role in determining ice sheet mass balance. Observations indicate that the stagnation of Kamb Ice Stream 150 years ago (Retzlaff and Bentley, 1993) may be the primary cause for the currently positive mass balance in West Antarctica (Joughin and Tulaczyk, 2002). Further geological evidence has suggested that other Siple Coast ice streams have exhibited considerable variability in the last 1000 years (Hulbe and Fahnestock, 2007; Catania et al., 2012). The ongoing slowing of Whillans Ice Stream (Hulbe and Whillans, 1997) and the possibility of reactivation of Kamb Ice Stream (Vogel et al., 2005) suggest that ice stream variability will continue to have a major influence on ice sheet mass balance and global rates of sea level rise over the next several centuries.

The variability of a Hudson Strait Ice Stream has been implicated as a main factor in Heinrich events, large periodic ice discharge events from the Laurentide ice sheet during the last glacial period (Heinrich, 1988). Current geochemical estimates of Heinrich event characteristics (Hemming, 2004) are sufficiently broad to suggest that Heinrich event modeling may be useful in constraining the record. Studies of IRD provenance indicate that Heinrich layers in North Atlantic sediment cores point to Hudson Strait ice stream variability as the ice source (Hemming, 2004). Further geological evidence (Andrews and Maclean, 2003) suggests the Hudson Strait Ice Stream was similar to modern Siple Coast ice streams (though on a much larger scale), indicating that both may share a single mechanism of variability.

The simple model described in this study can be useful as a guide for such complex model stud-

ies in picking an appropriate parameter regime and constructing a reasonable ice stream geometry. MacAyeal (1993) constructed a relaxation oscillator model of the entire Laurentide ice sheet by exploiting its characteristic binge and purge time scales and without explicitly considering the possibility of a Hudson Strait Ice Stream. MacAyeal (1993) was successful in reproducing observed Heinrich event period, but had to assume a characteristic ice stream purge time scale of approximately 250 years. Since our model explicitly simulates ice stream dynamics, we are able to predict key parameters of interest, such as purge time scale, till freeze-on thickness and basal cooling amplitude. Marshall and Clarke (1997) explicitly simulate the Laurentide ice sheet and a hypothetical Hudson Strait Ice Stream using a complex model, but were not able to reproduce discharge within the wide range of proxy records. Other studies (Calov et al., 2002, 2010) have also attempted to reproduce the period and amplitude of Heinrich ice discharge events, but cite the need for evolving drainage and till mechanics in order to gain a full understanding of the physical processes that cause Hudson Strait Ice Stream variability.

High ice stream velocities are caused by the deformation of meltwater-saturated, weak subglacial till (Alley et al., 1986; Blankenship et al., 1986; Engelhardt et al., 1990). In Antarctica, this meltwater originates at the ice-bed interface, which is maintained at the pressure-melting point during the active ice stream phase. The resulting weak bottom stress is complemented by lateral stresses at ice stream margins in resisting the weak driving stress typical of Antarctic ice streams (Echelmeyer et al., 1994; Jackson and Kamb, 1997). Changes in the strength of subglacial till shift the balance of resistive stresses and may significantly alter ice stream velocity (van der Veen and Whillans, 1996). Observations also indicate that drainage conduits at the ice-bed interface may provide a means for transporting locally produced meltwater over long distances (Engelhardt and Kamb, 1997; Winberry et al., 2009), significantly complicating the problem of modeling ice stream hydrology and dynamics.

The complexities of ice stream dynamics have been modeled using a diverse array of approaches. Tulaczyk et al. (2000b) used a highly reduced model and found that multiple modes of ice stream

flow are possible, depending on the subglacial net heat flux and changes in subglacial production of meltwater. Complex models often incorporate parameterizations of observed small scale phenomena, such as drainage networks. Two studies (Bougamont et al., 2003a,b) coupled a flow band model to a simple hydrology model similar to that of Tulaczyk et al. (2000b). Another study (van der Wel et al., 2013) coupled a flow band model to both simple local hydrology and a dynamic drainage model. Similarly, Bougamont et al. (2011) (hereafter B11) coupled a complex Herterich-Blatter-Pattyn ice model (Herterich, 1987; Blatter, 1995; Pattyn, 2002) to a simple hydrology model. This later study found that sustained oscillatory ice stream behavior was not attainable without a seemingly ad-hoc supply of water from a parameterized regional drainage network. Related complex model studies of hydrology beneath ice sheets (Payne, 1995; Dunse et al., 2011; Van Pelt and Oerlemans, 2012) have found that multiple distinct modes of ice sheet flow exist depending on the state of the subglacial thermal heat budget. Sayag and Tziperman (2009) showed that the spatial structure of ice streams suggests a multi-valued sliding law. Prescribing such a law, they then (Sayag and Tziperman, 2011) found either oscillatory or steady-streaming modes, depending on the rate of upstream ice supply. However, they did not explicitly include the physics that lead to the prescribed sliding law.

This paper studies the interaction of ice stream dynamics, basal hydrology and thermal processes to understand the physical conditions that may give rise to and modulate ice flow variability on a range of time scales. We build a simple model, described in the next section, to simulate the subglacial heat budget, the resulting production or consumption of meltwater and its impact on till deformation. Our central aim is to explore possible ice stream behaviors and their dependence on physical parameters.

We make a number of key improvements to earlier simple models (Tulaczyk et al., 2000b; MacAyeal, 1993) while retaining the simplicity that permits a wide range of parameter experimentation and analytic approaches. In particular, this model allows both ice thickness and meltwater content to vary, resulting in a triple-valued flux relationship that has been shown to lead to surfing behavior (Fowler,

1987; Fowler et al., 2001). We also allow for the possibility of till freeze-on and basal ice cooling during stagnant intervals of till overconsolidation, altering the subglacial heat flux. If till becomes saturated, drainage is permitted and may have a significant impact on the final equilibrium that would otherwise not be reached in the absence of drainage.

The resulting ice stream flow evolution includes two regimes, a steady-streaming mode and a binge-purge mode. These modes are qualitatively similar to the modes found first by Payne (1995), and later in other studies with a complex ice sheet models (Sayag and Tziperman, 2009, 2011; Dunse et al., 2011; Van Pelt and Oerlemans, 2012). In some of these studies, subglacial hydrology is parameterized with ad-hoc sliding parameters, which are then varied in order to demonstrate that there are multiple possible modes of ice sheet behavior, including high- and low-frequency cyclicity and steady flow. In this study, we focus on ice stream-like geometry and explicitly simulate till mechanics and the basal heat budget, which obviates the need for either ad-hoc parameterizations or poorly constrained empirical sliding laws. The flow mode is determined by the balance between different sources of heating and cooling at the ice-bed interface and meltwater drainage. This provides a general framework to interpret the special cases of other simple and complex model studies in terms of readily-measurable physical parameters like geothermal heat flux and ice surface temperature.

Additionally, the nature of the transition between these two modes is not always smooth, taking the form of a subcritical Hopf bifurcation. In short, a supercritical Hopf bifurcation occurs when variation of a parameter causes a system to smoothly change from steady state to to an oscillating equilibrium state of infinitesimal amplitude. In a subcritical Hopf bifurcation, variation of a parameter causes a system to change from steady state to an oscillating equilibrium state of large amplitude (Strogatz, 1994). In our model, the occurrence of this type of bifurcation produces hysteresis in cases that may have important implications for climate-ice stream interactions.

2.2 Model description

We model an ice stream as a single lumped spatial element in order to focus on temporal (rather than spatial) evolution. All spatial derivatives are approximated using finite-differencing over the spatial scales of interest. The model domain is a rectangle of length L in the streamwise x-direction, corresponding to the entirety of the ice stream trunk, and width W in the cross stream y-direction, corresponding to ice stream width between shear margins. We assume that $\frac{W}{L} \ll 1$, and that vertical shear contributes negligibly to ice stream velocity. The velocity field in the ice stream is determined by lateral and basal shear stress balancing the driving stress acting on an ice stream cross-section. To obtain a spatially-lumped model, we then assume that a single velocity can be used to represent ice discharge from the ice stream (Raymond, 1996, 2000).

The model describes the rate of meltwater production at the ice-bed interface, which evolves in response to ice and till dynamics, and may activate different physical processes depending on the till state. Section 2.2.1 describes the ice thickness evolution equation, followed by the meltwater budget in section 2.2.2, ice sliding velocity in section 2.2.3 and till and basal ice properties in section 2.2.4. For values of all constants referenced hereafter and used to generate all figures (unless otherwise noted), see Table 2.1.

2.2.1 Ice stream thickness

Changes in ice stream thickness are the result of a balance between accumulation from snowfall and removal due to ice stream velocity

$$\frac{dh}{dt} = a_c - \partial_x \left(u_b h \right) , \tag{2.1}$$

Constant	Description	Value
a'	Till empirical coefficient (Pa)	1.41×10^6
a_c	Accumulation rate ($m \cdot yr^{-1}$)	0.1
A_g	Glen's law rate factor ($Pa^{-3} \cdot s^{-1}$)	5×10^{-25}
b	Till empirical exponent	21.7
C_i	Volumetric heat capacity of ice ($J \cdot K^{-1} \cdot m^{-3}$)	1.94×10^6
e_c	Till consolidation threshold	0.3
g	Acceleration due to gravity ($m \cdot s^{-2}$)	9.81
h_b	Thickness of temperate ice layer (m)	10
k_i	Thermal conductivity of ice ($J \cdot s^{-1} \cdot m^{-1} \cdot K^{-1}$)	2.1
L	Ice stream trunk length (km)	500
L_f	Specific latent heat of ice ($J \cdot kg^{-1}$)	3.35×10^5
n	Glen's law exponent	3
W	Ice stream trunk width (km)	40
w_s	Till saturation threshold (m)	1
Z_s	Initial effective till layer thickness (m)	1
ϱ_i	Ice density ($kg \cdot m^{-3}$)	917
ϱ_w	Water density ($kg \cdot m^{-3}$)	1000

Table 2.1: Parameters used in this study (unless otherwise indicated)

When discretized for an ice stream with no flow entering at the upstream end, the resultant balance is

$$\frac{dh}{dt} = a_c - \frac{u_b h}{L}, \tag{2.2}$$

where a_c is the constant accumulation rate and u_b is the basal sliding velocity. The second term on the right-hand side of this equation is an approximation of ice flux divergence, $\frac{\partial}{\partial x}(u_b h)$, assuming that sliding velocity vanishes at the upstream boundary and thickness is spatially uniform within the domain. Ice flux from upstream tributaries is assumed to be negligible. Basal melting and freeze-on are small compared to accumulation and ice flux, and so are neglected from this mass balance.

2.2.2 Meltwater budget

When the temperature of the bed, T_b, is at the melting point, $T_b = T_m$, the bed can have a non-zero water content w. This is related to the bed void ratio e through $w = eZ_s$, where Z_s is the thickness

that unfrozen till would occupy if it were reduced to zero porosity. When $w > 0$, it evolves according to

$$\frac{dw}{dt} = m - \frac{Q_d}{LW} \tag{2.3}$$

where m is basal melt rate and Q_d is the volumetric discharge rate through all subglacial conduits below the ice stream. In this model, w and Z_s are dynamically evolved and $e = \frac{w}{Z_s}$ is calculated diagnostically.

m can be related to geothermal heat flux G, conduction into the ice and heat dissipated by sliding at the bed (as in Lingle and Brown, 1987; Tulaczyk et al., 2000b; Joughin et al., 2004)

$$m = \frac{1}{\varrho_i L_f}\left[G + \frac{k_i\left(T_s - T_b\right)}{h} + \tau_b u_b\right], \tag{2.4}$$

where T_s is the prescribed ice surface temperature, T_b is the basal temperature, k_i is the thermal conductivity of ice, τ_b is the basal shear stress so that $\tau_b u_b$ represents frictional heating, while ϱ_i is the density of glacial ice and L_f is the latent heat of fusion. Negative m corresponds to the freezing of basal water. Vertical heat conduction here is a discretized version of $k_i \partial_z T$ at the bed, assuming that vertical ice temperature variations are linear from the basal ice temperature to the prescribed surface temperature. Corrections to this approximation would likely result in a larger vertical temperature gradient near the bed (Joughin et al., 2004).

When w reaches zero from above, both u_b and the frictional heating term in the expression for m are set to zero as all the till is frozen and basal temperature may drop below T_m. Additionally, when $w = 0$, $T_b = T_m$ and $m = G + \frac{k_i(T_s - T_m)}{h} > 0$ then till begins to thaw and $\frac{dw}{dt} = m$.

When the till water content exceeds an upper saturation threshold (w_s), we assume that till has

become saturated and all additional production of meltwater goes directly into drainage,

$$Q_d = \begin{cases} 0 & \text{if } w < w_s \text{ or } m < 0 \\ mLW & \text{otherwise} \end{cases} \tag{2.5}$$

Simulating the evolution of drainage channels over a permeable bed requires model complexity that is significantly beyond the scope of this study. We assume that subglacial drainage will reach steady-state on a time scale (days to months, see Schoof (2010)) that is short compared to the relaxation time scale of the bed (years), hence we have neglected this drainage evolution time scale. Incorporating a constant level of excess meltwater drainage from upstream sources would simply shift the location of parameter regimes, and thus it has been neglected in this study.

2.2.3 Ice Basal Sliding Velocity

Following Raymond (1996), we start with the equations for incompressible Stokes flow (see discussion in chapter 1), and then compute the centerline sliding velocity of an ice stream by neglecting longitudinal stresses, vertical ice deformation and sliding unrelated to till deformation. The centerline velocity is thus determined by a balance between driving stress, τ_d, and a combination of basal shear stress, τ_b and the lateral stress, leading to (Raymond, 1996),

$$u_b = \frac{A_g W^{n+1}}{4^n (n+1)} \max \left[\left| \frac{\tau_d - \tau_b}{h} \right|^{n-1} \left(\frac{\tau_d - \tau_b}{h} \right), 0 \right], \tag{2.6}$$

where A_g is a constant creep parameter in the shear margins and $\tau_d = \varrho_i g \frac{h^2}{L}$ is an approximation of the driving stress with acceleration due to gravity, g. Enforcing a positive sliding velocity in equation 2.6 arises from the Coulomb friction law, in which there is no sliding when the yield stress of the bed is not attained (Schoof, 2006a). For the ice flow geometry assumed, this is the case when the yield stress exceeds driving stress. Though Raymond (1996) calculated an expression for u_b which in-

cluded cross-stream variations, we neglect these in the same fashion as Tulaczyk et al. (2000b), since they are small and have a minimal impact on the ice stream flux in equation 2.2. When drainage is active, τ_b is small and $u_b \propto \left(\frac{\tau_d}{h}\right)^n$.

2.2.4 Till and Basal Ice Properties

Following Tulaczyk et al. (2000a), till strength can be modeled as a Coulomb friction law, $\tau_b = \mu N$, where N is the effective pressure and μ is a friction coefficient. This can be expressed directly in terms of void ratio

$$\tau_b = \begin{cases} a' \exp\left(-b\left(e - e_c\right)\right) & \text{if } w > 0 \\ \infty & \text{otherwise} \end{cases}, \tag{2.7}$$

where e_c is a till consolidation threshold, a' is the till strength at e_c (different from a given in Tulaczyk et al. (2000a) by a factor of $\exp(be_c)$) and b is also a constant. This assumes that e_c is a lower bound on the void ratio. In this study we only use equation 2.7 to model till strength as a function of void ratio (hence we do not need to explicitly specify μ or calculate N).

At low void ratios, the hydraulic processes described previously are no longer expected to be applicable. Once the till becomes sufficiently consolidated and bed strength is sufficiently large, surface tension effects are no longer able to maintain a clean ice-till interface, and a frozen fringe can propagate into the sediment matrix (Rempel, 2007). We assume that this happens at the consolidation threshold, e_c, and that, once the growth of a frozen fringe is initiated, all subsequent freezing will occur inside the till, so that

$$e_c \frac{\partial Z_s}{\partial t} = \begin{cases} m & \text{if } 0 < Z_s < Z_0 \\ m & \text{if } e = e_c \text{ and } Z_s = Z_0 \text{ and } m < 0 \\ 0 & \text{otherwise} \end{cases}. \tag{2.8}$$

where Z_o is the maximum sediment thickness available.

Once the till layer has completely frozen ($Z_s = 0$), a layer of basal ice may cool down, reducing the vertical ice temperature gradient. The temperature of the basal ice layer changes due to the same heat balance as before,

$$\begin{array}{ll} T_b = T_m & \text{if } w > 0 \\ \frac{dT_b}{dt} = \frac{\varrho_i L_f}{C_i h_b} m & \text{if } w = 0 \text{ and either } (T_b = T_m \text{ and } m < 0) \text{ or } (T_b < T_m) \end{array}, \tag{2.9}$$

where C_i is the heat capacity of ice and h_b is the thickness of the temperate basal ice layer that is being cooled. This serves as an approximation to a fully dynamic model for vertical heat diffusion through an ice stream (MacAyeal, 1993).

2.3 Results

Figure 2.1 shows four characteristic behaviors exhibited by the ice stream model at different prescribed ice surface temperatures. They can broadly be separated into two categories. Figures 2.1a and 2.1b show stable fixed points, where ice stream velocity reaches an equilibrium after some initial transient behavior, via two mechanisms.

In Figure 2.1a, till water content quickly reaches the saturation threshold, w_s, beyond which drainage removes the excess of meltwater being produced. Ice stream velocity, facilitated by the weak bed, also reaches an equilibrium. In this state, a very weak bed coexists with subglacial drainage that removes meltwater as it is produced.

In Figure 2.1b, the initial rate of meltwater production is insufficient to sustain till layer saturation. Till water content rapidly rises due to a high geothermal flux, low vertical heat conduction and a positive feedback loop between increasing velocity, frictional heating, meltwater production and till weakening. This causes a rise in velocity and eventually, a thinning of the ice stream. Thin-

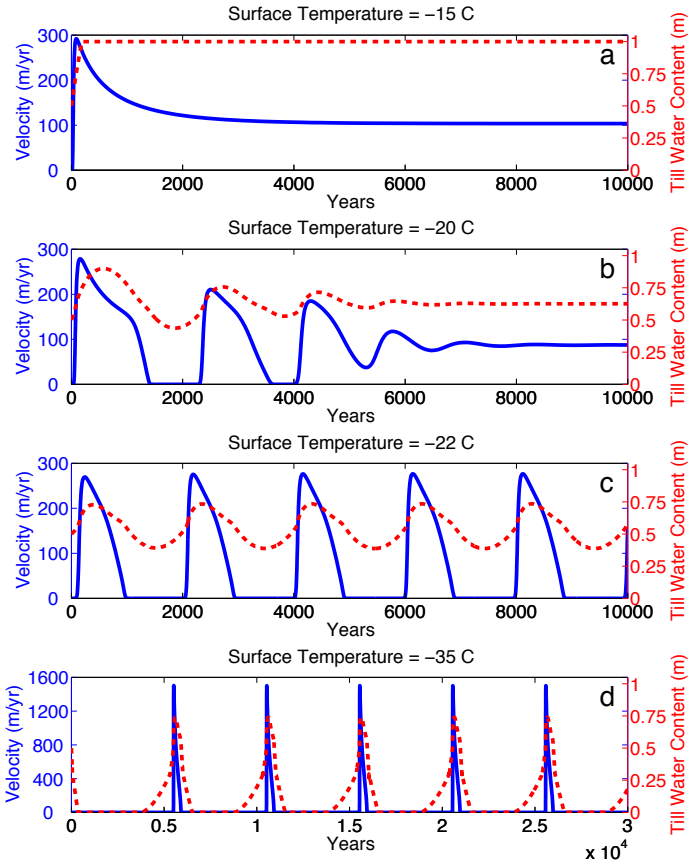

Figure 2.1: Characteristic numerical results for the ice stream model with parameters given by Table 2.1, geothermal heat flux of 0.07 $\frac{W}{m^2}$ and four different prescribed surface temperatures (see location in parameter space in Figure 2.2). In all panels, ice sliding velocity is a blue solid line and till water content is a red dashed line. (a) Steady-streaming with drainage; (b) Steady-streaming without drainage; (c) Weak binge-purge oscillation; (d) Strong binge-purge oscillation.

ning leads to an increase in vertical heat conduction, until it exceeds the prescribed geothermal heat flux and the additional frictional heating, turning the subglacial heat budget negative. Till water content then drops as meltwater is frozen out of the till, leading to till consolidation and ice stream stagnation. During stagnation, slow ice stream thickening from accumulation decreases vertical heat conduction until the ice stream is reactivated. This repeats with decreasing amplitude as the ice sur-

face temperature is insufficiently low to maintain this cycle. Eventually the ice stream reaches an equilibrium velocity similar to that of the drained example of Figure 2.1a. In this case, the equilibrium is maintained by the additional heating due to friction at the bed. This is identical to the "ice stream mode" identified by Tulaczyk et al. (2000b), though in this case the steady-state ice thickness is dynamically determined, rather than prescribed.

Both of these mechanisms (Figures 2.1a and 2.1b) result in steady-state behavior that is very similar. The primary difference is that one equilibrium permits the sustained existence of a subglacial drainage and the other does not. We refer to both collectively as the "steady-streaming mode". Figures 2.1c and 2.1d, on the other hand, show stable limit cycles, where ice stream velocity oscillates indefinitely. The activation of different physical processes in the corresponding two parameter regimes yields oscillations of very different amplitudes and periods.

In Figure 2.1c, a sufficiently cold ice surface is able to sustain the same cycle of accumulation and purging that led to the damped oscillations seen in Figure 2.1b. This weak binge-purge mode is qualitatively similar to the binge-purge oscillations of MacAyeal (1993). However, rather than a prescribed purge time scale, as in MacAyeal (1993), this ice stream model sets its own time scale.

In Figure 2.1d, a very cold atmospheric temperature enables long periods of stagnation during which till is completely frozen and basal ice is cooled. When ice thickening due to accumulation and the resulting weakening of the vertical temperature gradient have turned the subglacial heat budget positive, basal ice warms to the pressure-melting point, till is thawed and renewed meltwater production results in ice stream reactivation. The ice stream has thickened significantly during the long stagnant period, leading to high driving stress (compared to typical modern ice streams) that results in a reactivated ice stream velocity that is much higher than in the weak binge-purge mode. We refer to this as the strong binge-purge mode.

The weak and strong binge-purge modes are similar qualitatively. However, it is important to note that the strong binge-purge cycle is enabled by till freezing and basal cooling, which do not

occur in the weak case, where stagnation occurs above the till consolidation threshold, e_c due to a weaker negative heat flux (see section 2.3.4).

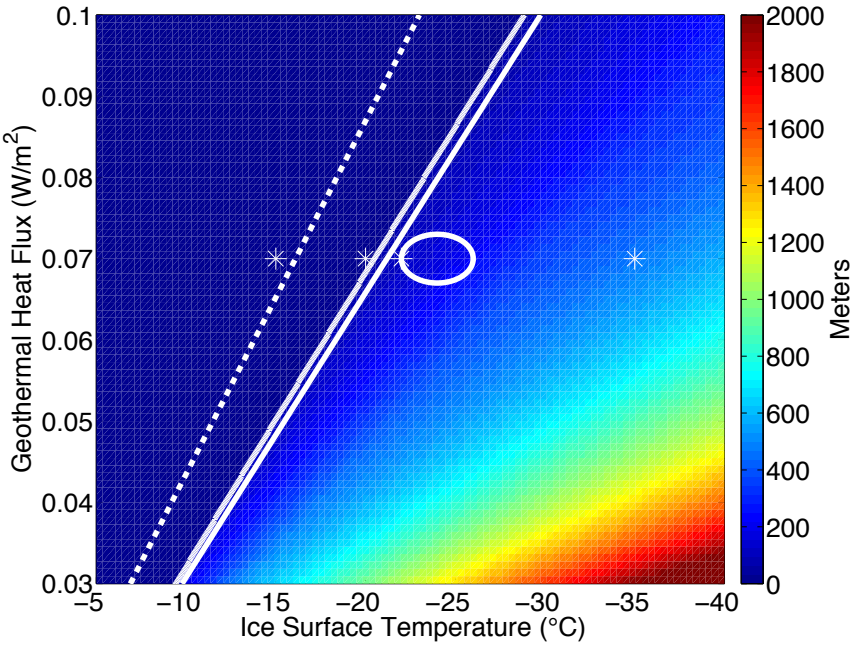

Figure 2.2: Ice thickness oscillation range (in meters) on a plane of the parameter space for which geothermal flux and ice surface temperature are varied and dimensionless parameter α is constant. Rightmost white solid line is analytic approximation to stability boundary between steady-streaming (zero range region in top-left) and binge-purge (finite range region in bottom-right) modes (accurate to within the thickness of the line). Leftmost white solid line is location of the last appearance of binge-purge oscillations in numerical simulations. Both solid white line bound the region of hysteresis. White dashed line is boundary between steady-streaming with and without drainage. White stars indicate locations of characteristic examples in plotted in Figure 2.1. White ellipse marks approximate parameter regime of modern Siple Coast ice streams. Ellipse drawn using geothermal heat flux range estimates cited in Joughin et al. (2004) and a conservative range of mean air temperatures over Siple Coast ice streams from UWisc AMRC data found at amrc.ssec.wisc.edu/aws/.

Figure 2.2 is a plot of ice thickness oscillation range as a function of two main parameters, the geothermal heat flux amplitude and ice surface temperature. The four regimes described above represent a transect through the full parameter space of this simple ice stream model (white stars in Figure 2.2). The steady-streaming mode occurs for warm ice surface temperature and high geothermal

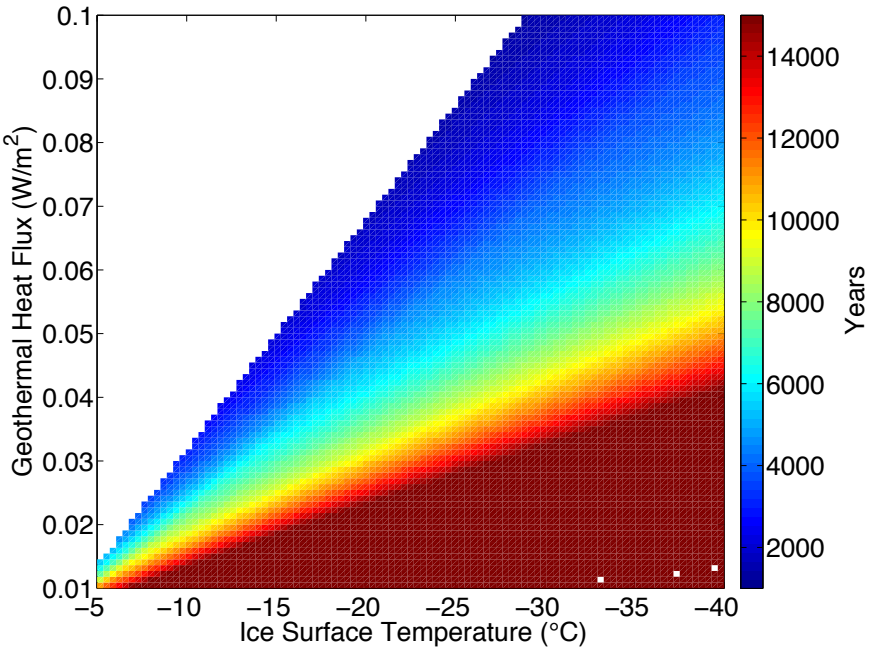

Figure 2.3: Binge-purge oscillation period (in years) on a plane of the parameter space for which geothermal flux and ice surface temperature are varied and dimensionless parameter α is constant.

heat flux (above solid white lines of Figure 2.2). At lower ice surface temperatures and geothermal heat flux (below solid white lines of Figure 2.2), there is an abrupt transition (in the form of a sub-critical Hopf bifurcation, see section 2.3.2) to the weak binge-purge mode. In the region between the two solid white lines of Figure 2.2, the ice stream may reach either mode, depending on initial conditions of ice thickness and till water content. At yet colder ice surface temperatures and lower geothermal heat flux, there is a stronger binge-purge mode.

Figure 2.3 is a plot of the period of ice stream oscillations as a function of the same two parameters as in Figure 2.2. Oscillation period is mostly proportional to oscillation amplitude. Within a robust range of parameters, we find most periods to be of order 10^3 years, reaching a minimum of 800 years. This aligns with other models with thermally-induced oscillations (MacAyeal, 1993; Bougamont et al., 2003b) but appears to be larger than the ice stream oscillation periods suggested by

recent observational studies of modern Siple Coast ice stream (Hulbe and Fahnestock, 2007; Catania et al., 2012).

2.3.1 Stability Boundary

We set out to determine the location of the stability boundary between the two modes of ice stream behavior. The steady-streaming mode corresponds to the steady state solution of our model, and we test for conditions under which this steady state becomes unstable to small perturbations. Such an instability would render the steady-streaming mode unattainable, whereas a stable steady state means that the steady-streaming mode can be realized in practice.

To test for instability, it suffices to consider small departures from the steady state achieved in Figure 2.1b which does not involve drainage, till freeze-on or basal cooling and is time-independent. This reduces our model to equation 2.2 and

$$\frac{dw}{dt} = m \tag{2.10}$$

with m calculated from equation 2.4 and $T_b = T_m$ prescribed. u_b is calculated as before and we define ΔT as the surface temperature departure from T_m. This is similar to the undrained plastic bed model first developed in Tulaczyk et al. (2000b), with the key difference being inclusion of dynamically evolving ice thickness (which has also been included in more complex model studies such as Bougamont et al., 2003a,b). Non-dimensionalization of this reduced model yields the following system

$$\frac{dh^*}{dt^*} = 1 - h^* u_b^* \tag{2.11}$$

$$\alpha \frac{dw^*}{dt^*} = \tau_b^* u_b^* + \beta - \frac{\gamma}{h^*} \tag{2.12}$$

with the dimensionless parameters

$$\alpha = \frac{\varrho_i L_f}{[t][\tau_d][u_b]} \tag{2.13}$$

$$\beta = \frac{G}{[\tau_d][u_b]} = \frac{G}{a_c \varrho_i g[h]} \tag{2.14}$$

$$\gamma = \frac{k_i \Delta T}{[h][\tau_d][u_b]} = \frac{k_i \Delta T}{a_c \varrho_i g[h]^2}, \tag{2.15}$$

where α is the ratio of bed relaxation rate (associated with the timescale on which till water content responds to changes in the basal heat budget) to frictional heating rate, β is the ratio of geothermal heating to frictional heating and γ is the ratio of vertical heat conduction to frictional heating. The characteristic ice thickness scale,

$$[h] = L \left[\frac{4^n (n+1) a_c}{A_g W^{n+1} \left(\varrho_i g\right)^n} \right]^{\frac{1}{n+1}}, \tag{2.16}$$

is expressed as a fraction of ice stream length determined by the ratio of accumulation rate to the maximum ice streaming velocity (for details of non-dimensionalization and other scaling parameters see appendix A.1).

A linear stability analysis (see appendix A.2) then demonstrates that the steady-streaming mode becomes unstable when

$$\beta < \left(\frac{n+1}{n} \right)^{-\frac{n}{n+1}} \gamma - \frac{\left(\frac{n+1}{n}\right)^{\frac{n}{n+1}}}{n+1}. \tag{2.17}$$

It can be shown that the instability takes the form of a subcritical Hopf bifurcation; if started near the steady-streaming solution, the ice stream will rapidly evolve away from it in a sequence of increasing oscillations. Numerically, one can trace the subsequent evolution (using the full model that includes till freeze-on) and show that the ice stream evolves into one of the binge-purge modes,

though a local analysis is not sufficient for this.

We can alternatively write the relationship between geothermal heat flux (G) and surface temperature departure from T_m (ΔT) that denotes the transition from the steady-streaming mode to the binge-purge mode as

$$G = \lambda \Delta T - \varkappa \tag{2.18}$$

where

$$\lambda = \left(\frac{4}{3}\right)^{-\frac{3}{4}} \left(\frac{A_g \varrho_i^3 g^3}{a_c}\right)^{\frac{1}{4}} \frac{k_i W}{4L} \tag{2.19}$$

$$\varkappa = \left(\frac{4}{3}\right)^{\frac{3}{4}} \left(\frac{A_g \varrho_i^3 g^3}{a_c}\right)^{-\frac{1}{4}} \frac{a_c \varrho_i g L}{W}. \tag{2.20}$$

This analytically-determined boundary is the rightmost white solid line on Figure 2.2, confirming that the stability analysis and minor approximations therein provide a good fit to the boundary predicted by numerical simulation and our understanding of the related physical mechanisms.

2.3.2 Mode Transitions and Hysteresis

The nature of the transition between steady-streaming and binge-purge modes is important for understanding how ice streams respond to external forcing. In this simple model, forcing may come from changes in geothermal heat flux (on geologic time scales) or changes in climate (surface ice temperature or accumulation rate). Geothermal heating is approximately constant on the time scale of a particular continental ice sheet configuration. However, surface air temperature and accumulation may plausibly change during glacial cycles or due to decadal to millennial-scale climate variability (e.g. Dansgaard-Oeschger events).

We have already shown that the steady-streaming solution will become unstable when either surface temperature or geothermal heat flux is decreased (more generally, when β is decreased or γ

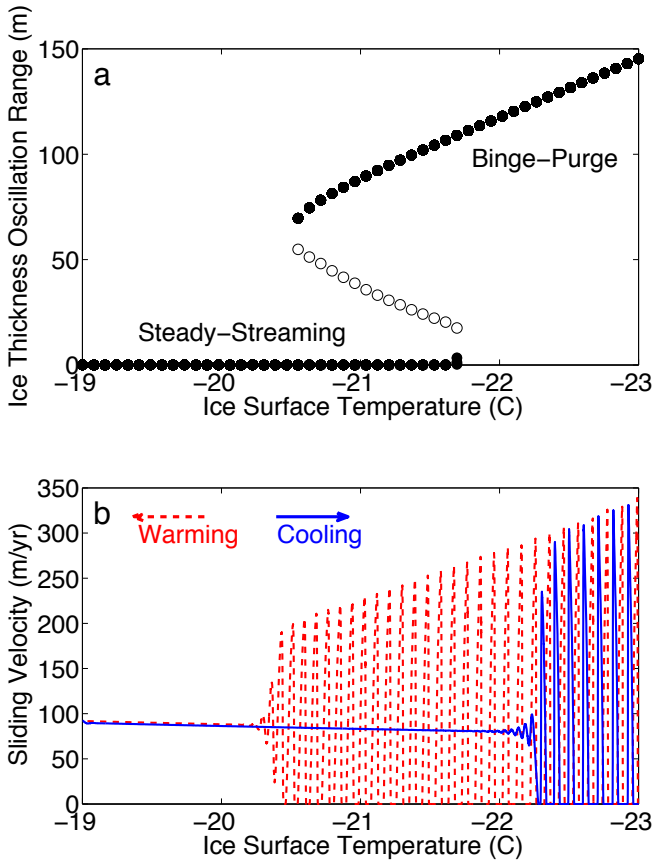

Figure 2.4: (a) Bifurcation diagram. Each point represents a fixed point or limit cycle determined from simulations with a single prescribed ice surface temperature and numerous initial ice thicknesses (initial till water content was kept constant near the fixed point value). Filled points are stable. Open points are unstable. (b) Transient numerical simulation with slow (0.005 °C/century) increase (red) and decrease (blue) in surface ice temperature. Both panels for prescribed geothermal heat flux of 0.07 $\frac{W}{m^2}$.

is increased). It can be shown analytically that the transition to instability takes the form of a Hopf bifurcation, associated with the onset of unstable oscillatory behavior. Figure 2.4a shows this Hopf bifurcation to be subcritical. This figure is generated by initializing the ice stream at a range of initial conditions for each distinct set of prescribed parameters (here only surface temperature is varied) and then determining if all initial conditions lead to a single final state (stable fixed point or limit

cycle; filled points) or multiple final states (unstable limit cycle; open points).

Further normal form transformation and analysis strongly suggest that the bifurcation is subcritical for a wide range of values for α, β and γ (see appendix A.3). As indicated in Figure 2.2, the region of parameter space corresponding to modern West Antarctic ice streams (white ellipse) is in the binge-purge parameter regime. This is consistent with observations which indicate that modern Siple Coast ice streams have periodically switched between active and stagnant states in the recent past (Retzlaff and Bentley, 1993; Hulbe and Fahnestock, 2007; Catania et al., 2012). It is also notable that modern Siple Coast ice streams appear to occupy a parameter regime that is very near the stability boundary (rightmost white solid line of Figure 2.2) to the steady-streaming mode and the region of hysteresis (bounded by solid white lines in Figure 2.2).

The presence of a subcritical Hopf bifurcation (Strogatz, 1994) necessarily implies that by changing a parameter such a surface temperature, there would be hysteresis and irreversibility in ice stream behavior. In other words, the reverse transition from a binge-purge mode to a steady-streaming mode occurs at a higher temperature (Figure 2.4a) than the point at which the steady-streaming mode first becomes unstable. There is therefore, a range of surface temperatures for which both steady-streaming or binge-purge modes are possible.

Figure 2.4b plots ice velocity as a function of surface temperature for a transient run with very slowly changing surface temperature (such that temperature varies on time scale much longer than ice stream variability). In moving from the binge-purge mode to steady-streaming (red dashed line; surface warming) there is a jump from a finite-amplitude stable limit cycle to a fixed point. In the bifurcation diagram of Figure 2.4a, this jump corresponds to the oscillatory solutions disappearing abruptly below $T_s = -20.5°\mathrm{C}$; in technical parlance, this disappearance is termed a saddle-node bifurcation of limit cycles (Strogatz, 1994). Similarly, in moving back from the steady-streaming mode to binge-purge (blue solid line; surface cooling) there is a another jump. The abruptness of these transitions in Figure 2.4b depends on the rate of surface temperature change being sufficiently

slow in comparison to the growth rate of instabilities near the bifurcation point.

The transition between steady-streaming and binge-purge behavior occurs at different temperatures depending on whether the ice surface temperature is increasing (red) or decreasing (blue). This simulation demonstrates the extent to which hysteresis may result in irreversible changes in ice stream behavior over a range of several degrees of surface ice temperature. Given the apparent proximity of modern Siple Coast ice streams to the bifurcation region in parameter space, these results are potentially relevant for understanding the response of Antarctic ice streams to future climate change.

2.3.3 Steady-Streaming Velocity

In steady-streaming mode (Figures 2.1a,b), drainage and friction mediate the equilibrium sliding velocity attained by the ice stream. Steady-streaming with drainage occurs when $\beta > \gamma$ (white dashed line of Figure 2.2), implying that geothermal heat flux exceeds characteristic vertical heat conduction. In this case, the basal shear stress is negligibly small and the fixed point of equation 2.11 and $u^* = \left(\tau_d^*/h^*\right)^n$ require that $u^* = 1$, the steady-streaming velocity will be the characteristic scaled velocity, $[u_b]$. In dimensional units, the equilibrium velocity of steady-streaming with drainage,

$$u_d = W\left[\frac{A_g\left(\varrho_i g a_c\right)^n}{4^n\left(n+1\right)}\right]^{\frac{1}{n+1}}, \tag{2.21}$$

is the velocity that would occur on an ice stream with the characteristic ice thickness (equation 2.16) and a zero-strength bed.

The case of steady-streaming without drainage occurs when $\gamma > \beta > \left(\frac{n+1}{n}\right)^{-\frac{n}{n+1}}\gamma - \frac{\left(\frac{n+1}{n}\right)^{\frac{n}{n+1}}}{n+1}$, implying geothermal heat flux is less than characteristic vertical heat conduction, and above the stability boundary. In this case, we must solve the for the fixed point of (2.11) and (2.12) in the case where $\tau_b^* > 0$. (For the full analysis and higher order approximations, see appendix A.5.) A zero-

order approximation (with $n \to \infty$; accurate to within 5%) on the steady-streaming equilibrium velocity without drainage is

$$u_f = 2u_d \left[(1 - \beta) + \sqrt{(\beta - 1)^2 + 4\gamma} \right]^{-1}, \tag{2.22}$$

with β and γ defined previously. The steady-streaming velocity without drainage, u_f, is a fraction of the steady-streaming velocity with drainage, u_d. It is always the case that $u_f \leq u_d$ in the interval $\gamma > \beta > \left(\frac{n+1}{n}\right)^{-\frac{n}{n+1}} \gamma - \frac{\left(\frac{n+1}{n}\right)^{\frac{n}{n+1}}}{n+1}$.

2.3.4 Binge-Purge Oscillations

To first order, the amplitude (Figure 2.2) and period (Figure 2.3) of the oscillations in the binge-purge mode are controlled by the ratio of vertical heat conduction to geothermal heat flux, the "ratio of equilibrium heat fluxes" (REHF). This quantity is the baseline "forcing" of the basal heat budget, which is then dynamically modified by changes in ice thickness and frictional heating. We define the REHF here as the ratio of two dimensionless parameters of the reduced model, corresponding to vertical heat conduction and geothermal heat flux,

$$\text{REHF} = \frac{\gamma}{\beta} = \frac{k_i \Delta T}{G[h]}, \tag{2.23}$$

where $[h]$ is the ice thickness scale. The expression $\frac{k_i \Delta T}{[h]}$ is the characteristic vertical heat conduction that would occur if ice thickness was at its characteristic scale, $[h]$. In Figures 2.2 and and 2.3, a low REHF occurs in the upper left corner and high REHF in the lower right corner. The transition from steady-streaming with drainage (Figure 2.1a) to steady-streaming without drainage (Figure 2.1b) occurs on the line (dashed white line in Figure 2.2) where REHF is one.

During stagnation, a high REHF lowers the till water content, till thickness and basal ice temper-

ature more than in a low REHF case. This increases the length of time that it takes the ice stream to reactivate and increases the magnitude of accumulation that occurs during the stagnant phase.

Very near the stability boundary (rightmost solid white line in Figure 2.2) in the weak binge-purge mode, the active purge phase is a significant portion of the period of the oscillation. As REHF increases, the amplitude of the purge phase increases and length of the purge phase decreases. This is the result of a more efficient ice stream purge caused by a strong driving stress built up during the longer binge phase.

In the limit of $\alpha \ll 1$, this binge-purge mode can be thought of as a relaxation oscillation with a stagnant branch and an active purge branch, much like the glacial surge model of Fowler (1987). It differs from the Fowler (1987) model and the canonical van der Pol oscillator (Hinch, 1991) in that changes in model variables are non-smooth. Analysis of various parametric limits, and the behavior of the branches in this relaxation oscillator paradigm is included in appendix A.6.

In real ice streams, the limit of $\alpha \ll 1$ does not strictly apply, physically implying that there is a non-negligible time timescale associated with bed relaxation to changes in the basal heat budget. However, a small α limit permits approximation of nullclines of the phase trajectory. These lead to approximations for the critical ice thickness at both stagnation and activation and total binge-purge period. The general strategy is to first find the critical ice thickness at stagnation, h_s, by locating the point at which the active branch of the relaxation oscillator becomes unstable (see Figure 1 in appendix A). We find a second-order asymptotic approximation on this critical stagnation thickness, h_s,

$$h_s = [h]\left[\left(\frac{\gamma}{\eta}\right)^{\frac{1}{n+3}} - \frac{\beta}{n+3}\left(\eta^2\gamma^{n+1}\right)^{-\frac{1}{n+3}} - \frac{n}{2\left(n+3\right)^2}\beta^2\left(\eta^3\gamma^{2n+3}\right)^{-\frac{1}{n+3}}\right], \tag{2.24}$$

with $\eta = \frac{n^n}{(n+1)^{n+1}}$. This generally agrees with the stagnation thickness given by the ice stream model to within 5%.

During the stagnant phase, the ice sliding velocity is (by definition) zero. This greatly simplifies

the reduced model as thickness increases linearly with accumulation and till water content decreases to a minimum at $h = [h]\frac{\gamma}{\beta}$ (from equation 2.12 when $u_b = 0$) and then increases until the critical activation water content and ice thickness are reached. For parameter regimes away from the stability boundary in which the duration of stagnation is much greater than the duration of active streaming, we can derive an approximation on the total binge-purge period

$$T = \frac{\gamma}{\beta - \dfrac{\gamma}{2\dfrac{\gamma}{\beta} - h_s}} \left[\ln\left(2\frac{\gamma}{\beta h_s} - 1 \right) - \frac{\dfrac{\gamma}{\beta} - h_s}{\dfrac{\gamma}{\beta} - \dfrac{h_s}{2}} \right] \left(\frac{[h]}{a_c} \right) \tag{2.25}$$

This confirms the analysis of small α that to first-order, period increases with REHF. This approximation agrees with the period given by the ice stream model (Figure 2.3) to within 10% away from the stability boundary in the weak binge-purge parameter regime. Ignoring basal cooling during stagnation and neglecting the surge duration all contribute to this error. However, without these approximations, closed-form solutions for the binge-purge period and critical thicknesses are unattainable.

This directly leads to an approximation for the critical activation thickness, h_a,

$$h_a = h_s + [h]T, \tag{2.26}$$

which agrees with the critical activation thickness given by the ice stream model in the weak-binge-purge mode to within 10%.

The details of the derivations above and additional asymptotic analyses of the binge-purge solutions are included in appendix A.7.

2.4 Model limitations and future prospects

This study reduces a three-dimensional thermomechanical ice stream with subglacial meltwater to a zero-dimensional model. Without resolving streamwise variations, we have made the implicit assumption that activation and stagnation occurs simultaneously throughout the domain. In reality, the local effects of till water content on ice dynamics will propagate at some finite time scale, which may impact if and how meltwater production throughout the ice stream responds to changes in ice stream thickness. Though this may change some of the details of regimes in parameter space (Figures 2.2 and 2.3), we expect that the relatively short adjustment time scale of bed relaxation (years) will still produce the modes of behavior explored in Figure 2.1.

Similarly, we assumed the vertical temperature profile of the ice stream to be linear in order to simplify the calculation of vertical heat conduction. There are two possible justifications for this: for a stagnant ice stream, a linear temperature gradient could be the result of diffusion-dominated heat transport. For a rapidly-moving ice stream depleting previously stagnant ice on a much faster time scale, rapid advection can equally preserve the shape of the vertical temperature distribution, with the same basal and surface temperatures as before, but compressing the temperature gradient as the ice stream thins. A major limitation of our approach in either case is that temperature changes at the ice surface are propagated instantaneously to the bed. Hence, if we change the parameter T_s transiently (as in Figure 2.4b), we assume that this is instantly felt at the bed. In reality, the diffusion time scale for ice thicknesses of order 10^3 meters can stretch to thousands of years. In addition, field measurements of the vertical temperature profile in ice streams exhibit weak temperature gradients in the upper portion of the ice thickness and much stronger temperature gradients in basal ice (Gow et al., 1968; Engelhardt and Kamb, 1993). Deviation of the measured temperature profile from a linear approximation is primarily the result of horizontal advection of heat in basal ice (Joughin et al., 2004). Thus, dynamically calculating a more realistic temperature profile (MacAyeal, 1993)

would likely result in stronger temperature gradients in basal ice and an enhancement of of vertical heat fluxes at the ice-bed interface. Though this may result in a shift of the parameter regimes, it would not necessarily change the overall structure. Complex interactions between climate forcing on millennial time scales, with similar diffusive time scales and the intrinsic time scale of binge-purge oscillations may yield interesting behavior with relevance to understanding ice sheet responses to climatic variability.

Previous studies of ice streams (Bougamont et al., 2011; Sayag and Tziperman, 2011) have allowed for the emergence of ice stream width using complex ice dynamical models. Our prescription of ice stream width neglects the importance of ice advection across shear margins and shear margin migration during activation and stagnation (Schoof, 2012c). However, bedrock geometry may simply confine ice stream geometry to a fixed width, and this still represents a reasonable first approximation to make. In any case, prescribing ice stream width enabled the exploration of the impacts of ice stream geometry on flow variability in the above analysis.

Saturation and consolidation thresholds are utilized in our model in order to include necessary physics without complicating the model. The till consolidation threshold, e_c, is the point at which ice-debris interlayering and ice lensing occur in subglacial till, preventing further extraction of water from the till and basal freeze-on of meltwater. We have set $e_c = 0.3$, but its exact value is uncertain (Christoffersen and Tulaczyk, 2003; Rempel, 2007). The till saturation threshold, w_s, represents the point at which till becomes impermeable to further addition of meltwater. In the simulations presented in this study, $w_s = 1$ meter, ensuring that saturation is reached when the bed is very weak. More observational data are necessary to determine the actual value of w_s for subglacial tills, which may affect our estimate of the steady-streaming velocity for ice streams with drainage (equation 2.21).

The dynamic evolution of subglacial drainage networks has been neglected in this study. Complex model studies (Fowler and Johnson, 1996; Bougamont et al., 2011; van der Wel et al., 2013; Kyrke-Smith et al., 2013) have modeled or parameterized drainage evolution beneath ice streams.

The inclusion of dynamic drainage would likely have the effect of producing regional transport of meltwater within the ice stream trunk. The addition of a realistic upstream meltwater source and subglacial lakes in topographic troughs would impact the distribution of bed strength and ice stream behavior. Unfortunately, it is not feasible to realistically simulate such behavior in the present simple model.

The rate of vertical heat conduction in our model depends on a single prescribed atmospheric temperature. This neglects the impact of atmospheric lapse rate on the surface ice temperature and we also ignore the temperature dependence of effective ice viscosity, which is assumed constant in this study. Similarly, our assumed constant accumulation rate neglects the dependence of precipitation on elevation. Nonetheless, this study produces binge-purge oscillations of similar period and amplitude to studies such as MacAyeal (1993), which includes lapse rate effects on top of a prescribed sea level atmospheric temperature. The surface elevation and surface slopes of modern ice streams are not sufficiently high to expect that there would be a significant impact on ice surface temperature and accumulation rate. This may be different in the case of the ice stream that caused Heinrich events, which may become thick and develop large surface elevation gradients (see bottom-right corner of Figure 2.2 and the simulation of Figure 2.5).

Echelmayer et al. (1994) suggests that the temperature dependence of ice rheology and dynamic effects like strain heating and fabric development in ice stream shear margins may be important. Though the temperature dependence of ice rheology is known, accounting for other complex thermodynamic processes requires a sophisticated model, which is well beyond the scope of this study.

The model's simplicity enabled us to easily interpret its behavior in terms of a limited set of parameters and processes. Further study with more complex models may reveal that there are other physical processes which contribute to ice stream variability. There are several ways in which this model can be improved, mainly by adding realism and eliminating simplifying assumptions.

2.5 Implications for Heinrich events and variability in complex models

Here we explore the implications of our simple model for understanding two sets of results: (a) variability in complex ice flow models and (b) variability of a Hudson Strait Ice Stream as a cause for Heinrich events.

Experiment one of B11 coupled a 3D thermomechanical ice flow model to the undrained plastic bed model of Tulaczyk et al. (2000b), producing damped oscillations in ice stream flow. In Figure 2.5, we have utilized the parameters provided in that study, and find that the ice stream of Figure 2 of B11 is in a parameter regime of our model that produces damped oscillations to a steady-streaming mode without drainage. Comparing the two models, we find that during purge phases, our modeled ice stream rapidly activates and then gradually stagnates, which is the reverse of B11. Additionally, our model reaches a steady-state of moderate speed, whereas B11 reverts to a slow-moving "ice sheet mode". Though our model is much simpler then that of B11, we suggest that the sustained oscillations produced in experiment two of B11 may be obtained by changing the model's prescribed parameters in order to bring it to the lower right region in our parameter space (Figure 2.2). This could replace the ad-hoc drainage parameterization used in experiment two of B11 in order to obtain sustained oscillatory behavior.

For the purpose of comparing our simple model to Heinrich event models, we posit a hypothetical Hudson Strait Ice Stream that is 800 km long, 90 km wide (based on the Hudson Strait bathymetry given by Andrews and Maclean, 2003), with a catchment area covering 25% of Hudson Bay, an effective till layer thickness of 2 meters (based on estimates of total IRD volume, see Hemming, 2004), geothermal heat flux of 0.05 $\frac{W}{m^2}$ and ice surface temperature of $T_s = -35^\circ\mathrm{C}$ (matching the parameters used by MacAyeal, 1993, with all other parameters the same as elsewhere in this study, see Table 2.1). A simulation from our simple model in this parameter regime (Figure 2.6) yields a strong binge-purge oscillation with a total period of 7026 years, a purge phase duration of

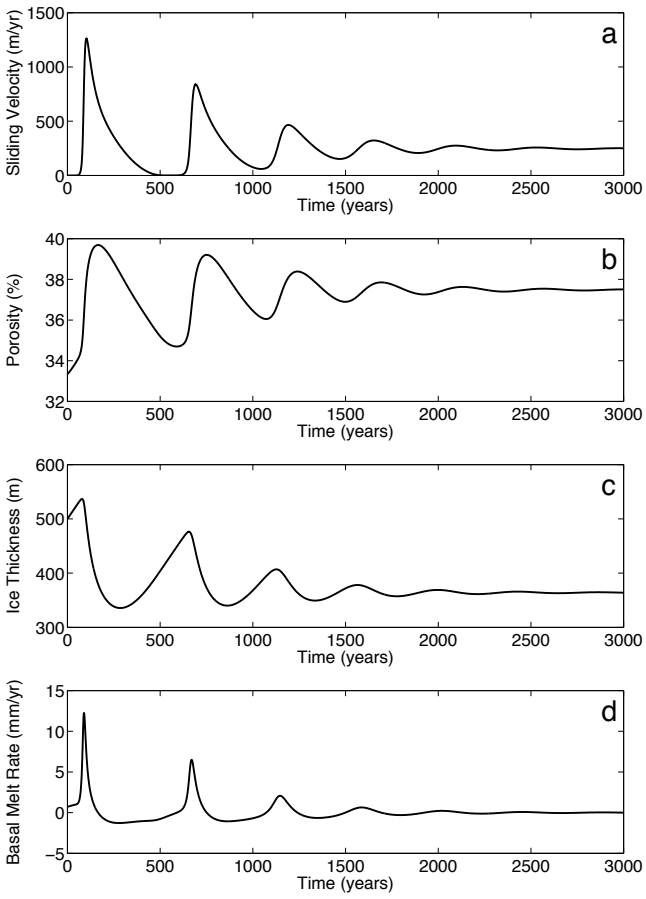

Figure 2.5: Simulation replicating parameter regime of experiment 1 in Figure 2 of Bougamont et al. (2011). We used all parameters given in that study and estimate ice stream width to be 35 km and A_g to be 7×10^{-25} Pa$^{-3} \cdot$ s^{-1} (corresponding to an average temperature of -7 C in the ice stream). (a) sliding velocity. (b) till porosity (note that till porosity $\varphi = \frac{e}{1+e}$). (c) ice thickness. (d) basal melt rate.

208 years, total ice discharge of 1×10^5 km^3 and peak discharge of 0.24 Sv. Though these numbers are dependent on poorly constrained ice stream geometry and ice fabric parameters, they are very close to those found by MacAyeal (1993), who prescribed a purge time scale of 250 years and simulated a Heinrich event period of 7,260 years. We conclude that a dynamically determined purge time scale is

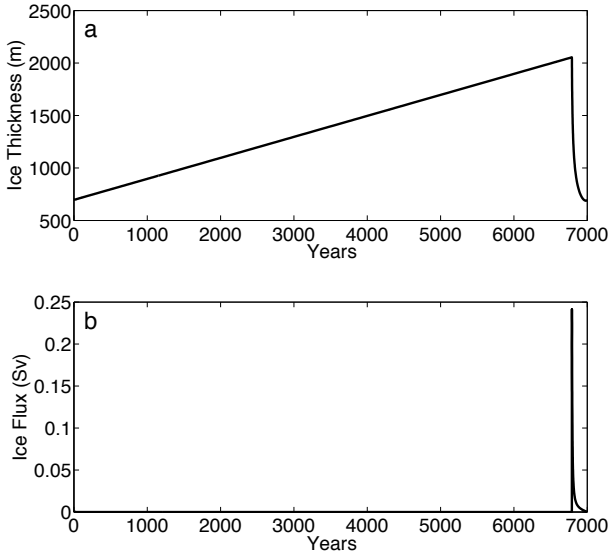

Figure 2.6: Heinrich event simulation with ice stream 800 km long, 90 km wide, catchment area of 1.44×10^5 km^2, 2 m thick effective till layer, geothermal heat flux of 0.05 $\frac{W}{m^2}$ and ice surface temperature of $T_s = -35°$C. (a) Ice thickness. (b) Instantaneous ice flux in units of sverdrups. Note that "catchment area" refers to surrounding ice field with thickness the same as ice stream trunk - presumably the ice stream draws ice from a much larger region.

important in constructing a physically consistent portrait of the Hudson Strait Ice Stream.

The range in total ice discharge (3×10^4 to 5×10^6 km^3), peak discharge (0.15 to 1 Sv), duration (2×10^2 to 2×10^3 years) and period (7×10^3 to 1×10^4 years) of Heinrich events provided by proxy records (Hemming, 2004) is large to the degree that it does not provide a strong constraint on Heinrich events. Nonetheless, this modeling exercise has demonstrated that the variability produced by both modern Siple Coast ice streams and a Hudson Strait Ice Stream can be feasibly explained by the thermal mechanism explored earlier. Future study may then be able to use a more sophisticated version of this model to further constrain the Heinrich event record.

2.6 Conclusions

We analyzed the results of a simple model of ice stream dynamics, coupling basal hydrology with ice flow and including subglacial drainage and till mechanics. This adds physics not captured in previous simple ice stream models, while retaining sufficient simplicity to enable robust analysis of model dynamics in a way not feasible with complex models.

In our simple model, we find that geothermal heat flux and surface temperature control vertical basal heat budget and determine the character of the ice flow, of which we found two potential modes of behavior. A steady-streaming mode is maintained by both drainage and frictional heating at the ice-bed interface, and is qualitatively similar to the ice stream mode described in Tulaczyk et al. (2000b). Unlike Tulaczyk et al. (2000b), the steady-streaming mode in our model depends on the dynamic ice thickness and in some cases, the development of subglacial drainage. Sayag and Tziperman (2009, 2011) also found a transition between streaming and oscillations using a multi-valued basal sliding law, as they varied the accumulation rate. Their model resolved the spatial structure of the ice stream, yet did not simulate the basal hydrology as in this study. The connection of the results here to such sliding laws remains an interesting question for future research.

An oscillatory binge-purge mode is found here with periods ranging from hundreds to ten of thousands of years and amplitude in ice thickness ranging from tens to thousands of meters. The oscillation is primarily caused by meltwater freeze-on during stagnation due to ice thinning and the resulting strengthening of diffusive heat flux away from basal ice. The reverse process of meltwater production occurs during activation.

The transition between the steady-streaming mode and the binge-purge mode is a subcritical Hopf bifurcation for a range of physically-realizable parameters. Simulations where one or more physical parameters are varied across the bifurcation indicate that there is hysteresis in ice stream behavior. As a result, the ice surface temperature at which an ice stream transitions between steady and

oscillating changes depending on whether the temperature increases or decreases. This is a new behavior that has not been found in previous studies of ice stream variability, with significant potential implications to our understanding of the mass balance of the Antarctic ice sheet.

The ice stream variability simulated in this study is also useful for interpreting earlier, more complex, ice stream models. It is likely that one of the experiments of Bii does not produce sustained oscillations in ice stream flow because it resides in the steady-streaming regime of parameter space. Furthermore, our model is able to produce ice stream variability that resembles Heinrich events in both period and amplitude, while constraining a number of characteristics of a hypothetical Hudson Strait Ice Stream that may be the cause of Heinrich events.

3

Rapid Grounding Line Migration Induced by Internal Ice stream Variability

3.1 Introduction

Ice stream flow exhibits variability at a range of spatial and temporal scales, with stagnation and reactivation of fast flow on centennial to millennial time scales playing an important role in the present mass balance of the West Antarctic Ice Sheet. Radar measurements of buried crevasses indicate that Kamb Ice Stream stagnated 150 years ago (Retzlaff and Bentley, 1993), resulting in the currently positive mass balance of the Siple Coast (Joughin and Tulaczyk, 2002). Satellite radar interferometry and ground-based GPS studies have also recorded ongoing deceleration of Whillans Ice Stream (Hulbe and Whillans, 1997; Joughin et al., 2005). Simultaneously, satellite observations (Rignot et al., 2008) indicate that the acceleration of Pine Island Glacier has resulted in a large, negative mass balance in the Amundsen Sea sector. Fahnestock et al. (2000) found that recent centennial-scale variability in several Siple Coast ice streams is recorded in visible satellite imagery of streaklines on the Ross Ice Shelf. Subsequent studies from Hulbe and Fahnestock (2007) and Catania et al. (2012) used an integrated data-model approach to show that low-frequency ice stream variability over the past millennium was accompanied by significant excursions in grounding line position.

In addition to the integrated data-model approaches, observations of submarine, englacial and subglacial features are also important indicators of the significant difference between past and present grounding line positions. A number of studies (reviewed in Livingstone et al., 2012) have used the presence of grounding zone wedges and moraines on the Antarctic continental shelf to infer grounding line positions during the last deglacial retreat of paleo-ice streams. The size of these bedforms implies occasional halting of ice stream grounding lines lasting 100-10,000 years (Anandakrishnan et al., 2007; Dowdeswell et al., 2008; Graham et al., 2010). Additionally, radar and seismic observations from underneath modern Siple Coast ice streams find deformed ice-internal stratigraphy from relict grounding lines (Catania et al., 2005) and multiple stacked sediment pack-

ages (Luthra et al., 2013) that are 80-100 km from the modern grounding line location.

Fast ice stream flow in West Antarctica is caused by the deformation of subglacial till weakened by meltwater produced at the bed (Alley et al., 1986; Blankenship et al., 1986; Engelhardt et al., 1990). Many mechanisms (reviewed in Bennett, 2003) have been proposed to explain the low-frequency variability in ice stream flow, including hydraulic surging, erosion of subglacial till, variations in ice shelf buttressing and interactions with other ice streams. A number of studies have also explored how changes in subglacial till properties and meltwater production may explain centennial to millennial-scale ice stream variability and stable spatial oscillations in ice velocity (Kyrke-Smith et al., 2013). Attempts to understand these mechanisms have ranged in complexity from simple models (MacAyeal, 1993; Tulaczyk et al., 2000b; Robel et al., 2013) to flowline models (Bougamont et al., 2003a,b; van der Wel et al., 2013) to high-order ice flow models (Bougamont et al., 2011). A common feature of these models is the thermal regulation of meltwater production at the bed, which is capable of producing oscillatory ice stream flow. Such a mechanism is broadly similar to early models of mountain glacier surge behavior (Robin, 1955; Clarke, 1976).

A few studies have explored the relationship between ice stream variability and grounding line position. Thomas et al. (1988) offered a conceptual interpretation of ongoing changes in the Siple Coast grounding line that invoked ice stream thermal oscillations. Perhaps confirming such an interpretation, Hulbe and Fahnestock (2004, 2007) simulated large scale migration of the Siple Coast grounding line in response to prescribed ice stream variability. They separately posited that such variability could be caused by oscillations in the basal thermal regime. Hindmarsh and Le Meur (2001) showed that noise-induced drift due to internal ice stream variability could cause grounding line retreat, with an external temperature forcing. However, only recently has the representation of the grounding line in models achieved the level of sophistication necessary to accurately model transient grounding line flux and position. Schoof (2007a) showed that high resolution is needed near the grounding line in order to accurately capture the mechanical transition zone from ice sheet to

ice shelf flow. Fried et al. (2014) used a model with refinement near the grounding line to show how the Siple Coast grounding line would respond to prescribed variations in bed traction simulating ice stream variability. Such an approach has also been employed in transient simulations of ice stream response to forcing (Goldberg et al., 2009; Pollard and DeConto, 2009; Nick et al., 2009; Katz and Worster, 2010; Jamieson et al., 2012; Cornford et al., 2013; Favier et al., 2014).

To determine the significance of forced ice stream variability, it is imperative to first characterize natural modes of unforced ice stream variability and their mechanism. As such, the focus of this study is unforced ice stream variability at centennial to millennial time scales, which has a significant influence on ice sheet mass balance. In section 3.2, we describe a novel implementation of an ice stream flowline model which allows for accurate calculation of transient grounding line migration and activation wave propagation. In section 3.3, we show that this flowline model is similar to the box model of Robel et al. (2013) in parameter space structure and hysteretic transition between steady-streaming and oscillatory behavior. As in previous studies (Oerlemans, 1982b; Fowler, 1987; MacAyeal, 1993; Payne, 1995), we demonstrate (in section 3.3.1) that internal variability arises due to thermal feedbacks in meltwater production at the bed. We find (in section 3.3.2) that in a longitudinally-resolved model, these oscillations produce activation waves that propagate via a coupling of longitudinal stress and frictional heat production. In our model, activations waves are smoothed by the inclusion of longitudinal stresses and meltwater storage in till, though they still require fine upstream grid resolution to be accurately resolved (section 3.3.3). Section 3.4 shows how activation waves cause mass to be transported to the grounding line, producing rapid grounding line migration during the active phase. This key result shows that significant grounding line variability can occur in the absence of retrograde slopes or external forcing. Migrations of the grounding line are solely due to mass imbalances near the grounding line, which may not be representative of the overall ice stream mass balance in our simulations of internal variability. Section 3.5 explores the parametric sensitivity of variability in the ice stream flowline model. We conclude (sections 3.6-

3.7) that it is important to consider the potential significance of internal ice stream variability when interpreting geological evidence of past grounding line positions and the potential for future instabilities in grounding line position.

3.2 Model description

This study employs a depth-integrated shallow ice stream model, incorporating integrated lateral shear stress, meltwater production, an undrained Coulomb plastic till layer and dynamic ice temperature. This model permits the exploration of ice stream behavior arising from the coupling of ice stream thermodynamics to undrained till hydrology. Section 3.2.1 describes the ice stream force balance and an approach for calculating alongstream velocity, followed by ice thickness and grounding line position in section 3.2.2, ice temperature in section 3.2.3, till properties and meltwater production in section 3.2.4, cold-temperate transitions in section 3.2.5 and model numerics, including the stretched coordinate system in section 3.2.6. The assumptions made herein are appropriate for so-called "pure ice streams" in West Antarctica and the Laurentide Ice Sheet on sufficiently long time scales that surface meltwater production is negligible. An extensive derivation and discussion of the flowline model can be found in appendix B.

3.2.1 Ice stream velocity

As shown by Greve and Blatter (2009) and many others, non-rotating ice flow under the force of gravity can be represented by a simplified form of the the incompressible Stokes flow equations (see

chapter 1 for discussion)

$$\frac{\partial}{\partial x}\tau_{xx} + \frac{\partial}{\partial y}\tau_{xy} + \frac{\partial}{\partial z}\tau_{xz} = 0 \tag{3.1}$$

$$\frac{\partial}{\partial x}\tau_{xy} + \frac{\partial}{\partial y}\tau_{yy} + \frac{\partial}{\partial z}\tau_{yz} = 0 \tag{3.2}$$

$$\frac{\partial}{\partial x}\tau_{xz} + \frac{\partial}{\partial y}\tau_{yz} + \frac{\partial}{\partial z}\tau_{zz} = \varrho g. \tag{3.3}$$

The vertical normal stress, τ_{zz} is hydrostatic, allowing the horizontal normal stresses to be expressed as

$$\tau_{xx} = 2\tau^D_{xx} + \tau^D_{yy} - \varrho g(h - z) \tag{3.4}$$

$$\tau_{yy} = 2\tau^D_{yy} + \tau^D_{xx} - \varrho g(h - z), \tag{3.5}$$

where the D superscript indicates deviatoric stresses (Greve and Blatter, 2009). Inserting these expression back in the ice flow equations, and assuming that $\tau_{y}y$ and variations in ice thickness and are small (as they are in the trunk of an ice stream), we are left with

$$2\frac{\partial}{\partial x}\tau^D_{xx} + \frac{\partial}{\partial y}\tau_{xy} + \frac{\partial}{\partial z}\tau_{xz} = \varrho g\frac{\partial h}{\partial x}. \tag{3.6}$$

Integrating over depth, we have

$$2\frac{\partial}{\partial x}\left(h\tau^D_{xx}\right) + h\frac{\partial}{\partial y}\tau_{xy} - \tau_b = \tau_d. \tag{3.7}$$

where τ_b is basal shear stress ($\tau_{xz} = 0$ at the ice surface) and $\tau_d = \varrho_i g h\frac{\partial h}{\partial x}$ is the driving stress (a negative quantity). Integrating across (y) the ice stream and reinserting Glen's flow law for ice (see

chapter 1), yields a horizontal force balance along a central ice stream flowline

$$\frac{\partial}{\partial x}\left(2hA^{-\frac{1}{n}}\left|\frac{\partial u_b}{\partial x}\right|^{\frac{1}{n}-1}\frac{\partial u_b}{\partial x}\right) = \tau_d(x,t) + \tau_b(x,t) + G_s h|u_b|^{\frac{1}{n}-1}u_b, \tag{3.8}$$

where $u_b(x,t) = u(z = b; x, t)$ is the basal ice velocity ($b = b(x)$ is bed elevation). The term on the left hand side is the longitudinal stress and the three terms on the right hand side are (respectively) the driving stress, basal shear stress and cross-stream integrated lateral shear stress, which is estimated assuming that velocity vanishes outside of the ice stream (Dupont and Alley, 2005). The basal velocity u_b is assumed to result from till deformation. A is the vertically-averaged Nye-Glen Law coefficient which is a function of ice temperature, n is the Nye-Glen Law exponent and G_s is a parameter capturing the importance of lateral shear stress.

Longitudinal stress (that is, the τ_x deviatoric stress in the x-direction) is assumed to balance water pressure at the grounding line (Shumskiy and Krass, 1976)

$$\left[2A^{-\frac{1}{n}}h\left|\frac{\partial u_b}{\partial x}\right|^{\frac{1}{n}-1}\frac{\partial u_b}{\partial x}\right]_{x=x_g} = \frac{1}{2}\varrho_i g\left(1-\frac{\varrho_i}{\varrho_w}\right)(1-f)h(x_g)^2. \tag{3.9}$$

Where f is a parameterization of back stress due to ice shelf buttressing (Dupont and Alley, 2005), which arises due to lateral friction between the ice shelf (not simulated here) and a confining embayment. When $f = 0$ (as it is in the baseline simulation), the ice stream is unbuttressed and when $f = 1$, the ice stream is fully buttressed.

The upstream boundary is defined to be the ice divide and correspondingly, velocity is set to zero there: $u_b(x = 0) = 0$. Without any upstream ice sheet inflow, the ice stream is self-contained.

Vertical shear of horizontal velocity is added separately to the basal velocity assuming that it arises

independently due to driving stress

$$u(z) = u_b + \frac{2\bar{A}}{n+1}\tau_d^n h\left[1 - \left(1 - \frac{z-b}{h}\right)^{n+1}\right]. \tag{3.10}$$

Enforcement of $x - z$ mass continuity (assuming that the cross-stream velocity vanishes, $v = 0$) allows for the calculation of vertical velocity, by integrating upwards from the bed at constant $x = x_0$

$$w(x,z,t) = -\int_b^{b+h} \left.\frac{\partial u}{\partial x}\right|_{x=x_0} dz, \tag{3.11}$$

subject to the condition $w + u\frac{\partial b}{\partial x} = 0$ at $z = b$. Elsewhere we also refer to the column-averaged horizontal velocity $\bar{u}(x,t) = \frac{1}{h}\int_b^{b+h} u(x,z,t)dz$.

3.2.2 Ice thickness and grounding line position

Ice thickness evolves by simple advection

$$\frac{\partial h}{\partial t} + \frac{\partial}{\partial x}\left(\bar{u}h\right) = a_c - m, \tag{3.12}$$

with a constant source of accumulation, a_c, everywhere along the flowline. m, the basal melt rate, is generally neglected in this equation as it is 1-3 orders of magnitude smaller than accumulation rate in a grounded ice stream.

By definition, ice begins to float at the grounding line,

$$\varrho_i h(x_g) = \varrho_w b(x_g), \tag{3.13}$$

where ϱ_i is the density of glacial ice and ϱ_w is the density of seawater.

3.2.3 Ice temperature

Calculating ice temperature along the flowline is necessary for reliable determination of the basal heat budget. We model temperature with the advection-diffusion equation in the $x - z$ plane

$$\frac{\partial T}{\partial t} + \frac{\partial}{\partial x}(uT) + \frac{\partial}{\partial z}(wT) = \varkappa \left(\frac{\partial T}{\partial x^2} + \frac{\partial T}{\partial z^2} \right), \tag{3.14}$$

where $\varkappa$ is the thermal diffusivity of glacial ice.

At the ice surface, the temperature is equal to a prescribed atmospheric temperature: $T(z = b + h) = T_s$. At the bed, ice temperature is assumed to be at the pressure melting point: $T(z = b) = T_{MP}$ (see discussion of this assumption in section 3.2.5). There is no heat flux through the ice divide and grounding line: $\frac{\partial T}{\partial x}\Big|_{x=0,x_g} = 0$.

3.2.4 Till properties

Subglacial till properties evolve in a manner similar to Robel et al. (2013), which is a modified form of the undrained plastic bed model of Tulaczyk et al. (2000b). The basal melt rate, m, is calculated from the basal heat budget

$$m = \frac{1}{\varrho_i L_f} \left(G + \tau_b u_b + k_i \frac{\partial T}{\partial z}\Big|_{z=b} \right), \tag{3.15}$$

where, on the right hand side, the first term is the geothermal heat flux, the second term is the frictional heat flux and the third term is the vertical conductive heat flux at the bed. k_i is the thermal conductivity of glacial ice and L_f is the latent heat of fusion.

Till void ratio, $e = \frac{Z_w}{Z_s}$, is a ratio of the thickness of void spaces in the till column (Z_w) to unfrozen solid till thickness without void spaces (Z_s). Assuming that meltwater always fills the void

spaces in the till column, the till water content can then be defined as $Z_w = eZ_s$. e and Z_s then vary as a function of the ice stream state.

Void ratio is assumed to evolve freely when either above or increasing from a specified lower consolidation threshold, e_c

$$Z_s \frac{\partial e}{\partial t} = \begin{cases} m & \text{if } e > e_c \\ m & \text{if } e = e_c \text{ and } Z_s = Z_0 \text{ and } m > 0 \\ 0 & \text{otherwise} \end{cases}, \tag{3.16}$$

where Z_0 is the maximum available till thickness.

To prevent the development of unphysical void ratios, many ice stream models which implement a version of the undrained plastic bed model (Bougamont et al., 2011; van der Wel et al., 2013) set a minimum attainable void ratio (equivalent to e_c here). In reality, till freezes on at this void ratio threshold. When void ratio reaches its lower threshold in models which do not include till freeze-on, additional basal cooling ($m < 0$) has no effect on the till state. Thus, energy is not conserved and future basal heating ($m > 0$) will immediately begin to increase void ratio from the prescribed minimum. In simulations where void ratios reach this minimum and then begin to increase again, the duration of ice stream stagnation will be significantly different, as till does not need to thaw. Our model includes the process of till freeze-on, ensuring that the duration of ice stream stagnation is accurately simulated and energy is conserved.

When the void ratio reaches e_c from above, till begins freezing on as a frozen fringe (Rempel, 2007). Z_s, the current thickness of unfrozen till without void space can be modeled accordingly

$$e \frac{\partial Z_s}{\partial t} = \begin{cases} m & \text{if } 0 < Z_s < Z_0 \\ m & \text{if } e = e_c \text{ and } Z_s = Z_0 \text{ and } m < 0 \\ 0 & \text{otherwise} \end{cases}. \tag{3.17}$$

Equations 3.16 and 3.17 cover all possible till states, with the exception of $Z_s = 0$, which is discussed in section 3.2.5.

The basal shear stress is calculated from the basal velocity and void ratio assuming that the till behaves as a Coulomb plastic material

$$\tau_b = \tau_c \frac{u_b}{\sqrt{u_b^2 + \varepsilon_u^2}}, \tag{3.18}$$

where ε_u is the velocity scale over which till transitions from a quasi-linear to Coulomb friction law. The form of this friction law effectively regularizes the basal shear stress (to account for when $u_b = 0$), but is related to critical state soil mechanics (Schofield and Wroth, 1968). The critical failure strength of the till follows the empirical form of Tulaczyk et al. (2000a)

$$\tau_c = \tau_0 \exp[-b(e - e_c)], \tag{3.19}$$

where τ_0 and b are empirical parameters.

3.2.5 Cold-temperate transition

For sufficiently strong basal freezing, the entire till layer undergoes freeze-on ($Z_s = 0$). Basal ice then cools below the melting point in the same fashion as in the lumped model of Robel et al. (2013) and in inter-ice stream ridges. However, the migration of a cold-temperate transition at the bed in a longitudinally-resolved model requires the simulation of physical processes not included in a typical thin-film, semi-depth-integrated model (Schoof, 2012b). As such, we omit these physics, with the proviso that our model is only valid for simulations in which the till layer never completely freezes through.

Parameter	Description	Value
a_c	Accumulation rate ($m \cdot yr^{-1}$)	0.5
b	Till empirical exponent	21.7
$b_\circ$	Ice divide bed height (m)	100
b_x	Bed slope	-5×10^{-4}
C_i	Volumetric heat capacity of ice ($J \cdot K^{-1} \cdot m^{-3}$)	1.94×10^6
e_c	Till consolidation threshold	0.5
f	Buttressing parameter	0
g	Acceleration due to gravity ($m \cdot s^{-2}$)	9.81
G	Geothermal heat flux ($W \cdot m^{-2}$)	0.07
G_s	Lateral shear stress parameter ($kg \cdot s^{-4/3} \cdot m^{-7/3}$)	400
k_i	Thermal conductivity of ice ($J \cdot s^{-1} \cdot m^{-1} \cdot K^{-1}$)	2.1
L_f	Specific latent heat of ice ($J \cdot kg^{-1}$)	3.35×10^5
n	Nye-Glen Law exponent	3
T_s	Ice surface temperature (°C)	-15
$Z_\circ$	Maximum available till thickness (m)	5
ε_u	Yield Velocity ($m \cdot s^{-1}$)	10^{-9}
$\varkappa$	Thermal diffusivity of ice ($m^2 \cdot s^{-1}$)	1.41×10^{-6}
ϱ_i	Ice density ($kg \cdot m^{-3}$)	917
ϱ_w	Seawater density ($kg \cdot m^{-3}$)	1028
$\tau_\circ$	Till empirical coefficient (Pa)	5.42×10^4

Table 3.1: Parameters used for baseline simulation in this study (unless otherwise indicated).

3.2.6 Stretched coordinates and model numerics

The ice surface and grounding line constitute free boundaries of the grounded ice stream. It is thus advantageous to formulate the numerical solution in a stretched coordinate space

$$\sigma = \frac{x}{x_g} \tag{3.20}$$

$$\eta = \frac{z - b}{h} \tag{3.21}$$

where $x_g = x_g(t)$ is the grounding line position, $h = h(x, t)$ is the ice thickness and $b = b(x)$ is the bed elevation (in a similar fashion to Katz and Worster, 2010). In this system, the grounding line is always at $\sigma = 1$ and the ice surface is always at $\eta = 1$. This approach prevents the strong grid size dependence in fixed grid solutions (Vieli and Payne, 2005) and allows grid refinement near the grounding line for accurate calculation of transient grounding line migration. This numerical approach is similar to moving grid models without coupling to an ice shelf (referred to as model class MGSHSF in Vieli and Payne, 2005).

The ice divide and grounding line are, respectively, the first upstream and last downstream nodes in the model domain. The basal velocity solution is defined on grid nodes, and ice thickness, till properties and temperature are defined on grid elements. Alongstream variations in horizontal basal velocity are calculated using the variational approach of Schoof (2006a) applied to the force balance described in section 3.2.1. At each time step, we simultaneously solve for ice thickness and the grounding line position for the stretched domain using backward Euler implicit time integration. We also solve a transformed version of the temperature equation in the stretched domain, in which horizontal diffusion is neglected. See appendix B for all transformed equations and scaling arguments.

3.3 Ice stream internal variability

In this section, we describe ice stream thermal oscillations and their similarity to variability produced in other models (Clarke, 1976; Fowler, 1987; MacAyeal, 1993; Payne, 1995; Fowler et al., 2001; Robel et al., 2013). We also show that in a flowline model, transitions between stagnant and active phases of ice stream behavior are manifested as propagating activation and deactivation waves (Fowler and Schiavi, 1998). Here, we advance previous work by demonstrating that activation waves propagate through a coupling of longitudinal stresses and frictional heat production. Using a sensitivity experiment, we suggest that numerical convergence of spatially-resolved models of ice stream variability only occurs when the grid resolution is sufficiently fine (~1 km) so as to capture the activation wave.

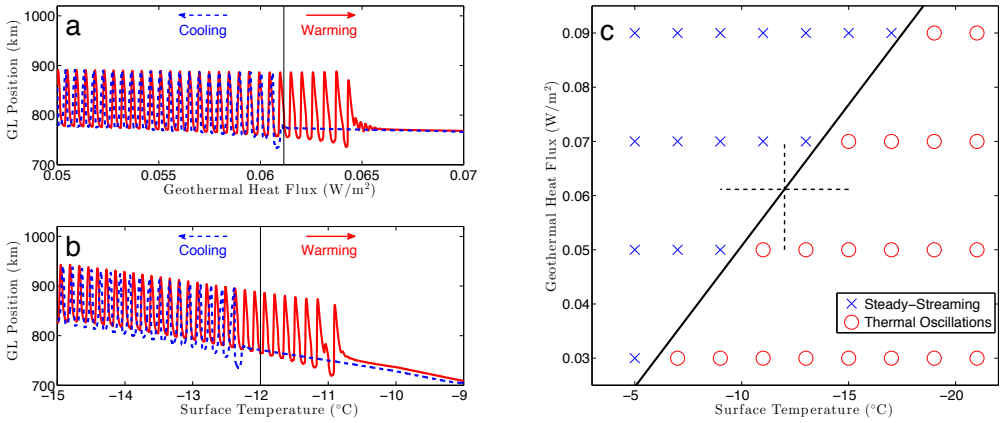

Figure 3.1: (a) Transient numerical simulation with slow (4×10^{-5} W m^{-2}/century) decrease (blue dashed) and then increase (red solid) in geothermal heat flux. Surface temperature held constant at $T_s = -12°$ C. Solid black line is the analytical stability boundary corresponding to solid black line in panel c. (b) Transient numerical simulation with slow (1.2×10^{-2} °C/century) decrease (blue dashed) and then increase (red solid) in ice surface temperature. Geothermal heat flux held constant at $G = 0.0612$ W m^{-2}. Solid black line is the analytical stability boundary corresponding to solid black line in panel c. (c) A summary of model results in a parameter space of ice surface temperature and geothermal heat flux. Blue crosses are steady-streaming simulations (stable fixed point). Red circles are oscillatory simulations (stable limit cycle). Solid black line is an analytically-derived stability boundary from chapter 2 with a correction for bed slope. See appendix B for details of parameter mapping and correction. Dashed black lines correspond to range of parameter variation for hysteresis simulations shown in panels a-b. All other parameters are specified in Table 3.1.

Going forward, we initialize simulations by running the flowline model to a converged state in

which the ice stream is permanently streaming at moderate velocity. Our simulations then have an initialization period wherein the prescribed surface temperature is gradually decreased. The surface temperature and all other system parameters (listed in Table 3.1 for the baseline simulation) are then held constant to allow the ice stream to equilibrate to the new parameter regime.

When either ice surface temperature or geothermal heat flux is high (as defined by the slope of the black line in Figure 3.1c), there will be an associated weak vertical temperature gradient at the bed. This enables a small negative background basal heat budget, which is augmented by a constant level of frictional heating and leads to a balanced basal heat budget ($m = 0$ in equation 3.15). This parameter regime produces "steady-streaming" behavior in an ice stream. However, if either ice surface temperature or geothermal heat flux is too low, frictional heating is not able to maintain a steady balance. This leads to repeated transitions between the active state where frictional heating causes excess meltwater production and the stagnant state where a shutdown in frictional heating causes meltwater to freeze. We refer to these transitions as "thermal oscillations".

We can compare the behavior of the simple box model of chapter 2 with the more complicated flowline model of this study. First, we see that the transition between steady-streaming behavior and thermal oscillations appears similar to the bifurcation in the simple model of chapter 2. As a result, in simulations where a parameter is slowly varied through the stability boundary in both directions, there is hysteresis (Figure 3.1a-b). However, there are marked differences in the ice stream response depending on which parameter is varied. We see in Figure 3.1b that, despite the slowly applied variation in temperature (6° C over 50,000 years), a "memory" of past changes in ice surface temperature causes the ice stream to follow a different path during warming (red solid line) than it did during the initial cooling (blue dashed line), even upon returning to a steady-streaming state. Though variations in geothermal heat flux (Figure 3.1a) are immediately realized in the basal heat budget, variations in ice surface temperature (Figure 3.1b) are transported downward to the bed on a time scale of 10^4 years. Thus, in addition to hysteresis, which is a general feature of parameter varia-

tion over the stability boundary, it is important to consider the timescale of ice stream adjustment to forcing through parameters such as ice surface temperature and accumulation. It is likely that both hysteresis and ice stream adjustment timescale play an important role in determining the response of ice streams to (relatively) rapid climate forcing both in modern and glacial periods. In section 3.6.2, we discuss the implications of hysteresis for interpretation of geomorphological features formed during deglacial transitions.

After a period of transient evolution, the ice stream reaches a stable behavior and we can determine whether it is in a steady-streaming or oscillatory state. Figure 3.1c shows a representative set of simulations with prescribed surface temperature, T_s and geothermal heat flux, G, varied over a reasonable range. These two parameters effectively span all possible types of ice stream behavior (see discussion of stability in chapter 2 and Figure 2.2). The location of the analytically-derived stability boundary of the simpler model (black line in Figure 3.1c) appears to predicts the transition between steady-streaming and oscillatory states simulated by the more complex flowline model of this study. Thermal oscillations have a minimum period of 700-1200 years near the subcritical stability boundary in the flowline model of this study, which also agrees with the simpler model of chapter 2. This corresponds to a minimum amplitude of $50 - 100$ km in grounding line migration.

The difference in complexity between the simple model of chapter 2 and the more complex model of this study hinders a direct mapping between their parameters (see further discussion in appendix B). However, the preponderance of similarities does suggest that at the very least, the simple model of chapter 2 can be useful in explaining the mechanisms underlying the behavior of more complex ice stream models.

3.3.1 Thermal oscillations

Hovmöller diagrams are used extensively in climate dynamics to show the propagation of a wave (in some system quantity) along one spatial dimension over time. Figure 3.2 shows a Hovmöller dia-

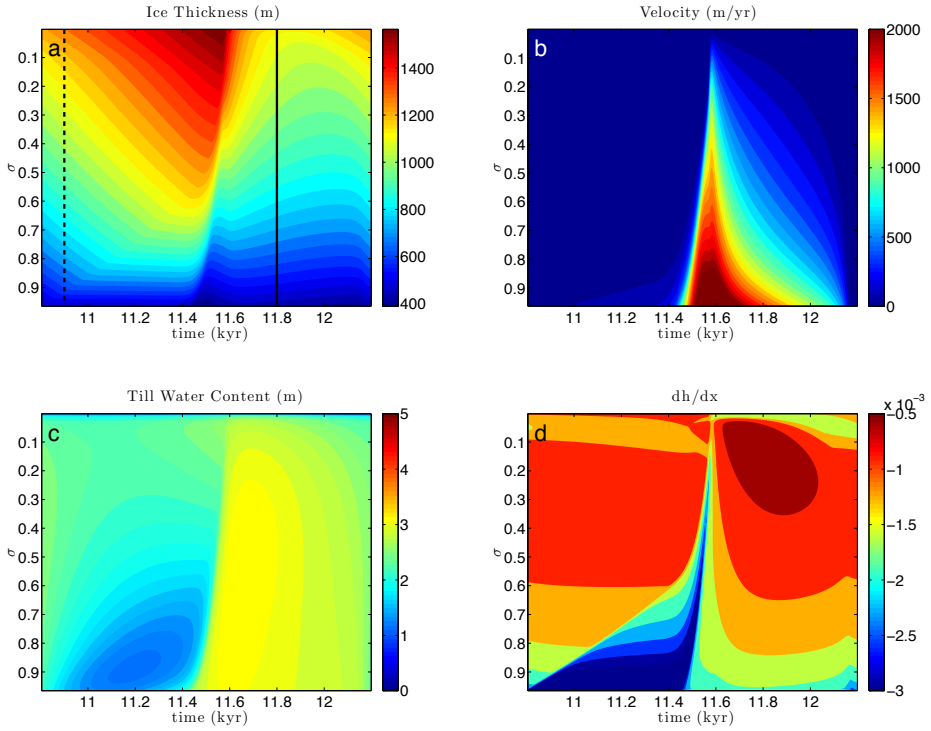

Figure 3.2: Hovmöller diagrams of a single ice stream thermal oscillation. Transient initialization occurs from 0-10 kyr. All panels are a function of time on horizontal axis and stretched alongstream coordinate, σ, on vertical xis. (a) Ice thickness. (b) Basal horizontal velocity. (c) Till water content. (d) Ice thickness slope, $\frac{\partial h}{\partial x}$. In panel a, dashed line indicates location of stagnant ice stream state snapshot corresponding to Figure 3a-b. Solid line indicates location of active ice stream state snapshot corresponding to Figure 3.3c-d.

gram of a single oscillation from a baseline simulation of an ice stream in a thermal oscillatory state. After a transient phase of initialization (0-10 kyr in this simulation), the ice stream reaches a new oscillatory state where it switches between active and stagnant phases. In the stagnant phase (Figure 3.3a), horizontal velocity is low in the ice stream trunk, ice surface slope is high near the grounding line, void ratio is low, part of the till layer thickness is frozen and the basal temperature gradient is decreasing. Over time, the stagnant ice stream thickens, advection of cold ice to the bed is reduced and basal temperatures warm through conduction, producing basal meltwater and weakening the

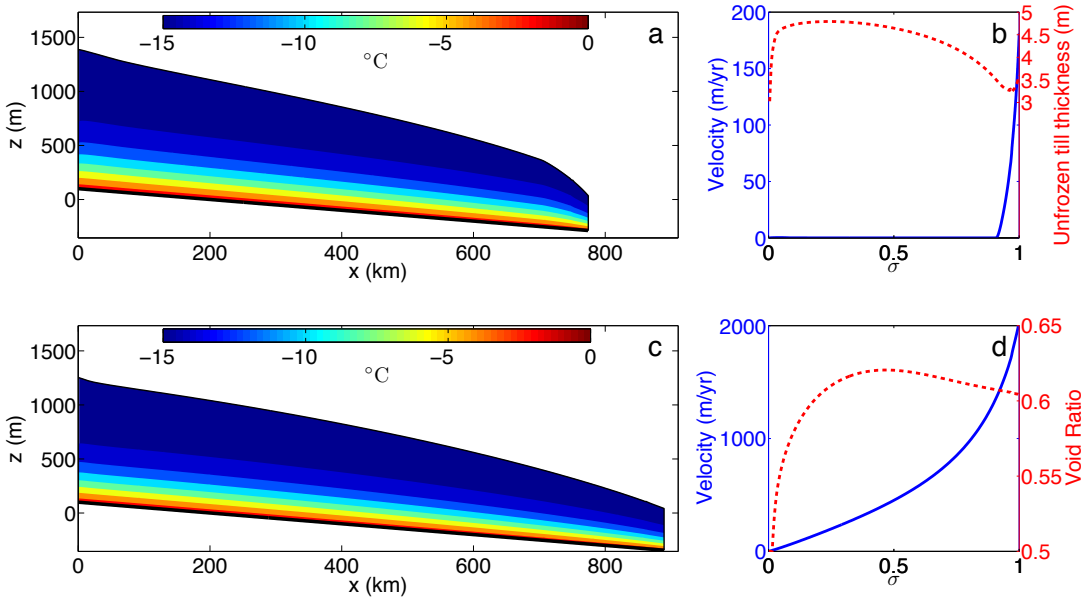

Figure 3.3: Snapshots of ice stream stagnant state ($t = 10.9$ kyr in Figure 3.2 and active state ($t = 11.8$ kyr in Figure 3.2) from thermal oscillatory regime run described in section 3. (a) Side-view of stagnant ice stream, contours indicate ice temperature. (b) Horizontal basal velocity (blue solid line) and unfrozen till thickness (red dashed line; void ratio is at lower consolidation threshold, e_c, everywhere) of stagnant ice stream as a function of σ alongstream coordinate. Maximum available till layer thickness is 5 meters. (c) Side-view of active ice stream, contours indicate ice temperature. (d) Horizontal basal velocity (blue solid line) and till void ratio (red dashed line) of active ice stream as a function of σ alongstream coordinate.

bed. Activation occurs near the grounding line where the bed strength and lateral shear stress become less than the driving stress. During activation there is a positive feedback between frictional heating, meltwater production, till weakening and increased velocities which leads to a rapid increase and then overshoot (beyond what can be supported by ice input from accumulation) in ice stream velocities. In the active phase (Figure 3.3b), horizontal velocity is high everywhere, ice surface slopes are low, void ratio is high and basal temperature gradient is increasing. Over time, the active ice stream thins, increasing vertical heat conduction, freezing basal meltwater and strengthening the bed. Stagnation occurs near the ice divide where the bed strength and lateral shear stress become greater than the driving stress. This thermal mechanism is similar to that described in many previous

studies (Robin, 1955; Oerlemans, 1982b; MacAyeal, 1993; Payne, 1995).

Figure 3.2d shows three "slope breaks" (rapid spatial changes in slope of ice thickness) away from the grounding zone, where there is always a slope break due to the transition to unconfined ice shelf flow. The concave slope break that separates non-sliding, steep upstream ice from fast-sliding, shallow downstream ice quickly propagates upstream during activation. This slope break is due to the transition from partially frozen to unfrozen till and is discussed in greater detail in the next section on activation waves.

During the stagnant phase there is a prominent convex slope break that separates high-slope downstream ice from lower-slope upstream ice. Till is partially frozen everywhere in the ice stream, so non-zero velocities cannot be due to weak till. In this phase, there is some internal ice deformation occurring, but the predominant source of non-zero velocities downstream is slow sliding due to high driving stress (see Figure 3.3a). Longitudinal stresses ensure that the transition to a frictionless ice shelf always produces non-zero mass flux near the grounding line (even when the grounded bed is strong). By removing mass at the grounding line, the ice stream can produce a region of steep slope in the grounding zone, which produces large enough driving stress to match the high yield strength of a partially frozen bed ($\tau_c = \tau_o$; see equation 3.19). The transition from upstream ice below the yield stress to downstream ice at this yield stress corresponds to the transition between non-sliding and slow sliding, producing a slope break. This resembles the slope break near the grounding line of the stagnant Kamb Ice Stream (Catania et al., 2010).

During the active phase, there is a minor concave slope break that remains near the ice divide. As in the model of Schoof (2004), this slope break is the result of the imposed upstream boundary condition, which requires that the ice divide remains stagnant while the remainder of the ice stream is active.

3.3.2 Activation waves

As is apparent from Hovmöller diagrams (Figure 3.2), ice stream activation does not occur simultaneously along the ice stream length, but rather begins near the grounding zone and then propagates upstream as an activation wave. This wave is defined by a sharp transition in ice thickness, till water content and horizontal velocity. As it propagates upstream, ice surface slopes decrease, frictional heating increases, till thaws, void ratio increases, and horizontal velocity increases by two orders of magnitude.

We show here that the mechanism of activation wave propagation is a coupling between frictional heat production and longitudinal stress. At a location where a perturbation of high ice velocity is initiated due to a weak bed, longitudinal stress smooths variations in horizontal velocity. This produces ice slip over a strong bed up and downstream of the initial perturbation, resulting in frictional heat production. This initiates a positive feedback between frictional heating, meltwater production, bed weakening and increased ice velocity. The adjacent till is quickly saturated and horizontal propagation continues as longitudinal stress spreads high velocities from the newly weakened bed. An equivalent "deactivation wave" occurs near the ice divide, but it does not propagate the full ice stream length before complete stagnation occurs. Though this was explored to some extent in Fowler and Schiavi (1998), we will not discuss it here in detail.

In Figure 3.4b, during the stagnant phase, we see a zone of large positive longitudinal stress that corresponds with a slope break. This longitudinal stress maximum slowly moves upstream with the slope break, initiating infinitesimal sliding up and downstream, where the till is still strong. The aforementioned propagation mechanism should be initiated, but the net heat flux at the bed due to geothermal heat flux and vertical heat conduction is negative (Figure 3.4e) and small perturbations in frictional heat production are rapidly dissipated. When the net heat flux at the bed crosses zero due to ongoing accumulation of ice thickness, perturbations in frictional heating are able to rapidly

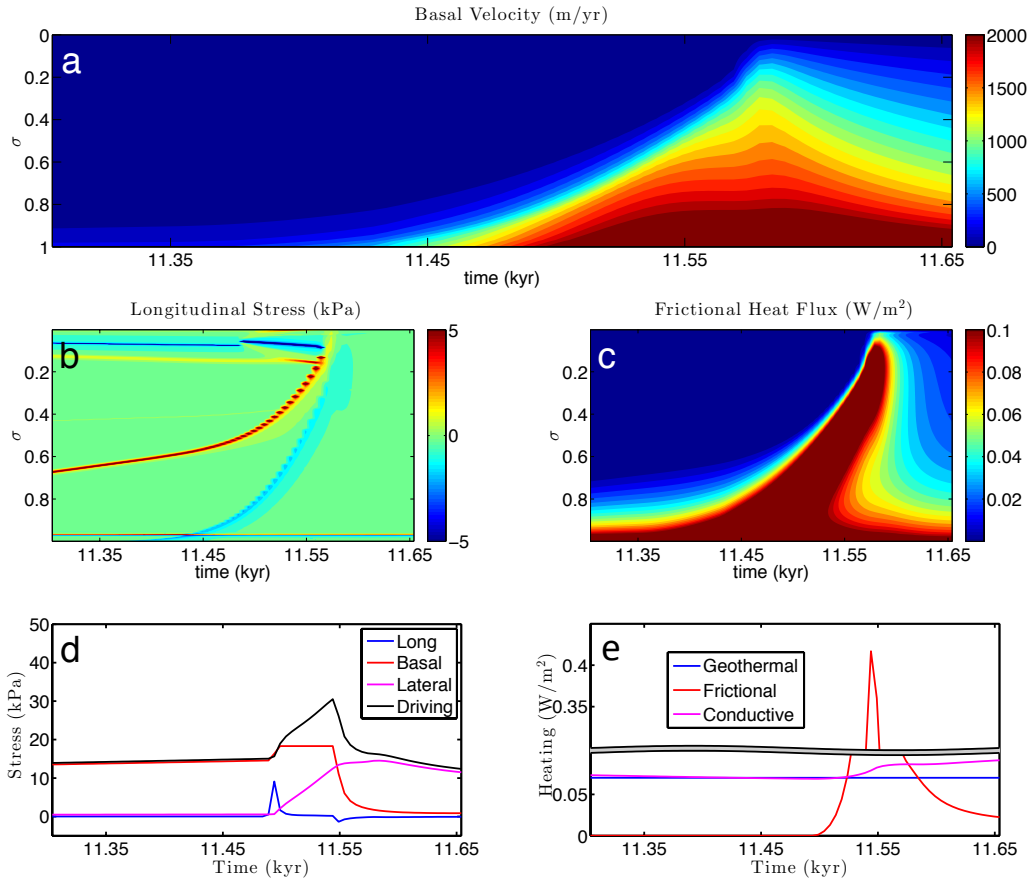

Figure 3.4: Mechanism of activation wave propagation. Panels a-c are Hovmöller diagrams with time on the horizontal axis and stretched alongstream coordinate, σ, on vertical axis. (a) Horizontal basal velocity. (b) Longitudinal stress. (c) Frictional heat flux. Panels d-e are plots of (d) force balance and (e) basal heat budget at a single location ($\sigma = 0.5$) with time on the horizontal axis. In panel e, we plot the negative of the conductive heat flux and split the vertical axis to highlight the difference in geothermal and vertical conductive heat flux.

grow through the positive feedback of frictional heating and meltwater production (Figure 3.4c). We have plotted an example (panels d and e of Figure 3.4) at $\sigma = 0.5$, in the middle of the ice stream, where the net heat flux crosses zero at $t \approx 11.45$ kyr, several decades before there is a spike in both longitudinal stress and frictional heat production. In such a way, the activation wave propagates via coupling of frictional heating and longitudinal stress, but only when the background net heat flux

allows for the growth of the frictional heating instability.

Price et al. (2008) showed a similar feedback between longitudinal stress and frictional heating in simulations of an externally perturbed ice stream model without meltwater storage. In Price et al. (2008) and other similar studies (Payne et al., 2004), initial perturbations near the grounding line propagate upstream while being rapidly damped, typically not reaching further than 100-200 km. In this study, the initiation of streaming at the grounding line is amplified and propagated ~1000 km upstream to the ice divide, where it is damped only because of the prescription of no sliding. The frictional heating instability described previously is the physical mechanism responsible for amplification. However, it is the storage of meltwater in the till layer which maintains weak till long after passage of the activation wave. Sensitivity experiments (Table 3.2) demonstrate that as we increase the maximum available till thickness (Z_0), which controls the rate of till layer adjustment to changes in basal meltwater production, the amplitude of grounding line migration associated with thermal oscillations also increases. Thus, the "memory" maintained by the storage of meltwater ultimately controls the integrated ice stream response to activation waves. This agrees with the speculation of Price et al. (2008), that when basal storage capacity is significant, the enduring effect of past meltwater production enhances the ice stream response to changes near the grounding line.

The growth rate and extent of inland propagation is also dependent on the initial ice stream state. Ice streams that begin in a stagnant state amplify perturbations aggressively due to the significant contrast between stagnant and adjacent active ice. Ice streams that begin in a streaming state (Price et al., 2008) may damp perturbations due to the lesser contrast between streaming and adjacent slightly-faster streaming ice (and hence weaker longitudinal stress gradient). Though this study is focused on understanding the unforced variability of ice streams, these simulations suggest that further study of activation waves and their representation in numerical models would advance understanding of the magnitude, time scale and upstream extent of the ice stream response to forcing near the grounding line.

3.3.3 Activation wave smoothness and model convergence

Activation waves are a common feature of longitudinally-resolved ice sheet models with simple basal hydrology (Fowler, 1987; Greenberg and Shyong, 1990; Payne, 1995; Fowler and Schiavi, 1998). Similarly, in many model simulations of large paleo-ice sheet discharge events (i.e. Heinrich events, see Calov et al., 2002, 2010; Papa et al., 2006), wave-like features do appear. Notwithstanding the qualitative resemblance of these features to activation waves, proper implementation of a basal hydrology scheme is critical to ensuring realistic activation wave behavior and model convergence. As both Payne (1995) and Fowler and Schiavi (1998) argued, models with instantaneous "switches" in sliding and no longitudinal stress will produce shock-like activation waves that are difficult to resolve and prone to numerical errors. Fowler and Schiavi (1998) fixed this problem by including an ad-hoc bed relaxation time scale that smooths the transition from non-sliding to sliding ice. In our model, the inclusion of longitudinal stresses and storage of meltwater in till (which has an intrinsic bed relaxation time scale captured by the non-dimensional parameter α derived in chapter 2) smooths the transition between non-sliding and sliding ice. Hence, the inclusion of some key physical processes associated with realistic ice streams mitigates the numerical issue of shock-like activation waves.

Fowler and Schiavi (1998) showed that matched asymptotic methods can be used to analyze activation waves in shock coordinates. Repeating such an asymptotic analysis for our more complex model is beyond the scope of our study. We instead test the sensitivity of simulated activation wave speed to upstream model resolution (grounding zone resolution is already high) to determine whether it is necessary to resolve the boundary layer associated with the activation wave front (Figure 3.5). At a coarse upstream horizontal grid spacing of ~50 km typical of continental-scale ice sheet models, activation wave speed is approximately twice its fully converged value. At much finer upstream resolution of ~5 km, activation waves are within 10% of fully converged. Further convergence proceeds slowly with increased resolution, but we are confident that our solution has reached nu-

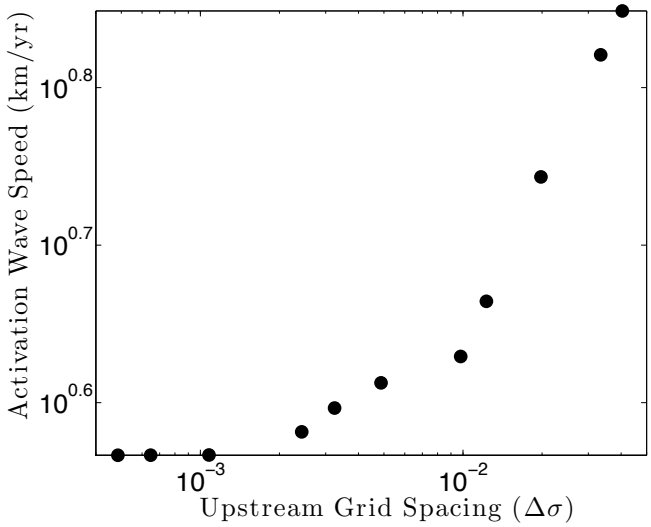

Figure 3.5: Activation wave speed convergence with finer upstream horizontal grid spacing. X-axis is grid spacing measured in non-dimensional stretch coordinate units (in text, we refer to physical units of grid spacing corresponding to an ice stream with $x_g = 1000$ km for simplicity). Activation wave speed is calculated by tracking the movement of the concave slope break referenced in section 3.1 from the grounding zone to a location $x_g/10$ from ice divide.

merical convergence (within 1%) for fine grid spacing of ~1 km. Convergence in activation wave speed is also accompanied by convergence of thermal oscillation amplitude and period. We conclude that accurate simulation of ice stream variability (including Heinrich events) requires considerably finer horizontal grid resolution than what has traditionally been used in coarse-gridded (25-150 km) ice flow models at continental scale (Calov et al., 2002; Papa et al., 2006; Calov et al., 2010). This can likely be accomplished with a hybrid model scheme (Bueler and Brown, 2009) or adaptive-mesh approaches (Goldberg et al., 2009).

3.3.4 Activation wave propagation to the grounding line

In the simulation discussed here, steep surface slopes maintain non-negligible sliding velocities in the grounding zone which produce a constant level of frictional heat production, even during the stagnant phase. Consequently, in this model, the heat budget becomes positive and activation oc-

curs near the grounding line first. This does not imply that activation waves only propagate upstream, as related observational (Fatland and Lingle, 1998) and theoretical (Fowler, 1987) analyses show that mountain glacier surges (which are due to a similar mechanism) propagate both up- and downstream. In this study, it is difficult to discern the downstream-propagating activation wave, as it reaches the grounding line very quickly. Upon reaching the grounding line, this activation wave initiates a short-lived decrease in ice thickness, and attendant grounding line retreat (see black solid line of Figure 3.6a). The influence of the downstream-propagating activation wave is quickly overtaken by transport from the upstream-propagating activation wave which initiates a significantly larger increase in ice thickness and attendant grounding line advance. We discuss this grounding line migration in the next section.

3.4 Grounding line migration

Thermal oscillations in our ice stream model are accompanied by large, rapid migrations in grounding line position (black solid line in Figure 3.6a). When the ice stream activates, the grounding line begins to advance at rates that can exceed 1 km/yr, with most of the advance then occurring over a period of 100-300 years. Grounding line retreat begins during the active phase after excess ice thickness in the grounding zone has been transported through the grounding line. Grounding line retreat at rates of 100s of m/yr then continues for the remainder of the active phase. When the ice stream stagnates, the rate of retreat decreases significantly and the grounding line position becomes nearly static. For a range of parameters appropriate for the Siple Coast (see Table 3.2), the grounding line can migrate 100-170 km over the thermal oscillation cycle. To explain this sequence of grounding line migration events, we examine the advection of mass within and out of the ice stream in more detail.

During the stagnant phase, the bed is strong and supports steep surface slopes in a downstream

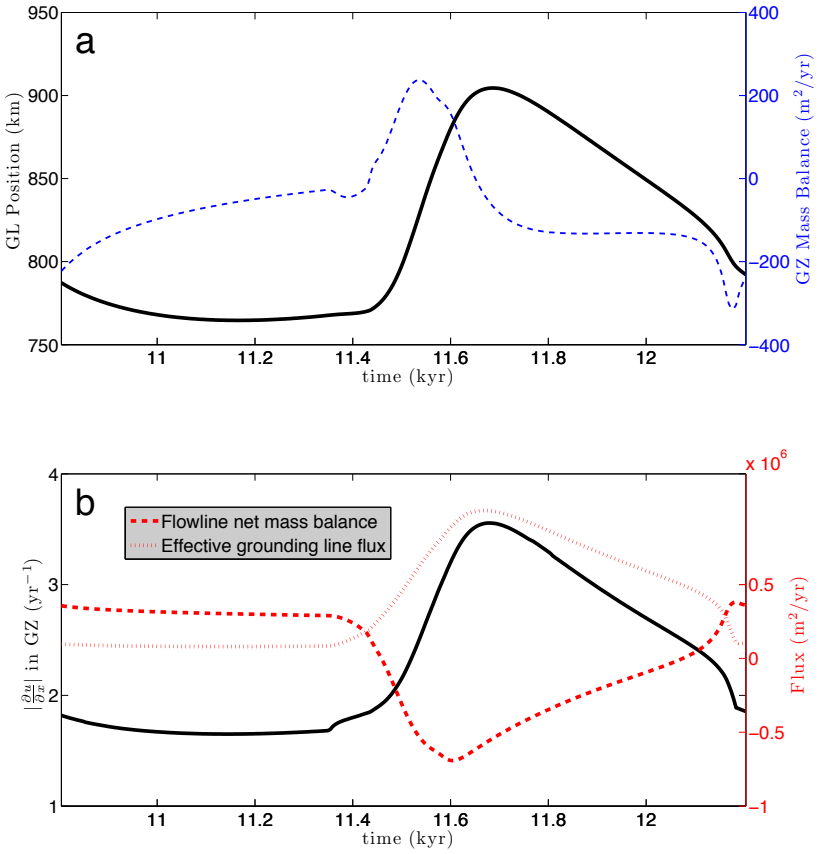

Figure 3.6: Time series of grounding line state over one thermal oscillation. (a) Solid black line is grounding line position. Dashed blue line is net mass balance over the grounding zone, defined as $\Delta\sigma x_g a_c + q(\sigma = 1 - \Delta\sigma) - q(\sigma = 1)$ with $q = uh$ and $\Delta\sigma = 0.03$. (b) Solid black line is average velocity divergence over grounding zone. Dashed red line is the net mass balance for the entire ice stream flowline domain. Dotted red line is the effective grounding line flux: $\tilde{q}_{gl} = [u(x_g) - \dot{x}_g]h(x_g)$. Time is on the x-axis for both panels.

portion of the ice stream, as a significant reservoir of mass is stored upstream. When activation occurs, there is a large divergence in ice velocity near the grounding line (black solid line in Figure 3.6b) associated with the initiation of the upstream propagating activation wave. As the activation wave propagates upstream, it advects ice thickness from the upstream ice mass reservoir to the ground-

ing line. As we argue below, the flotation condition (equation 3.13) ensures that any changes in grounding line ice thickness lead to grounding line migration. As ice is advected to the grounding line from upstream, a nearly equivalent effective grounding line flux (red dotted line in Figure 3.6b) will remove ice from the grounded ice stream. The effective grounding line flux, $\tilde{q}_{gl}$, is calculated as $[u(x_g) - \dot{x}_g]h(x_g)$. $\tilde{q}_{gl}$ accounts both for ice advected through the grounding line and the contribution from a change in the size of the domain (the grounding line in this model), making it the relevant measure of ice leaving the system. In this case, the effective grounding line ice flux does not adjust rapidly enough to compensate for the significant mass flux from upstream and therefore ice thickness in the grounding zone increases, leading to grounding line advance.

As the grounding line position advances, the effective grounding line flux increases with the deepening bed. Eventually, effective grounding line flux exceeds the influx of mass from upstream, leading to a decrease in ice thickness and grounding line retreat. Once the ice stream stagnates, slow advection of ice from the grounding zone continues primarily through slow sliding, which continues for the duration of the stagnant interval until reactivation. Keeping in mind the highly idealized nature of these model simulations (and that they represent an order-of-magnitude estimate of ice flux for a real ice stream system), we can approximate the sea level contribution of internal variability for the Siple Coast-like baseline ice stream simulation. At the peak of ice streaming, the equivalent rate of mass discharge through the grounding line is approximately .15 mm/yr and the total mass flux through the grounding line over the course a single thermal oscillations is 85 mm (for an ice stream 50 km wide at the grounding line, with ice flux spread evenly over global ocean area).

The scale of change in grounding line position resulting from thermal oscillations is determined by ice thickness at the grounding line, where ice begins to float (equation 3.13). This flotation condition can be written in difference form

$$\varrho_i \frac{\Delta h_g}{\Delta x_g} = \varrho_w b_x, \tag{3.22}$$

and then rearranged as

$$\Delta x_g = \frac{\varrho_i}{\varrho_w b_x} \Delta h_g, \tag{3.23}$$

where b_x is the local bedslope over the region of grounding line migration, Δh_g is a change in ice thickness at the grounding line and Δx_g is a change in grounding line position. A straightforward interpretation is that changes in grounding line position are determined by changes in the ice thickness at the grounding line, modulated by the inverse of the local bedslope. This is confirmed by Figure 3.6a, where the net mass balance in the grounding zone (blue dashed line) is proportional to the derivative of the grounding line position. The net mass balance in the grounding zone is defined as

$$\Delta\sigma x_g a_c + q(\sigma = 1 - \Delta\sigma) - q(\sigma = 1) \tag{3.24}$$

with $q = uh$ and $\Delta\sigma = 0.03$. When the net mass balance in the grounding zone is positive, the grounding line thickness is increasing and the grounding line advances. Conversely, when the net mass balance in the grounding zone is negative, the grounding line thickness decreases and the grounding line retreats. For the same change in ice thickness at the grounding line, a shallower bed slope will lead to more grounding line migration. This is confirmed by experiments of sensitivity to bed slope shown in Table 3.2.

In our simulations of an ice stream on a linear prograde bed with no external forcing, the grounding line position repeatedly migrates over a significant distance in response to an internal instability unrelated to the marine ice sheet instability (as first described by Weertman, 1974). Nearly all of the grounding line advance and retreat in our model occurs during the active phase, when the total ice stream mass balance is negative. During the stagnant phase, the ice stream mass balance is positive and a reservoir of mass grows upstream. However, the net mass balance of the grounding zone is small and negative, and the grounding line continues to slowly retreat during the stagnant phase. The local mass balance in the grounding zone (blue dashed line in Figure 3.6a) has a more direct re-

lationship to the grounding line migration rate through its influence on ice thickness than the net mass balance over the full ice stream length (red dashed line in Figure 3.6b). This has important consequences for the interpretations of grounding line migration that associate advance with a positive ice stream mass balance and retreat with negative mass balance (Shabtaie and Bentley, 1987; Joughin and Tulaczyk, 2002). Ice streams that are currently in retreat are likely to have negative mass balance in the vicinity of the grounding zone. However, a retreating grounding line does not always necessitate a negative mass balance in the entire ice stream, as we have shown through the example of unforced variability produced by thermal oscillations.

3.5 Parameter sensitivity

We assess the robustness of the simulated ice stream behavior with a basic sensitivity analysis, varying parameters from the baseline simulation. The results of these parameter sensitivity tests are compiled in Table 3.2, and are meant to sample a range of values that could reasonably be expected for Siple Coast ice streams. Generally, these simulations exhibit thermal oscillations with amplitude of grounding line migration of 100-170 km and a period of 900-1800 years.

Reductions in either ice surface temperature or geothermal heat flux lead to an increase in the amplitude of upstream thickness variations associated with thermal oscillations. This agrees with the results of chapter 2 which predict an increase in amplitude of ice stream thickness oscillations for decreasing ice surface temperature or geothermal heat flux. Counterintuitively, this increase in the amplitude of upstream thickness oscillations results in a decrease in the amplitude of grounding line migration associated with thermal oscillations. As it turns out, when the ice stream activates, the rate of ice transport downstream to the grounding line is reduced by increased lateral stress (see last term on right hand side of equation 3.8) due to thicker ice in the upstream mass reservoir. The slower delivery of ice to the grounding due to increased lateral shear stress is more effectively compensated

	Decreased from baseline			Increased from baseline		
Parameter	Value	Amplitude (km)	Period (yr)	Value	Amplitude (km)	Period (yr)
T_s	-20	120	1297	-10	X	X
G	0.05	119	1306	0.10	X	X
a_c	0.4	152	1714	0.6	135	1190
b_x	-4×10^{-4}	159	1560	-6×10^{-4}	130	1390
G_s	300	153	1314	450	X	X
Z_o	1	104	912	7	165	1570
f	–	–	–	0.5	X	X

Table 3.2: Compilation of results from parameter sensitivity experiments. Simulations marked with an "X" exhibit steady-streaming behavior. Other parameter values are the same as the baseline simulation and are listed in Table 3.1. Baseline simulation has amplitude 137 km and period 1382 years.

by the effective grounding line flux, resulting in less ice thickening at the grounding line and thus less grounding line migration.

A wider ice stream decreases lateral shear stress (G_s) and leads to an increase in thermal oscillation amplitude, but a decrease in period. The reduced period is caused by a lower threshold for activation of stagnant ice streams. When the ice stream activates, reduced lateral stress allows for larger excursions in grounding line position.

Increasing the buttressing parameter (from the baseline of an unbuttressed ice stream where $f = 0$) has the ability to reduce amplitude and period or altogether suppress thermal oscillations (marked with "X" in Table 3.2). This may be an important consideration in applying this model to buttressed ice streams. However, it is unclear what value of the buttressing parameter would be appropriate for real Siple Coast ice streams. As the results in Table 3.2 show, there are other cases in which the stability boundary has been crossed resulting in steady-streaming behavior. This leads us to the same conclusion as in chapter 2, that modern Siple Coast ice streams may reside in a parameter regime on or near a transition to steady-streaming behavior.

3.6 Relevance to observations and other models

As the parameter sensitivity experiments of section 3.5 show, comparing the results of this idealized model to real observations can be complicated by a number of factors including ice shelf buttressing and spatial variations in ice stream width, bed topography, accumulation and ice surface temperature. Additionally, Horgan and Anandakrishnan (2006) and Rignot et al. (2011a) suggested that there is an error of 100s of m/yr in modern estimates of grounding line migration rates in the Siple Coast. The short duration of reliable grounding line observations from aircraft and satellites hinders robust detection of low-frequency signals amid high-frequency noise and potentially significant external forcing. Thus, it is difficult to discern ongoing grounding line migration during most of the thermal oscillation cycle, except in the period immediately following activation and the period surrounding stagnation when migration rates are sufficiently large to distinguish from measurement error. Correspondingly, this section focuses on geological indicators of long-term grounding line migration and their correspondence to model simulations from this and other studies.

3.6.1 Whillans and Kamb Ice Streams

Luthra et al. (2013) found evidence of multiple subglacial sediment packages ~80 km upstream of the modern grounding line of Whillans Ice Stream. These features may have originated from sediment deposition at the grounding line during multiple past retreat and re-advance events. We would expect that the current ongoing deceleration and eventual stagnation would result in grounding line migration to the location of these features. This broadly agrees with Catania et al. (2010), who, on the basis of melt-related stratigraphy, concluded that the grounding line of Whillans Ice Stream has retreated and readvanced coinciding with stagnation and reactivation over the last 850 years.

Thomas et al. (1988) and Horgan and Anandakrishnan (2006) agree that the grounding line of recently stagnant Kamb Ice Stream is static or migrating at a slow rate. Catania et al. (2005) inferred

the presence of a relict grounding line ~100 km upstream of the current grounding line, which may be evidence of past thermal oscillations. Paired with our simulation, one potential interpretation is that Kamb Ice Stream is currently in a period of slow post-stagnation retreat to the location of that relict grounding line. However, this simulation does not account for the fact that the grounding line of Kamb Ice Stream currently lies on a retrograde section of an overdeepening. Another possibility is that the grounding line of Kamb Ice Stream is currently located at a lateral "pinning point" where lateral shear stresses associated with narrowing has prevented further retreat (Dupont and Alley, 2006). Under this scenario, future retreat associated with stagnation may occur rapidly, once the grounding line has passed its current location. Accounting for longitudinal variations in width and bed topography would enable the flowline model to test such hypotheses.

3.6.2 Grounding zone wedges

Grounding zone wedges are widespread features of the Antarctic continental shelf in locations where paleo-ice streams retreated during the last deglaciation (Livingstone et al., 2012). In many instances, these grounding zone wedges are found in clusters (Mosola and Anderson, 2006; Graham et al., 2010) or interspersed with push moraines (O'Brien et al., 1999), indicating episodic grounding line retreat and re-advance. Studies have suggested a number of possible mechanisms for generating these depositional features, such as: changes in external forcing (Hollin, 1962), lateral pinning points (Jamieson et al., 2012) or subglacial drainage events (Livingstone et al., 2012).

It is possible that grounding line migration due to the type of internal ice stream variability simulated in this study was superimposed on gradual retreat of ice streams during the last deglaciation. The simulations shown in this study suggest that there are periods of near-zero grounding line migration associated with both the stagnant phase and the peak of the active phase of an ice stream thermal oscillation. These appear to be sufficiently long to produce grounding zone wedges observed on the Antarctic continental shelf. Such an interpretation is supported by Christoffersen

et al. (2010), who suggested that sediment wedges and other geological features may be the result of subsequent melting and refreezing of basal ice debris.

The stability boundary hysteresis described in section 3.3 may have important implications for interpretations of geological features formed during periods of known climate transition. All else being equal, atmospheric warming associated with a deglacial transition could cause a retreating ice stream to transition from a thermal-oscillatory state which may produce clusters of grounding zone wedges during periods of stagnation to a steady-streaming state which may not produce a grounding zone wedge. This explanation is supported by observational evidence that at least four Antarctic paleo-ice streams underwent episodic retreat on the outer continental shelf and then fast retreat on the inner continental shelf during the last deglaciation (Livingstone et al., 2012). Subsequent cooling associated with the buildup of a large ice sheet would cause the reverse transition, but not at the same location on the shelf. The presence of such hysteresis in ice stream behavior could be revealed by careful analysis of geological features (barring significant overprinting) near the margins of paleo-ice sheets. This is just one example of how using the ice stream model of this study in conjunction with estimates of topography and paleoclimatological forcing could be a powerful tool in interpreting the location and age of paleo-ice stream geomorphological features.

3.6.3 Comparison to other model studies

The data-model studies of Hulbe and Fahnestock (2004, 2007) and Fried et al. (2014) provide the best comparison for simulations of grounding line migration induced by ice stream variability. The models used in these studies include prescribed ice stream variability forcing a domain that primarily encompasses the Ross Ice Shelf. The resulting grounding line migration looks broadly similar to the simulations in our study, including slow grounding line retreat during stagnation and advance after activation. Hulbe and Fahnestock (2007) highlights a 500 m/yr retreat of the grounding line of Kamb Ice Stream following the recent stagnation. This estimate seems large compared to observa-

tions of the grounding line retreat of Kamb Ice Stream and our prediction, though it is possible that more realistic forcing and topography could yield such rapid grounding line retreat.

Our model serves as a complement to the analysis of Hulbe and Fahnestock (2004, 2007). We have improved on these earlier studies by simulating the grounding zone at a sufficiently high resolution to resolve the mechanical transition from ice sheet to ice shelf flow (Schoof, 2007b). This gives us confidence that the type of simulated transient behavior of the grounding line during periods of significant change is reasonable. Additionally, the transport of significant ice thickness to the grounding line during the active phase enables the rapid grounding migration simulated in our model. These dynamics cannot necessarily be realistically reproduced by simply prescribing ice stream variability. By including ice stream thermodynamics and the evolution of till properties, we have a closed system that does not require external forcing to produce grounding line migrations. This enables us to describe the physical links between thermal oscillations, the development of activation waves and migration of the grounding line.

3.7 Conclusions

In this study, we have developed reasonable estimates for the time scale and amplitude associated with thermally-induced grounding line variability. This modeled variability is broadly similar to simpler ice stream models, demonstrating their usefulness as explanatory tools. Activation waves propagate outward from an initial location near the grounding line. A sensitivity analysis demonstrates that accurately modeling thermal oscillations and their associated activation wave requires a resolution of ~1 km. The activation wave triggers grounding line migration that can exceed 100 km at rates over 1 km/yr. In the example shown in this study, grounding line migration is the result of changes in mass balance at the grounding line, which may be different from the total ice stream mass balance. Additionally, these simulations have been used to broadly interpret observations of past

ice stream grounding line migration. We conclude that modeling of specific ice streams with this approach may assist in interpretation of seemingly disparate observations of grounding line migration.

4

Persistence and Variability of Ice Stream Grounding Lines on Retrograde Bed Slopes

4.1 Introduction

Large portions of the Antarctic Ice Sheet rest below sea level and have the potential to rapidly disintegrate, raising global mean sea level by several meters. The stability of marine ice sheets is consequently a major focus of glaciology. Recent theoretical and numerical studies have shown that under certain conditions, the flux of ice through the grounding line (where ice transitions from grounded to floating) increases sensitively with bedrock depth (Chugunov and Wilchinsky, 1996; Wilchinsky, 2001; Schoof, 2007b,a; Durand et al., 2009; Robison et al., 2010). Thus, when the grounding line rests on a retrograde slope (sloping upwards in the direction of flow), any retreat in grounding line position leads to greater flux and consequently additional retreat, and any advance in grounding line position leads to decreased flux and additional advance. By preventing a grounding line on a retrograde or very shallow prograde bedrock slope from achieving a stable steady-state position, this positive flux feedback causes the marine ice sheet instability (Weertman, 1974; Wilchinsky, 2009; Schoof, 2012a).

Ice streams are regions of fast-flowing ice that account for a significant portion of mass transport from the interior of the Antarctic Ice Sheet to the ocean. Observations indicates that the flow of some ice streams exhibits unforced variability on centennial to millennial time scales that has a significant impact on the mass balance of the Antarctic Ice Sheet (Joughin and Tulaczyk, 2002). Other observed changes in the flow velocity of different West Antarctic ice streams have been attributed to externally-forced reduction in ice shelf buttressing (Rignot et al., 2008; Pritchard et al., 2009). Such changes have raised the possibility that forced ice stream variability near topographic transitions to overdeepenings with sections of retrograde slope may lead to rapid retreat (Favier et al., 2014; Joughin et al., 2014). Studies have also begun considering additional or alternate physical processes that play a role in determining the location and stability of grounding lines in marine ice sheets, in-

cluding buttressing of grounded ice by lateral contact between ice shelves and bedrock (Goldberg et al., 2009; Katz and Worster, 2010; Gudmundsson et al., 2012), gravitationally-driven changes in local sea level (Gomez et al., 2010b, 2012), variations in ice stream trough geometry (Jamieson et al., 2012, 2014; Docquier et al., 2014), tidal compaction of till (Christianson et al., 2013) and sedimentation (Alley et al., 2007). Some of these processes have been shown to potentially stabilize grounding lines on a retrograde slope.

This study uses a flowline model that includes dynamically-varying till properties, including temperature and water content. We examine the processes which play a role in unforced, coupled variations in bed properties, ice stream flow and grounding line position on and near retrograde slopes. We come to two main conclusions. First, allowing bed properties to dynamically evolve radically changes model predictions of grounding line position and variability. Second, ice streams, like those in the Siple Coast region of West Antarctica, can exhibit behavior that is unexplained by existing theories of the marine ice sheet instability and ice stream variability. This includes persistence of the grounding line on a retrograde slope for centuries and a reversal of migration direction. The possibility of such behavior is particularly important to consider when evaluating whether observed grounding line retreat onto a retrograde slope is irreversible (Favier et al., 2014; Joughin et al., 2014). In other parameter regimes, we find that sufficiently long sections of retrograde slope can also reduce or suppress unforced ice stream variability in ways that are not predicted by theories of ice stream variability which do not consider complex topography.

In section 2, we describe the ice stream flowline model, idealized bed configuration and underlying mechanism of unforced ice stream variability. In section 3, we analyze the dependence of ice stream grounding line variability on accumulation rate and initial position for a set bed topography. We also compare the behavior of the ice stream when bed properties are not permitted to vary and when they vary freely. In section 4, we systematically vary the idealized topographic configuration and discuss the physical mechanisms which cause modification of ice stream variability without a

retrograde section. Specifically, we analyze how the position, length and slope of the retrograde bed section lead to different types of ice stream behavior. In section 5, we discuss the relevance and implications of these findings for more complex models and ice stream observations.

4.2 Model preliminaries

Active ice streams are strongly resisted by lateral shear stresses resulting from contact with topography or slow-flowing ice ridges (Echelmeyer et al., 1994). Additionally, many ice streams are underlain by till which behaves like a Coulomb plastic material with yield stress depending on water content (Tulaczyk et al., 2000a). In this study, we employ a shallow ice stream flowline model which includes lateral shear stresses and dynamically evolving subglacial till properties. This model solves for ice thickness and till water content along a central flowline (x), with horizontal velocity, vertical velocity and ice temperature also resolved in the vertical (z). As explained in section 3.2.1, the equations for incompressible Stokes flow can be simplified to a horizontal force balance for a depth-integrated ice stream flowline

$$\frac{\partial}{\partial x}\left(2h\bar{A}^{-\frac{1}{n}}\left|\frac{\partial u_b}{\partial x}\right|^{\frac{1}{n}-1}\frac{\partial u_b}{\partial x}\right) = \tau_d(x,t) + \tau_b + G_s h|u_b|^{\frac{1}{n}-1}u_b, \tag{4.1}$$

incorporating integrated lateral shear stress and basal shear stress from an undrained Coulomb plastic bed that evolves as meltwater is produced and refreezes at the ice-till interface. The model self-consistently simulates transient migrations in grounding line position and the propagation of activation waves associated with internal thermal oscillations of the ice stream. The simulations in this study are run at very high horizontal spatial resolution in the grounding zone (~100 m) and high resolution elsewhere (~1 km). The vertical resolution is sufficient (~10 m) to resolve the vertical temperature gradient of basal ice. Additional details of the flowline model and the numerical approach used in the following simulations can be found in chapter 3.

Parameter	Description	Value
a_c	Accumulation rate ($m \cdot yr^{-1}$)	0.3
b	Till empirical exponent	21.7
b_o	Ice divide bed height (m)	100
b_x	Prograde bed slope	-5×10^{-4}
C_i	Volumetric heat capacity of ice ($J \cdot K^{-1} \cdot m^{-3}$)	1.94×10^6
e_c	Till consolidation threshold	0.5
f	Buttressing parameter	0
g	Acceleration due to gravity ($m \cdot s^{-2}$)	9.81
G	Geothermal heat flux ($W \cdot m^{-2}$)	0.07
G_s	Lateral shear stress parameter ($kg \cdot s^{-4/3} \cdot m^{-7/3}$)	400
k_i	Thermal conductivity of ice ($J \cdot s^{-1} \cdot m^{-1} \cdot K^{-1}$)	2.1
L_f	Specific latent heat of ice ($J \cdot kg^{-1}$)	3.35×10^5
n	Nye-Glen Law exponent	3
T_s	Ice surface temperature (°C)	-15
Z_o	Maximum available till thickness (m)	4
ε_u	Yield Velocity ($m \cdot s^{-1}$)	10^{-9}
$\varkappa$	Thermal diffusivity of ice ($m^2 \cdot s^{-1}$)	1.41×10^{-6}
ϱ_i	Ice density ($kg \cdot m^{-3}$)	917
ϱ_w	Seawater density ($kg \cdot m^{-3}$)	1028
τ_o	Till empirical coefficient (Pa)	5.42×10^4

Table 4.1: Parameters used for oscillatory simulations in this study (i.e. those described in the main text).

We start from a baseline simulation with a bed of constant prograde slope

$$b_p(x) = b_o - b_x x, \tag{4.2}$$

where $b_p(x)$ is bed elevation with reference to sea level, b_o is the bed elevation at the ice divide and $b_x = 5 \times 10^{-4}$ is the background prograde slope.

In a baseline simulation, the bed topography is entirely prograde (equation 4.2) and the model parameters (Table 4.1) are set such that the ice stream will, by design, undergo these thermal oscillations in ice velocity and grounding line position. To explore how internal ice stream variability interacts with retrograde bed topography typically associated with overdeepenings and sediment wedges, we add a section of retrograde slope to the baseline prograde topography $b_p(x)$, such that the full bed topography (schematically illustrated in Figure 4.1) used in all the following simulations

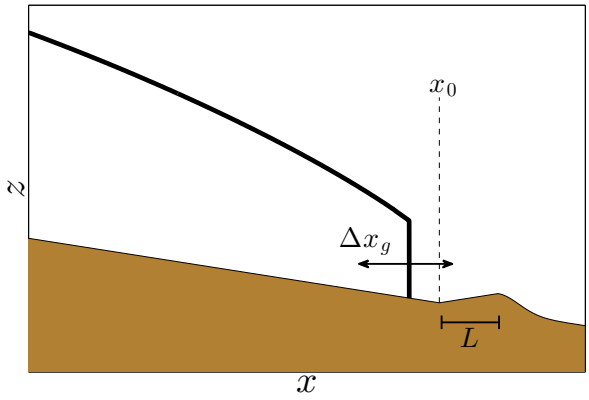

Figure 4.1: Schematic of bed configuration for model simulations. Solid black line indicates ice sheet profile. Brown shaded region is bedrock. x_o is the horizontal position where the retrograde section begins. L is the length of the retrograde section. Δx_g indicates the range over which the grounding line migrates during thermal oscillations.

is given by

$$b(x) = b_p(x) + b_r(x). \tag{4.3}$$

The added topography, $b_r(x)$, has a section of linear retrograde slope, which then exponentially relaxes back to the prograde profile

$$b_r(x) = \begin{cases} 0 & \text{if } x < x_o \\ b_{xr}(x - x_o) & \text{if } x_o \leq x \leq x_o + L \\ L b_{xr} \exp\left[- \left(\frac{2(x - x_o - L)}{L} \right)^2 \right] & x > x_o + L \end{cases} \tag{4.4}$$

where x_o is the position of the beginning of the retrograde section, L is the length of the retrograde section and b_{xr} is the slope of the retrograde section. We choose this simplified bed topography so that we can systematically vary x_o, L and b_{xr} over a wide range of reasonable bed configurations.

4.3 Spatiotemporal variations in bed properties change grounding line behavior

There is significant evidence (Tulaczyk et al., 2000a) to indicate that variations in the water content of sub-ice stream till strongly impacts the yield stress of till and hence the basal ice velocity. However, many ice stream models assume that bed properties are either uniform in time, space or both. The goal of this section is to show that allowing bed properties to freely vary in time and space significantly changes the predicted grounding line position of an ice stream compared to a more conventional scenario where bed properties are assumed to be constant. We do so by comparing our model's prediction of grounding line position to other marine ice sheet models (see Marine Ice Sheet Intercomparison Project Pattyn et al., 2012). In agreement with grounding line stability theory (Schoof, 2007a), these other models predict that, over a wide parameter range, a marine ice sheet with bed properties which are constant in space and time, cannot maintain a stable steady-state grounding line position on a retrograde slope. Additionally, when the grounding line is forced on a retrograde slope, it will irreversibly migrate in a single direction.

The ice stream grounding line migrates in response to internal thermal oscillations in the absence of a retrograde section on the bed, if environmental parameters are in the oscillatory regime of parameter space(Clarke, 1976; Fowler et al., 2001; Sayag and Tziperman, 2009, 2011; Robel et al., 2013). These thermal oscillations (also known as "binge-purge" oscillations) are due to a similar physical mechanism as thermal surging in mountain glaciers, which has been described in previous studies (Robin, 1955; Oerlemans, 1982b; Fowler, 1987; MacAyeal, 1993). Following ice stream activation, till is weak and ice stream horizontal velocity is high. As ice is advected from upstream, the grounding line thickens and rapidly advances by ~130 km to its most seaward position. Ice in the active ice stream trunk thins due to high velocities exceeding accumulation, which increases vertical heat conduction, freezing basal meltwater and strengthening the bed. During the second part of the active phase ice

stream velocity begins to decrease and the grounding line retreats. Eventually, till becomes sufficiently strong that the combined basal and lateral shear stress exceeds the driving stress and the ice stream stagnates. During the stagnant phase, the grounding line continues to slowly retreat to its minimum grounding line position. The ice stream slowly thickens upstream, which reduces the advection of cold ice to the bed and warms basal ice through conduction. Basal meltwater is produced and eventually weakens the bed sufficiently that activation occurs. The dynamics of this process are discussed in further detail in chapter 3.

To compare the predicted grounding line position as a function of a control parameter (Pattyn et al., 2012), we begin with bed topography which includes a shallow retrograde section starting at $x_0 = 800$ km extending to $x_0 + L = 880$ km and with a slope $b_{xr} = 2 \times 10^{-4}$. We vary a single control parameter, in this case accumulation rate, over a range of observationally-motivated values. By initializing the grounding line at many different initial positions, we can determine if there are values of accumulation rate for which there are multiple possible grounding line equilibria. Figure 4.2 plots the equilibrium grounding line position over a range of values of accumulation rate for a static bed (panel a) and a dynamic bed (panels b and c). These can be loosely compared to Figure 9a of Schoof (2007a).

Figure 4.2a illustrates the "static" case, where till yield stress is not allowed to vary as a function of meltwater content and is instead set to $\tau_c = 0$ kPa everywhere. As in the case with a Weertman sliding law, there is hysteresis in the steady-state grounding line position when the control parameter is varied. There is no stable grounding line position attainable on the retrograde section and for a range of accumulation rates ($0.35 < a_c < 0.6$ m/yr), there are two possible steady-state grounding line positions located on the two sides of the retrograde section. This is not surprising, given that lateral shear stress, which has the form $\tau_l = G_s h u^{\frac{1}{n}}$ in this model, takes the place of a Weertman basal shear stress, which generically has the form $\tau_b = Cu^m$. Additionally, previous studies (Tsai et al., 2015) have also found that a Coulomb plastic bed with temporally static properties behaves similarly

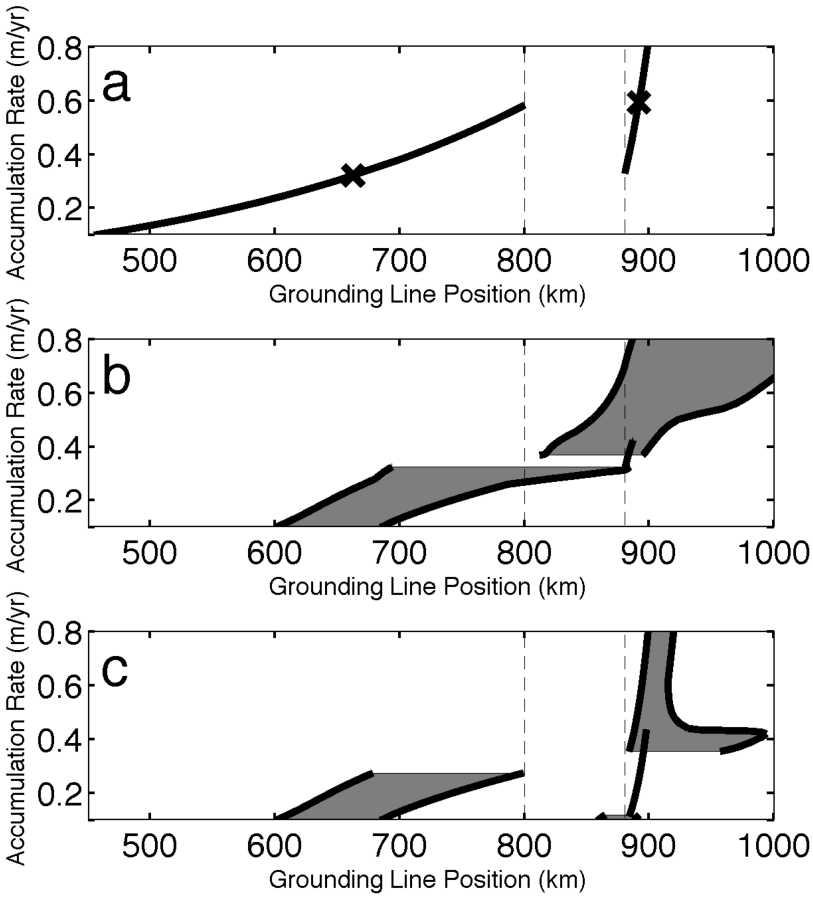

Figure 4.2: Comparison of equilibrium grounding line positions with varying accumulation rate. (a) Bed properties are static with $\tau_c = 0$ kPa everywhere. $b_{xr} = 2 \times 10^{-4}$ (b) Bed properties dynamically evolve. $b_{xr} = 2 \times 10^{-4}$. (c) Bed properties dynamically evolve. $b_{xr} = 10^{-3}$. In all panels $x_0 = 800$ km and $L = 80$ km. Shading indicates range over which grounding line oscillates in equilibrium behavior. "x" marks indicate location of steady states for simulations plotted in Figure 4.4.

(if not more unstable) to a bed with a Weertman sliding law. In all other ways, the ice stream with a static bed of Figure 4.2a is identical to the ice sheet of Schoof (2007a). Though we have chosen $\tau_c = 0$ kPa for simplicity, we can choose to increase τ_c to some arbitrary constant value and the curve in Figure 4.2a will simply translate downward.

In Figure 4.2b, till water content and basal yield stress are allowed to dynamically evolve (with all constants besides accumulation rate as in Table 4.1). The result is that for many values of accumulation rate, there are self-sustained thermal oscillations which cause migration over a range of grounding line positions indicated in Figure 4.2b by shaded regions. The hysteresis found in the static bed case is not found in this dynamic bed case. Rather, the dynamic bed produces two bifurcations where the ice stream steady-state transitions to a finite-amplitude oscillatory state. Using a model with constant prograde bed slope, chapter 3 (extending earlier theories of Fowler et al., 2001; Sayag and Tziperman, 2009, 2011) showed that decreasing accumulation rate and ice stream length should lead to a transition from steady-streaming to oscillatory ice stream behavior, which explains the bifurcation at $a_c = 0.32\ m/yr$. However, the reemergence of oscillatory behavior at high accumulation rate ($a_c > 0.37\ m/yr$) is not explained by such a simplistic model, and is instead related to the presence of a retrograde section (see discussion in section 4.4.4). As in chapter 3, there is hysteresis associated with both bifurcations where either a steady-state or oscillatory grounding line position may occur for a given accumulation rate (note the overlap of the stable steady-state and shaded oscillatory regime for $0.317 < a_c < 0.323\ m/yr$ and $0.37 < a_c < 0.42\ m/yr$ in Figure 4.2b). This type of hysteresis is qualitatively different from the hysteresis observed in the static bed case which arises due to the presence of the retrograde slope.

In Figure 4.2c, bed properties are permitted to evolve, and the position of the retrograde section is the same as in 4.2a and 4.2b. Here, the retrograde slope has been steepened to $b_{xr} = 10^{-3}$. Hysteresis associated with the retrograde slope (seen in Figure 4.2a) has mostly been restored as oscillations in grounding line position do not intersect the position of the retrograde slope. The only exception are low accumulation rates ($a_c \leq 0.12\ m/yr$) initialized seaward of the retrograde section where the grounding line migrates onto the retrograde slope during the stagnant phase of thermal oscillations. There is also hysteresis associated with the bifurcations in this bed configuration.

Comparing the static and dynamic bed cases in Figure 4.2, it is clear that allowing spatiotemporal

variations in bed properties changes not just the grounding line position, but the behavior of the grounding line, over a wide range of parameter values. In some parameter regimes, thermal oscillations cause the grounding line to migrate onto the retrograde section (during ice stream stagnation or activation) before reversing direction. Such behavior cannot be explained by appealing to the flux feedback which causes the marine ice sheet instability for a static bed, as in Figure 4.2a. The flux feedback is only applicable to an ice sheet that is at or approaching a steady-state (Chugunov and Wilchinsky, 1996; Wilchinsky, 2001; Schoof, 2012a). The thermal oscillations that produce internal variability in the grounding line position ensure that the ice stream is perpetually far from a steady-state. Rather than appeal to arguments that rely on such a steady-state assumption, in the next section we examine the physical processes that produce these (and other) types of grounding line behavior.

4.4 Ice stream behavior not explained by existing theories

The goal of this section is to explore the range of ice stream behaviors that are caused by the interaction of ice stream variability with different retrograde bed topographies and explain the physical mechanisms which cause some of these behaviors to diverge from the predictions of earlier theories. To do so, the grounding line is initialized at $x = 640$ km and the accumulation rate is then increased to $a_c = 0.3\ m/yr$. In a baseline simulation, there is no retrograde bed topography, and the dynamically evolving bed causes the grounding line to undergo thermal oscillations (as explained in section 4.2). The simplified nature of the bed topography (equations 4.2-4.4) then permits the addition of a section of retrograde bed that may modify the baseline oscillatory behavior. In each simulation, the position, length or slope of the retrograde section can be changed, while all other parameters are held constant. This explores a section of parameter space that is orthogonal to that explored in section 4.3 (where accumulation was varied). By comparing the baseline simulation to ice stream

behavior with an added section of retrograde slope, we can then explain how natural modes of ice stream variability interact with bed topography. In an exploration of the parameter space of potential retrograde bed configurations, we find four types of ice stream behavior. Figure 4.3 shows (after a period of transient initialization) four representative simulations of grounding line migration with the extent of the retrograde section in these simulations shaded in grey. This includes ice stream grounding lines which exhibit: (a) persistence on the retrograde section for centuries during ice stream stagnation before reversing direction of migration; (b) amplified variability and reversal of direction of migration while active on the retrograde section; (c) complete suppression of variability; (d) reduced amplitude of variability.

4.4.1 Persistence of grounding line on retrograde slope during ice stream stagnation

When the retrograde section is either short or located far upstream of the grounding line, oscillations in grounding line position (Figure 4.3a) are similar in amplitude and period to the baseline simulation (dashed line), though perhaps offset slightly in position along the bed. In such cases, the grounding line does not have much (or any) distance over which it interacts with the retrograde section, thus minimizing the departure from the baseline simulation where there is no retrograde section.

In a subset of cases where the retrograde section is located around the minimum position of the grounding line from the baseline simulation (including the simulation in Figure 4.3a and where $0.43 < a_c < 0.7$ m/yr in Figure 4.2b), the grounding line retreats onto the retrograde section, remains there for the duration of the stagnant phase (hundreds to thousands of years) and then reverses direction and advances onto the prograde slope. We can understand the mechanism of this behavior by comparing with the static bed case. The solid line of Figure 4.4 shows the transient evolution of a single simulation with static bed properties (where the final steady-state is marked by

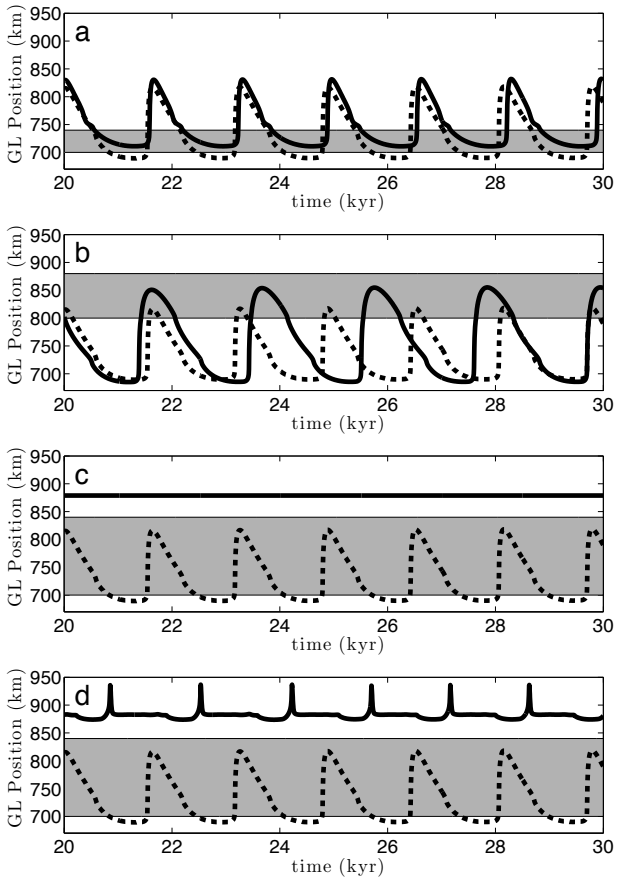

Figure 4.3: Four representative examples of interaction between retrograde section and ice stream thermal oscillations. In all panels, solid line is simulated grounding line migration after transient initialization period ($t < 20$ kyr), dashed line is grounding line migration in baseline simulation run without any retrograde section ($L = 0$ km) and grey shaded area is extent of retrograde section. (a) Minimally-modified thermal oscillations with ice stream persistence on the retrograde section during stagnation ($b_{xr} = 2 \times 10^{-4}$). (b) Amplified thermal oscillations with part of active phase on retrograde section ($b_{xr} = 2 \times 10^{-4}$). (c) Suppressed thermal oscillations ($b_{xr} = 6 \times 10^{-4}$). (d) Thermal oscillations with reduced amplitude ($b_{xr} = 8 \times 10^{-4}$). All examples are initialized with $x_g = 640$ km.

an "x" on Figure 4.2a), initialized at $x = 881$ km and then slowly forced to retreat onto the seaward edge of the retrograde section (at $x_0 + L = 880$ km). As we would expect, the marine ice sheet instability causes irreversible retreat over 1500 years. In contrast, when bed properties are allowed to

freely vary, such a retreat may occur when the ice stream is far from a steady-state and the intuition derived from the static bed theory of the marine ice sheet instability does not hold. Following ice stream stagnation, the grounding line continues to slowly retreat in response to the accumulation of ice thickness and the deformation of ice. However, the strong bed significantly reduces the mass flux out of the ice stream. This reduction in flux slows the rate of grounding line migration that would otherwise manifest as irreversible retreat (as in the solid line of Figure 4.4). During this slow retreat, a reservoir of excess ice mass accumulates upstream, driving an increasing gradient in ice thickness and driving stress, which eventually exceeds the yield strength of partially frozen till, causes slow sliding in the grounding zone and increased mass flux through the grounding line. This slow sliding is enough to cause thinning in the grounding line, reverse the direction of grounding line migration and advance back onto the downstream prograde slope. At this point enough meltwater is produced through frictional heating (and insulation provided by the thick ice) that the ice stream activates, ice from the upstream reservoir is advected to the grounding line, which rapidly thickens and advances.

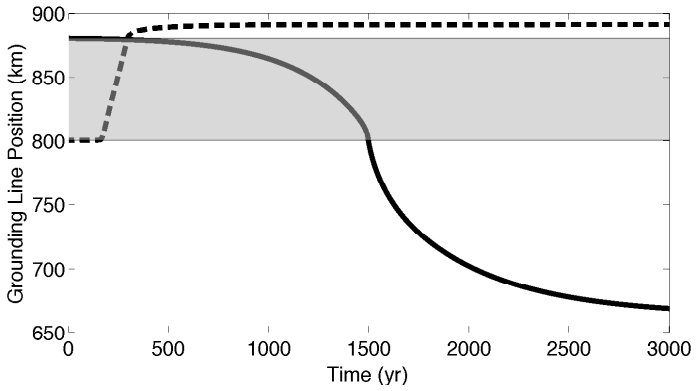

Figure 4.4: Transient evolution of ice stream grounding line position with bed properties kept static ($\tau_c = 0$ everywhere). $x_0 = 800$ km and $L = 80$ km and $b_{xr} = 2 \times 10^{-4}$. Solid line is initialized from $x_0 = 881$ km and $a_c = 0.33$ m/yr, decreasing to 0.32 m/yr over the first 300 years. Dashed line is initialized from $x_0 = 799$ km and $a_c = 0.58$ m/yr, increasing to 0.59 m/yr over the first 300 years.

4.4.2 Active ice stream grounding line reversing direction of migration on a retrograde slope

When there is a shallow retrograde section located around the maximum grounding line position (Figure 4.3b), the active ice stream advances onto the retrograde section, persists for a few centuries, then reverses direction and retreats to the prograde slope. The oscillations in ice stream grounding line position are also amplified from the baseline simulation with no retrograde section (also where $0.27 < a_c < 0.32$ m/yr in Figure 4.2b).

To explain the mechanism behind this persistence on the retrograde section, we again draw a comparison with the static bed case from section 4.3. In a transient simulation (dashed line Figure 4.4), an ice stream with static bed properties is initiated at $x = 799$ km and gently forced onto the landward edge of the retrograde section (at $x_o = 800$ km). The grounding line subsequently advances over the course of 150 years until reaching prograde bed topography. In contrast, when bed properties are allowed to freely vary, excessively high ice velocity during the initial part of the active phase leads to ice thinning, increased vertical heat conduction, till strengthening and decreasing velocity in a matter of decades in the latter part of the active phase. In this short interval, flux through the grounding line decreases and ice at the grounding line begins to thicken, which briefly wins out over unstable advance over the retrograde slope, causing a reversal in the direction of grounding line migration. The retrograde section is important, as it causes the grounding line to advance further than it would in the absence of a retrograde section, effectively amplifying thermal oscillations. If the retrograde section is steepened, there is an acceleration in speed of unstable grounding line advance related to the marine ice sheet instability, which can overcome changes in ice flow due to thermal oscillations (see discussion in section 4.4.3).

The case illustrated in this section is qualitatively similar to the to the persistence of a stagnant ice stream grounding line on a retrograde section discussed in section 4.4.1. The only difference here is

that the retrograde section causes a larger advance during activation than would be expected from thermal oscillations alone (in the baseline simulation with no prograde slope). Nonetheless, the grounding line of any ice stream undergoing thermal oscillations will repeatedly reverse direction, even in the absence of a retrograde slope (see dashed line in Figure 4.3b for baseline simulation). When the ice stream has built up or depleted a large reservoir of ice and is furthest from a steady-state of mass balance, a change in ice flow also causes a change in the tendency of grounding line ice thickness and thus the direction of migration. In the cases highlighted in panels a and b of Figure 4.3, the retrograde section does not have a strong impact on these reversals in grounding line migration (beyond some amplification). In the following two sections we highlight cases where the retrograde section plays a much stronger role in modifying ice stream variability.

4.4.3 Suppression of thermal oscillations by a retrograde slope

A retrograde section can completely suppress thermal oscillations (Figure 4.3c) when it is either: (a) steep and starting near the the maximum grounding line position of the oscillation in the baseline simulation or, (b) shallow and encompassing almost the entire range of grounding line migration in the baseline simulation. Suppression of thermal oscillations leads to a steady-streaming state with no temporal variability in ice flow (Tulaczyk et al., 2000b; Sayag and Tziperman, 2009, 2011) and a grounding line positioned off the retrograde slope.

To explain the suppression of ice stream variability, we can examine how the retrograde slope interacts with the competing feedbacks which produce thermal oscillations. When the ice stream activates, there is an internal positive feedback between frictional heating, meltwater production and till weakening. There is also an internal negative feedback, where the grounding line advances, the ice stream thins and the rate of vertical heat conduction at the bed increases. In the baseline simulation without the retrograde section, the positive feedback dominates, causing an initial overshoot in horizontal velocity and subsequently ice thinning, significant heat loss due to vertical heat con-

duction, meltwater freezing and eventually stagnation. By introducing a retrograde section that is sufficiently long or steep, we increase the extent of grounding line advance during activation and the associated internal negative feedback, which counteracts the internal positive feedback of frictional heating. The result is that till weakens less during activation than in the baseline simulation, the ice stream achieves lower peak horizontal velocity and does not overshoot. Vertical heat conduction at the bed is compensated by geothermal heat flux and frictional heating, causing the ice stream to reach a steady state where the grounding line position is advanced further than the retrograde section.

Alternatively, suppression of thermal oscillations by a sufficiently long or steep retrograde section can be explained in terms of the stability criterion for thermal oscillations derived in chapter 2, which predicts that (everything else being equal) a longer ice stream enhances the importance of a constant geothermal heat flux relative to fluctuations in vertical conductive heat loss. By forcing the grounding line to advance, the retrograde section diminishes the amplitude of variations in vertical conductive heat loss, making it more likely that the basal heat budget will come into balance and the ice stream will reach a steady-streaming state.

4.4.4 Reduction of thermal oscillation amplitude by a retrograde slope

When the retrograde section is long, steep and encompassing almost the entire range of grounding line migration associated with the baseline simulation with nor retrograde slope, the amplitude of grounding line oscillations is reduced from the baseline simulation (Figure 4.3d). In these reduced-amplitude oscillations (which also occur where $0.5 < a_c < 0.8$ m/yr in Figure 4.2c) the grounding line does not migrate landward of the retrograde section ($x_0 + L$).

We can explain the reduction in thermal oscillations amplitude by starting from the suppressed state described in section 4.4.3. The long, steep retrograde slope forces the ice stream to advance and eventually (after transient evolution) settle down to a steady-streaming state similar to the behav-

ior of suppressed oscillations. The difference here is that the retrograde section is sufficiently high ($>$ 100 m) due to its steepness that the ice thickness above that retrograde slope is correspondingly thin (compared to the baseline scenario). Over the retrograde section, this leads to anomalously high vertical conductive heat loss from the bed, freezing of meltwater and strengthening of till. As till strengthens, velocity decreases and longitudinal stresses rapidly spread this signal upstream and downstream to the grounding line as a deactivation wave (Fowler and Schiavi, 1998; Robel et al., 2014). Subsequently, accumulation causes thickening of stagnant ice and leads to reactivation, within a span of 100-200 years. This behavior is the same as typical thermal oscillations, with the only difference being that fluctuations in till state are restricted to a short portion of the bed (~200 km in this example) downstream of the retrograde slope. During the remainder of the ~1000 years of the reduced thermal oscillation cycle, the ice stream is near the same balance as in the suppressed regime and the grounding line is nearly stationary.

4.4.5 A parameter space picture of retrograde section modification of ice stream oscillations

The four panels of Figure 4.5 map thermal oscillation amplitude as a function of retrograde section length (L) and bed slope (b_{xr}), for $x_0 = 700$ km and $x_0 = 800$ km, and initializing simulations of each case on either side of the retrograde section. This parameter space picture captures the most significant modifications of simple thermal oscillatory behavior by retrograde bed topography. Longer or steeper retrograde sections than specified in the above ranges are not included because they may peak above sea level, conflicting with the model assumption that the bed is always below sea level at the grounding line. The parameter range spanned in Figure 4.5 includes the behavior regimes described in the preceding sections.

Retrograde sections located far upstream of the range of grounding line migration associated with thermal oscillations in the baseline simulation ($x_0 + L < 690$ km) or of short length ($L < 80$

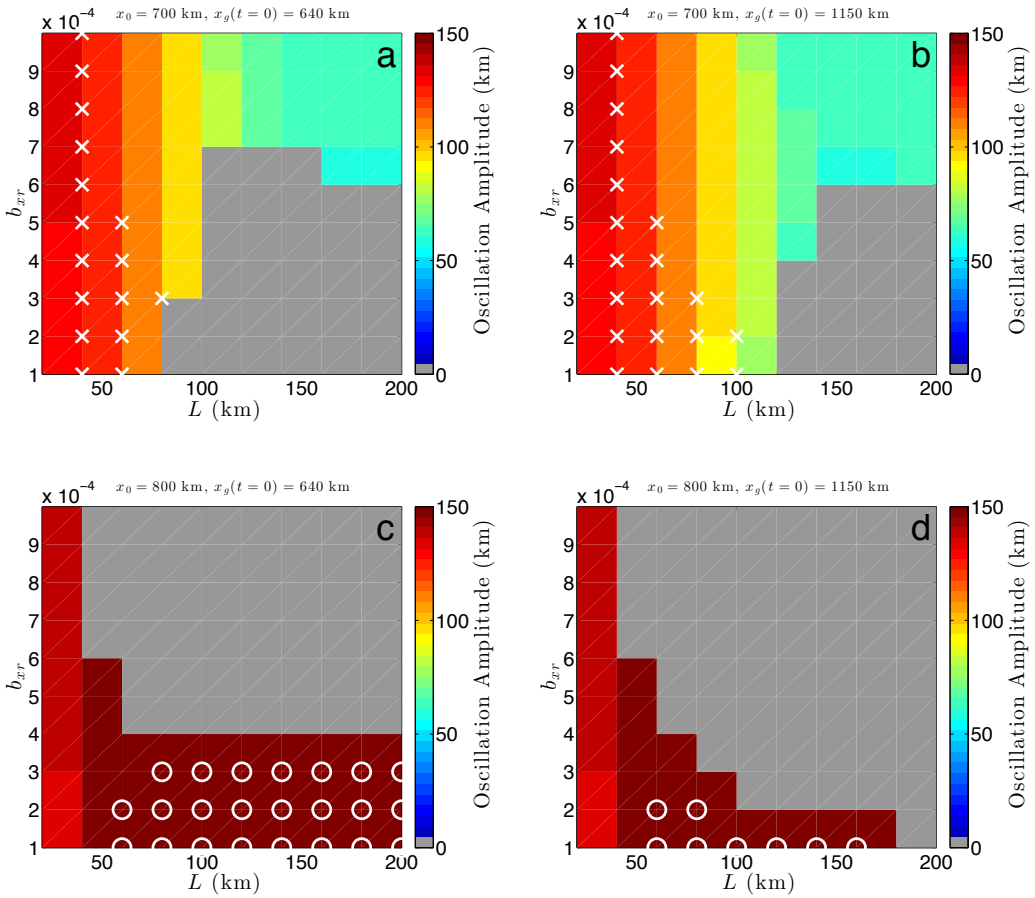

Figure 4.5: Amplitude of grounding line migration associated with thermal oscillations as a function of length (L) and slope (b_{xr}) of retrograde section. Simulations with zero oscillation amplitude are shaded in grey. "x" markers indicate simulations where the grounding line is on a retrograde slope at its minimum position during the stagnant phase. Circle markers indicate simulations where the grounding line is on a retrograde slope at its maximum position during the active phase. Panels (a) and (b) have a retrograde section starting at $x_0 = 700$ km. Panels (c) and (d) have a retrograde section starting at $x_0 = 800$ km. Panels (a) and (c) have initial ice stream grounding line position landward of retrograde section at $x_g(t = 0) = 640$ km. Panels (b) and (d) have initial ice stream grounding line position seaward of retrograde section at $x_g(t = 0) = 1150$ km. In the baseline simulation the grounding line position oscillations between 690 km and 815 km.

km) have a minimal impact on ice stream behavior. However, when the retrograde section is located near the minimum grounding line position the grounding line may persist for centuries on

the retrograde section during ice stream stagnation (marked by white "x" marks in Figure 4.5). Such behavior occurs for a wide range of b_{xr}, indicating that even strong retrograde slopes cannot prevent the reversal of of grounding line migration during at the onset of ice stream activation. There is no evidence that the marine ice sheet instability plays any significant role in producing hysteresis or otherwise modifying the behavior of ice streams which stagnate on or near sufficiently small retrograde sections ($L < 50km$), regardless of the steepness of the retrograde slope.

Shallow retrograde sections located around the maximum grounding line position result in prolonged intervals of several centuries where the grounding line of an active ice stream advances onto and then retreats from a retrograde section (such cases are marked by white circles in Figure 4.5). These long, shallow retrograde section may also amplify thermal oscillations by forcing the grounding line to advance through the same process involved with the marine ice sheet instability. Such behavior is limited to relatively shallow retrograde slopes, indicating that the marine ice sheet instability plays a more important role here and prevents such behavior entirely for steeper retrograde slopes.

When the retrograde slope is either located around the maximum grounding line position and is sufficiently steep (gray regions of Figure 4.5c,d) or sufficiently long that it spans the entirety of the range of grounding line oscillations (gray regions of Figure 4.5a,b), thermal oscillations are suppressed completely. In this case, the retrograde section causes the grounding line to advance sufficiently quickly that ice flow changes associated with thermal oscillations are not able to reverse the direction of grounding line migration. The result is that the ice stream attains a steady-state grounding line position seaward of the retrograde section.

At even steeper slopes, thermal oscillations reappear, but are reduced in amplitude relative to the baseline simulation and are restricted to the bed downstream of the retrograde section. However, there is still a wide gap in oscillation amplitude between parameters regimes where oscillations are suppressed and those where it is reduced entirely. This is to be expected when there is a bifurcation,

as an infinitesimal increase in slope (b_{xr}) of the retrograde section (e.g. along a transect where $L =$ 150 km in Figure 4.5a,b) results in a transition from steady-state to finite-amplitude oscillations in grounding line position. We have yet to find any evidence that the thermal mechanism is capable of producing oscillations of arbitrarily weak amplitude.

Hysteresis behavior associated with retrograde slopes is important because it imprints ice stream history on future behavior and so must be considered when spinning up numerical ice stream models. In section 4.3, we showed that for sufficiently steep retrograde slopes, the marine ice sheet instability may cause the behavior of an ice stream to differ depending on whether it begins landward or seaward of the retrograde section. We also see evidence for such hysteresis in a narrow range of retrograde sections with intermediate b_{xr} and L. Simulations with retrograde sections of intermediate length ($80 < L < 140$ km) and located near the minimum position of grounding line oscillations retain oscillatory behavior when initialized seaward of the retrograde section, but not always when initialized from landward. However, the persistence of a grounding line on the retrograde section during ice stream stagnation only depends on initial ice stream state for a small range of bed topographies. Simulations with retrograde sections of intermediate slope ($2 \times 10^{-4} < b_{xr} < 4 \times 10^{-4}$ km) and located near the maximum position of grounding line oscillations retain generate oscillatory behavior when initialized landward of the retrograde section, but not always when initialized from seaward. Reversal of an active ice stream on a retrograde section appears to be dependent on initial ice stream state. Only for shallow retrograde topography will such behavior occur regardless of the initial position of the grounding line.

4.5 Conclusions and relevance to observations

There are two main conclusions to be drawn from the results of this study. First, we have demonstrated that grounding line position and behavior change significantly as a result of spatiotemporal

variations in bed properties that arise as a part of unforced ice flow variability. While ice streams which have a hard bed or a permanently-saturated soft bed may not necessarily undergo large internal variations in basal shear stress, in a broad parameter regime relevant to observed ice streams, the possibility of a dynamically-evolving soft bed must be considered. As we have shown, models which do not include dynamically-varying bed properties risk missing out on a wide array of ice stream behaviors.

Second, ice stream grounding lines on or near retrograde slopes exhibit behaviors which are seemingly at odds with existing theories for grounding line stability or internal ice stream variability. Ice streams which are far from a steady-state due to internal variability may persist on retrograde slopes for centuries and reverse their direction of migration on such slopes. The marine ice sheet instability is not equipped to explain behavior which occurs so far from steady-state, which complicates how observations of grounding line migration are interpreted. The grounding line of an ice stream retreating onto a section of retrograde slope may continue to retreat irreversibly, or, may pause for centuries during stagnation before re-advancing onto the prograde slope. The latter possibility may explain why the grounding line of the currently stagnant Kamb Ice Stream rests on a retrograde slope (Fried et al., 2014) without evidence for ongoing migration (Horgan and Anandakrishnan, 2006). Distinguishing between these possibilities of irreversible retreat and stagnation before reversal for Kamb and other ice streams is critical in making accurate long-term predictions of ice stream flux and grounding line position. However, determining whether a grounding is undergoing irreversible retreat is complicated by the short observational records of grounding line position for many ice streams, which extend (at most) only a few decades. To make more progress in contextualizing existing observations and predicting future ice stream behavior, numerical models are necessary. To admit the widest range of possible ice stream behavior, ice stream modeling studies must include dynamic variation in bed properties or convincingly argue that such variation is not applicable to a particular ice stream.

There are 3-D thermomechanical ice stream models which include more processes than the simple flowline model utilized in this study. The simplicity of this flowline model enables robust exploration of the parameter space, process-level understanding of dynamical behavior and comparison to theories of grounding line stability and ice stream variability. Robel et al. (2014) showed that strong ice shelf buttressing, as parameterized by a buttressing parameter, may play a role in suppressing thermal oscillations, and consequently may dominate ice stream dynamics under some circumstances. More accurately determining the importance of buttressing would require a model with a fully dynamic ice shelf, including uncertain processes such as calving. However, to the extent that oscillations in velocity and grounding line position occur in some ice streams - and observations show that they do - the dynamics discussed in this study are relevant and likely play a role in more realistic models as well as observed ice streams. Nonetheless, in order to draw definitive conclusions about specific ice streams, more complete 3-D ice stream modeling is needed, which takes into account variations in bed properties simulated in this study and also details not captured by a flowline model, such as cross-stream variations in basal topography.

We do not challenge the notion that an unbuttressed ice stream with a Weertman sliding law cannot have a stable steady-state grounding line on a retrograde bed slope (excluding other physical processes). However, there are limitations in trying to fit all observed ice sheet dynamics to this simple version of the marine ice sheet instability. Indeed, recent studies have shown that an array of potentially important processes not included in the classical formulation of the marine ice sheet instability may inhibit it. Other studies (Schmeltz et al., 2002; Joughin et al., 2009, 2010; Parizek et al., 2013) have also shown that forced simulations of unstable grounding line migration over retrograde slopes are highly sensitive to assumptions about bed properties. The simulations presented here show the types of grounding line behavior that are possible once we step away from the limiting confines of the marine ice sheet instability with a static bed.

A new generation of observations (Schroeder et al., 2013; Smith et al., 2013) has provided some

indirect indications that subglacial hydrology may provide a stabilizing feedback in situations where there is high basal shear stress near the grounding line of an ice stream under significant external forcing, such as ocean melting. However, the paucity of direct observations of bed conditions over most of West Antarctica, including the presence (or lack) of plastic till and meltwater and their time-dependent evolution, is still a major obstacle to making accurate predictions of ice stream evolution. Future studies must continue to find new ways to make observations of bed properties, which can be incorporated into models with dynamically evolving subglacial hydrology. Such an approach would enhance dynamical understanding of ice sheet stability and improve predictions of Antarctic Ice Sheet change.

5

The Role of Ice Stream Dynamics in Deglaciation

5.1 Introduction

The 100 kyr glacial oscillations that have occurred since the mid-Pleistocene transition (Huybers, 2007) have been marked by rapid transitions from glacial to interglacial states. Milankovitch forcing is commonly believed to have paced these transitions (Hays et al., 1976), likely due to nonlinear phase locking (Hyde and Peltier, 1987; Gildor and Tziperman, 2000; Tziperman et al., 2006). Ice sheets experience several precession (26 kyr) and obliquity (41 kyr) cycles before responding with a full deglaciation when the ice sheet is large, leading to the 100 kyr glacial-interglacial period. However, rapid deglaciations of large ice sheets cannot be explained by the magnitude of Milankovitch forcing, and internal feedbacks within the climate system likely played a dominant role in producing the asymmetry between slow glaciation and rapid deglaciation and the 100 kyr period. Numerous feedbacks have been suggested, including changes in sea ice cover that affect albedo, air-sea fluxes or storm track and therefore moisture supply to ice sheets (Gildor and Tziperman, 2000; Li et al., 2005); changes to the thermohaline circulation (Broecker and Denton, 1989; Paillard, 1998); CO_2 feedbacks, including its ventilation from the deep ocean due to circulation and sea ice changes (Toggweiler, 1999; Gildor et al., 2002; Stephens and Keeling, 2000); albedo variations due to atmospheric dust loading (Peltier and Marshall, 1995), and more.

These climate feedbacks have had limited success in explaining rapid deglaciation, and glaciological feedbacks have therefore been considered as well. This includes the height-mass balance feedback, wherein an ice sheet that is lowering in elevation experiences increasing surface melting and further lowering, potentially leading to a runaway ice sheet collapse (Weertman, 1961). Another example involves the isostatic adjustment to the load of an ice sheet (Oerlemans, 1980; Pollard, 1982), although these feedbacks seem still insufficient to explain the full extent of rapid deglaciation (Abe-Ouchi et al., 2013). Models based on such feedbacks seem occasionally successful at reproducing fast deglaciations, but are highly idealized with respect to ice sheet dynamics, suggesting that there is

much more to be understood about the detailed physical mechanism of rapid ice sheet collapse.

Millennial-scale glacial climate variability points to ice streams as a possible processes capable of producing rapid ice sheet change even in the absence of Milankovitch forcing. Heinrich events are one example, where large iceberg discharge events are thought to be the result of flow variability of the Hudson Strait Ice Stream caused by either internal variations in subglacial thermal state (MacAyeal, 1993) or ocean-induced collapse of a buttressing Labrador Sea Ice Shelf (Marcott et al., 2011). Extant geomorphological evidence indicates that many such ice streams were found throughout the Laurentide and Eurasian Ice Sheets (Stokes and Clark, 2001). They are also common in the modern Antarctic and Greenland Ice Sheets, where glaciological observations show evidence for similar flow variability in the last 1000 years (Retzlaff and Bentley, 1993; Catania et al., 2012). Despite this considerable evidence that ice streams were a player in millennial glacial variability, the dynamics of ice stream variability during glacial terminations is still not well-understood, and this paper attempts to make progress on this front.

Clark et al. (1999) suggested that since the mid-Pleistocene transition, the advance of large ice sheets onto marginal soft-bedded regions where ice streams may form has almost always been a precondition for deglaciation. Stokes and Tarasov (2010) show that variations in the mass flux through topographic ice streams are indeed strongly associated with the spatiotemporal progression of deglaciation. Geothermal heat flux at the base of a thick ice sheet leads to subglacial melting and is hypothesized lead to ice sheet collapse (e.g., Marshall and Clark, 2002; Huybers and Tziperman, 2008). This assumes, explicitly or implicitly, that the gradual development of ice streams under temperate bed conditions raises the potential for rapid ice sheet collapse.

In parallel to these conceptual and model-based investigations of ice stream activity during deglaciation, new methods for interpreting geomorphological observations have revealed complex ice stream behavior during deglaciation. Stokes et al. (2009) found evidence of major ice stream discharge events during deglaciation of the Northwestern margin of the Laurentide Ice Sheet around 14.1 kyr

BP, roughly corresponding to the timing of Meltwater Pulse 1a. Margold et al. (2015) calculated the proportion of the ice sheet margin undergoing fast flow at different times during deglaciation, to conclude that during the LGM, the Laurentide Ice Sheet had a similar level of streaming as the modern West Antarctic Ice Sheet (as judged by fraction of the margin showing evidence of ice streaming), but later in the deglaciation (after 12 kyr BP), streaming was greatly reduced, consistent with other estimates (Shaw et al., 2006; Stokes and Tarasov, 2010).

Geomorphological observations and coarse resolution shallow ice models have raised new questions regarding the role of ice streams in deglaciation. Providing answers to these new questions may now be possible due to the advent of ice sheet models that can robustly resolve ice streams and simulate the evolution of subglacial till properties in simulations lasting 10^5 years or more. This study uses such an ice sheet model to perform simple, idealized simulations probing the response of an ice sheet to a prescribed change in surface conditions, corresponding to raising of equilibrium line altitude and sea level atmospheric temperature. The development of ice streams during ice sheet growth is demonstrated to play a key role in the increased sensitivity of large ice sheets (in accordance with the speculation of Marshall and Clark, 2002). Forcing climate by raising equilibrium line altitude causes a rapid deglaciation due to ice stream acceleration and the resulting increase in discharge rate and surface melting in ice streams. The fundamental cause can be traced to increasing driving stress in ice stream onset zones. It is shown that coarse resolution ice sheet models similar to those used in many paleoclimate simulations do a poor job of resolving ice stream activity and consequently are unable to accurately simulate the ice sheet response to forcing which is demonstrated here.

This paper is organized as follows. Section 5.2 introduces the ice sheet model and the configuration of climate forcing simulations. Section 5.3 describes ice sheet build-up, deglaciation, the role of ice streams in enhancing the large ice sheet sensitivity to forcing, and the robustness of the response under slower forcing. Section 5.4 demonstrates the importance of resolving ice streams in simulating the full deglaciation of ice streams. Sections 5.5 and 5.6 conclude by discussing the relevance of these

simulations to observations and the potential for ice stream interactions with other components of the Earth system.

5.2 Model Configuration

To simulate an ice sheet with the capacity to form dynamically-evolving ice streams, we employ the Parallel Ice Sheet Model (PISM), a 3D thermomechanical ice sheet model. We use the hybrid force balance scheme (Bueler and Brown, 2009), a composite of the shallow ice and shallow shelf approximations for ice sheet flow (discussed in chapter 1). Critically, this hybrid force balance scheme includes viscous stresses lateral to the dominant direction of ice flow and admits the possibility of ice stream formation in locations with weak basal resistance. For the idealized bed topography used in this study, the hybrid force balance provides a robust approximation to solutions of the full set of Stokes flow equations. With the exception of section 5.4, all model simulations are performed on a horizontal rectangular grid with 5 km resolution and a quadratic vertical grid with 40-200 m resolution (see full model description in Bueler and Brown, 2009).

The idealized bed configuration has an axisymmetric topography, with a flat continental interior, rapidly falling away below sea level at 1000 km from the domain center,

$$b(r) = 100 \left[1 - \left(\frac{r}{10^6} \right)^8 \right] \text{ meters}, \tag{5.1}$$

where $r = \sqrt{x^2 + y^2}$ is the distance from the center of the domain in meters.

The bed is assumed to be till-covered everywhere. Basal sliding over the till is governed by a Mohr-Coulomb plastic friction law (Truffer et al., 2001; Schoof, 2006b). The yield stress of the till is,

$$\tau_c = (\tan \varphi)\, N_{till}, \tag{5.2}$$

where φ is a specified till friction angle and $N_{till} = N(W_{till})$ is the effective pressure at the ice-till interface, which is determined by the local till water content. Our idealized configuration includes prescribed regions of weak till where ice streams are permitted to form. The weak till strips are all 40 km wide, beginning at the center of the domain and radiating outward to the edge of the domain. In the weak till strips, the till friction angle is set sufficiently low ($\varphi = 10^\circ$) to permit significant basal motion when the till is saturated with meltwater. Elsewhere, a uniform, high till friction angle of $\varphi = 80^\circ$ is specified, which ensures that the yield stress is not achieved and there is no basal motion (even when the till is saturated with meltwater). The bed is configured in this way so that the the proportion of the full simulated ice sheet margin undergoing ice streaming can be set to a level resembling that inferred from geomorphological observations of the Laurentide Ice Sheet at the Last Glacial Maximum. We have elected not to prescribe ice stream location and width by inserting troughs in bed topography (Kyrke-Smith et al., 2015), to exclude the potential for grounding line instabilities, which are beyond the scope of this study.

The effects of changing climate forcing caused by orbital variations are specified through surface mass balance (accumulation minus melting) and surface atmospheric temperature. The surface mass balance ($\mathcal{M}$) depends on the vertical distance from the ELA as follows,

$$\mathcal{M}(H) = \begin{cases} \beta(H - H_{ELA}) & \text{if } H < H_{ELA} + H_R \\ \beta H_R & \text{if } H \geq H_{ELA} + H_R, \end{cases} \tag{5.3}$$

and increases linearly with ice sheet surface elevation at a rate β until a specified runoff elevation, where surface mass balance is assumed to reach a constant. We represent the effects of Milankovitch forcing and climate effects via spatially-uniform changes to the equilibrium line altitude (ELA, or H_{ELA} in equation 5.3), which is the elevation at which the net surface mass balance is zero. This specification of elevation-dependent surface mass balance is used in many modeling studies of ice sheets

and reflects observations of surface mass balance in modern mountain glaciers and ice sheets (e.g., Oerlemans, 2002; Pollard and DeConto, 2005). Sea-level atmospheric temperature (T_s) is specified, and the atmospheric temperature at the ice surface (H) decreases with ice surface elevation according to the dry adiabatic lapse rate ($\Gamma = 9.8°\text{C/km}$),

$$T(H) = T_s - \Gamma H. \tag{5.4}$$

For simplicity we assume that there is melting at the ice surface when the atmospheric temperature is above 0°C. This implies that $T(H_{ELA}) = 0°\text{C}$, or that the ELA is always located where ice surface temperature is at the melting point.

The purpose of this study is to explore the role of ice streams in glacial termination in an idealized configuration that allows us to understand their role in isolation, and we have therefore eliminated many other feedbacks that are expected to play an important role in reality. Where the ice margin is less than 200 meters thick, ice is calved immediately in accordance with observational evidence (Albrecht et al., 2011). Additionally, all floating ice is assumed to immediately calve from the grounded ice sheet, and the model setup therefore does not include buttressing effects by ice shelves. Even if floating ice were not calved, the simplified bed topography precludes strong buttressing effects from occurring in these simulations. Though external ocean forcing on ice shelves is potentially an important component of climate forcing leading to ice sheet deglaciation, it is beyond the scope of the current work with its idealized approach, allowing us to focus on different processes. Additional climate and Earth system components are not included, but may be expected to further amplify the stand-alone ice sheet response to external forcing (see section 5.5 for further discussion).

5.3 The sensitivity of large ice sheets to forcing

The primary goal of this study is to determine the sensitivity of an ice sheet, via ice stream activity, to a change in climate forcing at different stages during its growth. As noted in the introduction, ice sheets experience several precession and obliquity cycles to which they do not respond with a full deglaciation until the ice sheet is large. Milankovitch forcing has been related to changes in the ELA (Ghil and Treut, 1981; Ghil, 1994). Our methodology for approaching this problem is therefore to apply a change to the ELA and specified sea level temperature that are motivated by the Milankovitch forcing during several stages during ice sheet development, and see if ice streams tend to be more effective in leading to deglaciation when the ice sheet is large. In the following subsections we first describe the initial spinup to equilibrium of the ice sheet and ice streams (section 5.3.1); we then find that the initial deglaciation response to step change of surface forcing occurs more dramatically when applied to larger ice sheets (section 5.3.2), and includes a significant acceleration in ice stream flux (section 5.3.3). Next, we show that ice stream acceleration leads to rapid deglaciation through a significant increase in discharge at ice stream margins and due to some increased surface melting in ice stream areas (section 5.3.4). Finally, we show that rapid ice stream-mediated deglaciation also occurs when the change in forcing is gradual and more Milankovitch-like rather than step-like (section 5.3.5).

5.3.1 Spinup to equilibrium of the ice sheet growth and ice streams

We start by describing the unforced model spinup run to a steady state. Simulations are initialized in an ice-free state with the equilibrium line at sea level, $H_{ELA} = 0$ m, and with a sea level atmospheric temperature specified to be $T_s = 0°$C. Surface mass balance is therefore positive over the terrestrial portion of the bed ($r < 1000$ km) and the ice sheet begins to grow. Gradually increasing ice sheet thickness insulates the bed and leads to warming of basal ice through geothermal heat flux (Figure

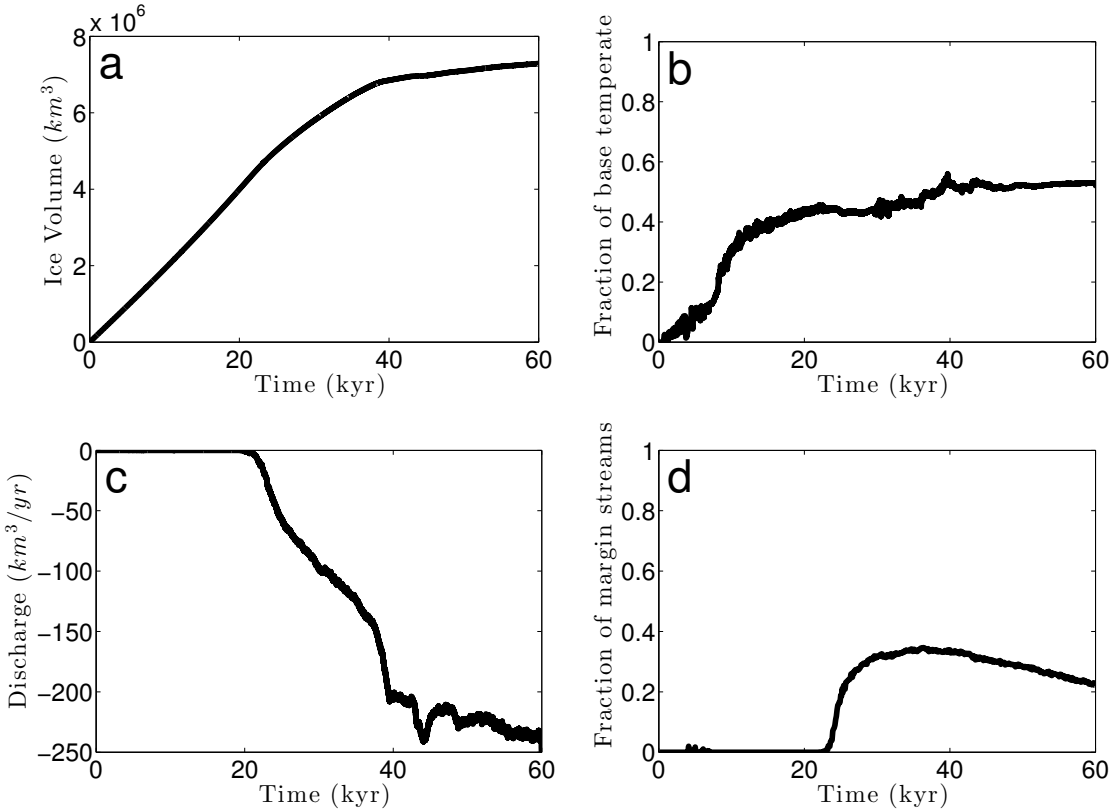

Figure 5.1: Evolution of important diagnostic quantities during ice sheet growth. (a) Ice sheet volume. (b) Percentage of base that is at pressure melting point. (c) Discharge due to calving at margin. (d) Percentage of margin in ice streams.

5.1b). Eventually the ice sheet becomes thick and slow deformational flow expands the margin outward onto the part of the bed that is below sea level, initiating ice calving into the ocean (Figure 5.1c). It is at this point, around 20 kyr in these simulations, that basal sliding is initiated near the ice sheet margin in places where weak till is specified, basal ice becomes temperate and calving at the margins of these ice streams provides a significant sink of mass. Basal sliding leads to a positive feedback of frictional heating at the bed, additional meltwater production, further weakening the bed and increasing basal sliding velocity. Longitudinal stresses coupled with frictional heating at the bed then propagate this sliding 100-200 km upstream, where the bed is sufficiently warm that frictional heating is not immediately dissipated by vertical heat conduction (Price et al., 2008; Robel et al., 2014).

The development of ice streams in this way continues for another 20 kyr until the ice streams and the ice sheet nearly reach a steady state by 60 kyr (Figure 5.1a,d). At steady-state, ice streams compose approximately 30% of the ice sheet margin, which is comparable to the Laurentide Ice Sheet at the Last Glacial Maximum and the modern Antarctic Ice Sheet (Margold et al., 2015).

5.3.2 Ice sheet response to change in forcing

Following our above stated goal and approach, we now apply a step change in climate forcing to the ice sheet at different times through the ice sheet growth, and study the ice sheet and ice stream responses. Figure 5.2 shows the response to a step change in ELA and sea-level atmospheric temperature, with each line representing a change in climate forcing at a different time (every 10 kyr). In all these simulations, the step change in forcing involves increasing the ELA from 0 to 400 m and increasing T_s from 0 to 4°C uniformly over the entire domain. This change in ELA and sea level temperature is in the middle of the range of estimated shifts in Northern Hemisphere climate resulting from Milankovitch forcing (e.g., Andrews et al., 1972; Oerlemans, 2002; Pollard and DeConto, 2005; Ullman et al., 2015). A realistic simulation of deglaciation would require a fully coupled climate and surface mass balance model forced by orbital variations in Northern Hemisphere insolation. This is beyond our idealized process study and so instead, we use a single prescribed magnitude for our change in climate forcing.

When the ice sheet is largest, in the simulations with step forcing applied at 40 and 50 kyr, there is a rapid decrease in ice volume in the 3 kyr following the change in forcing (Figure 5.2a,b). This same rapid initial deglaciation does not occur when the climate forcing is applied to a small ice sheet, and we next analyze the mechanisms involved in this differential response of a large and small ice sheet.

The only terms in the ice sheet mass balance are surface accumulation or melting (equation 5.3), and discharge through calving at the margin. Thus, the ice volume reduction can be decomposed into contributions due to surface mass balance (Figure 5.2c,d) and due to discharge (Figure 5.2e,f).

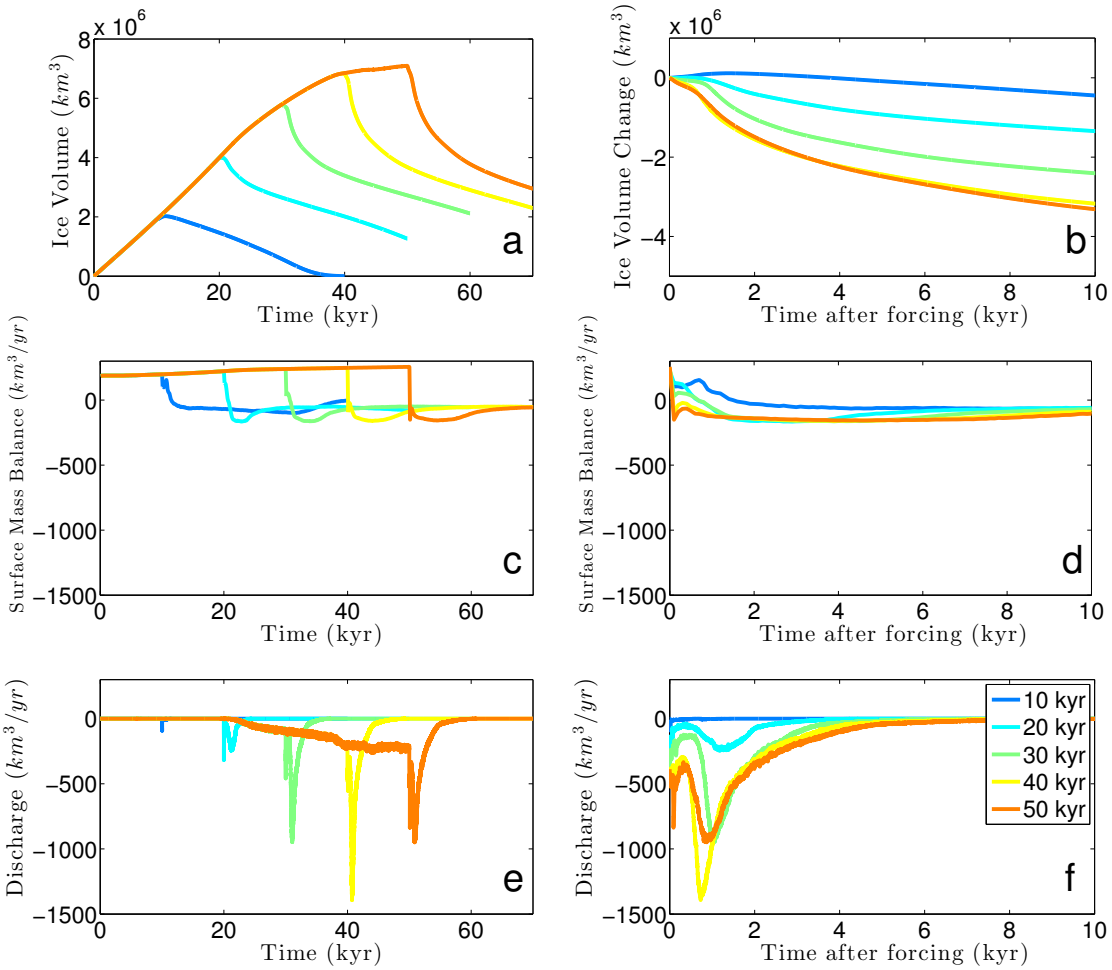

Figure 5.2: Ice sheet response to climate forcing at various times during growth. (a) Ice volume. (b) Change in ice volume with reference to ice volume at time of forcing. (c) Surface mass balance. (d) Surface mass balance following forcing. (e) Discharge due to calving at ice sheet margin. (f) Discharge following forcing.

The step change in ELA directly increases surface melting in all simulations (Figure 5.2c) by a modest amount, followed by some additional increase in the first 4 kyr of deglaciation. However, in simulations where the change in climate forcing is applied to a large ice sheet, it is discharge due to calving at the margin (Figure 5.2e) which dominates the rate of deglaciation in the 4 kyr following that change. After this enhanced discharge diminishes, surface melting takes over as the primary source of mass loss (Figure 5.2c). The remainder of deglaciation then occurs at a similar rate in all

simulations regardless of the initial ice volume (Figure 5.2b). This latter part of the deglaciation is the result of increasing intensity of surface melt driven by decreasing ice sheet surface elevation (the height - surface mass balance relationship, see equation 5.3) over an ice sheet area that continues to shrink. The result is that the integrated surface mass balance leads to a constant rate of mass loss for remainder of deglaciation, as shown in Figure 5.2d.

5.3.3 Ice stream acceleration

The large increase in discharge due to calving at the margins following the change in climate forcing (Figure 5.2e,f) is intriguing and suggests a role for ice stream dynamics. We next show that, indeed, ice streams accelerate in response to the change in forcing, and explain the mechanism for this change. Figure 5.3 shows average basal velocity and driving stress in weak till regions as a function of distance from the margin and time since the change in forcing. Before the change in climate forcing, the ice stream onset zone is 100-200 km upstream of the margin with streaming velocities of 300-500 m/yr at the margin (orange shading for $t < 0$ in Figure 5.3a), and with driving stresses of approximately 50 kPa (Figure 5.3b). After climate forcing is changed, driving stresses in the ice stream onset zone increase (dark red shades in Figure 5.3b). Longitudinal stresses coupled with frictional heating (similar to the mechanism discussed by Price et al., 2008; Robel et al., 2014) then propagate the increased driving stress upstream within 2 kyr. This weakens till upstream and extends the ice stream onset zone to 300-400 km upstream of the margin, where driving stresses are now 60-70 kPa. The higher driving stresses in the onset zone are accompanied by faster ice stream velocities throughout the ice stream (Kamb and Echelmeyer, 1986), including higher velocities near the margin of 1000-1500 m/yr. The ice stream acceleration persists for just over 5 kyr following the change in climate forcing.

We explain that ice stream acceleration is a consequence of the dependence of the surface mass balance on elevation, as follows. In thick continental ice sheets, like the one we are simulating in

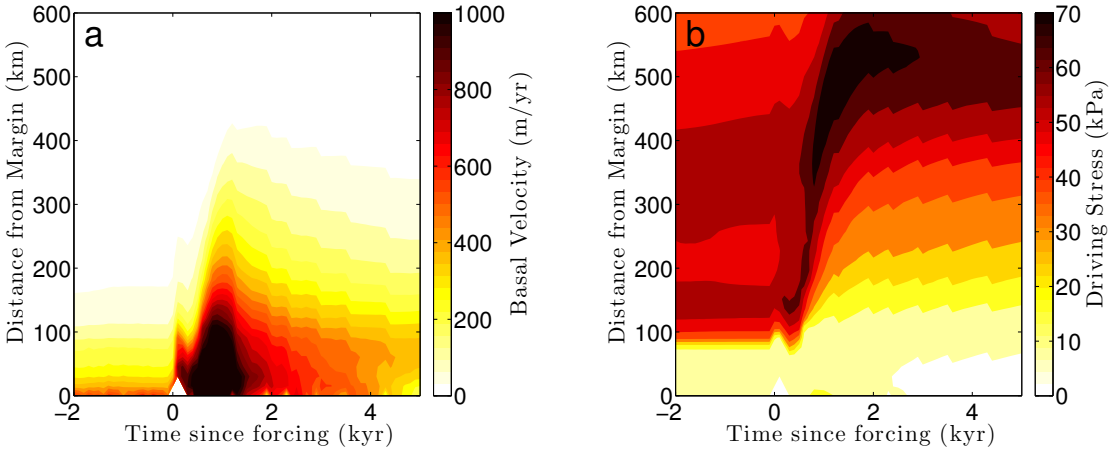

Figure 5.3: Mechanism of ice stream acceleration. In both panels, the x-axis is time since climate forcing and the y-axis is the distance from ice sheet margin (radial distance upslope from margin). All quantities are averaged over a radial distance from the center of the domain. (a) Basal ice velocity. (b) Driving stress.

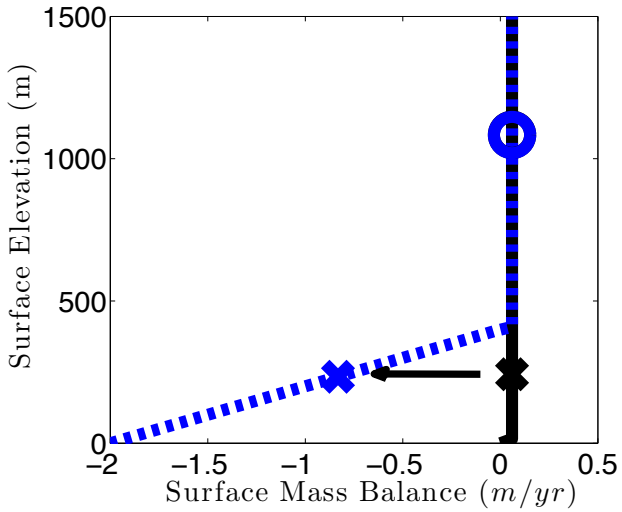

Figure 5.4: Surface mass balance changes due to change in climate forcing. Crosses indicate SMB at a typical ice stream elevation. Open circles denote typical SMB in ice dome location, upstream of ice streams. Black line and markers indicate surface mass balance just before the change to climate forcing is applied. Blue dash line and markers indicate surface mass balance just after.

this study, surface mass balance becomes more positive with elevation due to the reduction in both surface melting and accumulation, and then saturates and does not change further with height (at

the runoff elevation in equation 5.3). This saturation amounts to a negative curvature of the surface mass balance as function of elevation, $\mathcal{M}(H)$. In the simulation analyzed here, the region upstream of the ice stream in the central ice dome begins above this elevation of saturation and therefore undergoes little to no change in surface mass balance due to the applied change to the ELA (open circles in Figure 5.4). On the other hand, the low-elevation ice stream trunk areas begin above or near this elevation of saturation and ends below it (crosses in Figure 5.4) where surface melting increases with decreasing elevation. The result is that an upwards shift in ELA causes the ice stream to lose mass faster than the ice dome, enhancing the ice surface slope between them, in the onset zone. This increases driving stress at the ice stream onset zone, which then leads to ice stream acceleration.

The same argument can be made mathematically as follows. Ice stream thickness decreases everywhere during deglaciation, thus the increase in onset zone driving stresses is the result of steepening ice surface slope. We can understanding the cause for this steepening of the ice surface by referring to a simple mass conservation equation with a mass source $\mathcal{M}(H)$,

$$\frac{\partial h}{\partial t} = \mathcal{M}(H) + \frac{\partial}{\partial x}\left(uh\right), \tag{5.5}$$

where $H = h + b$ is the ice surface elevation. Differentiating with respect to x, we have an equation for the evolution of ice thickness slope

$$\frac{\partial}{\partial t}\left(\frac{\partial h}{\partial x}\right) = \frac{\partial \mathcal{M}}{\partial H}\frac{\partial H}{\partial x} + \frac{\partial}{\partial x^2}\left(uh\right). \tag{5.6}$$

At steady-state, the two terms on the right hand side balance each other. If there is a change in $\partial\mathcal{M}/\partial H$, before u and h adjust, there will be a tendency in surface slope, $\partial h/\partial x$. In our simulations, a step increase in ELA (which shifts the $\mathcal{M}(H)$ profile up) will result in steepening h_x in a

region of interest if $\partial \mathcal{M}/\partial H$ increases. In mathematical terms, if

$$\frac{\partial^2 \mathcal{M}}{\partial H^2} < 0, \tag{5.7}$$

then an increase in ELA results in a steepening of the ice surface. As we have already noted, the presence of a runoff line gives $\mathcal{M}(H)$ negative curvature and so results in steepening in our simulations.

The above discussion centers on the effect of ELA change. It turns out that the change we apply to the sea level atmospheric temperature has only a small effect on the model response. Specifically, the resulting change in ice stream surface atmospheric temperature does not appear to effect till water content and therefore basal shear stresses (not shown) in ice stream regions. We conclude that the change is surface atmospheric temperature plays little role in this ice stream acceleration. This is consistent with the argument of Marshall and Clark (2002) that pre-existing ice streams enable ice sheets to respond more strongly to a change in forcing, but that surface temperature forcing plays almost no role in the response.

Our simulations show that the enhancement of discharge in non-ice stream regions as a result of the change in forcing is negligible compared to the acceleration in ice stream flux, and this can be understood in terms of the above arguments. The low elevation of ice streams implies a jump in ice sheet elevation near their onset region. This then allows the surface mass balance to change over the ice streams but not in the onset areas, leading to the steepening and acceleration. Areas with no ice streams only have low elevation close to the margin, and only there can the response of the surface mass balance to the change in forcing lead to the same steepening. This implies that enhanced driving stresses resulting from climate forcing are limited to a narrower region near the ice margin, where the response is less strong as they must contend with a strong bed which only allows slow flow through ice deformation.

5.3.4 The role of ice streams in ice sheet deglaciation

We next show how ice stream acceleration leads to rapid deglaciation through increased ice stream discharge at the margin and, to a lesser degree, due to increased surface melting in ice stream areas. We again focus on the single simulation denoted by the orange line in Figure 5.2, where the change in forcing is applied at 50 kyr.

Consider first the increased discharge by ice streams at the margin. For this purpose, this discharge is decomposed into that due to ice streams, defined as locations where basal velocity is over 100 m/yr, and due to non-ice stream flow (Figure 5.5a). Following the change in forcing, there are two spikes in discharge at the ice sheet margins. The first spike in discharge is small and immediately follows the climate forcing, with similar magnitudes in ice stream and non-ice stream regions. This is the result of surface melting causing the ice margin to reach the flotation thickness and trigger. The second spike in discharge is an order of magnitude larger than the first, peaks in intensity 800 years after the change to climate forcing and the discharge returns to pre-forcing levels after 3 kyr. It is due entirely to increasing discharge through ice stream margins (blue line in Figure 5.5a). The ice sheet margin retreats continuously through deglaciation, with non-ice stream margins becoming mostly terrestrial (and non-calving) after 2 kyr following the forcing change, while ice-stream margins become mostly terrestrial after 5 kyr. The large flux through ice streams ensures that they will remain marine-terminating for much longer than the rest of the ice sheet.

The second way in which ice streams contribute to deglaciation after the change in forcing is through their contribution to the surface melting. Decomposing surface mass balance into that occurring over ice stream areas and non-ice stream areas (Figure 5.5b), we see that the total surface mass balance (accumulation minus melting) is lower in areas occupied by ice streams both at a steady state and after the forcing is applied (when there is net melting over ice stream areas). This is because areas occupied by ice streams have a lower elevation due to the fast flow there (Figure 5.5c). However,

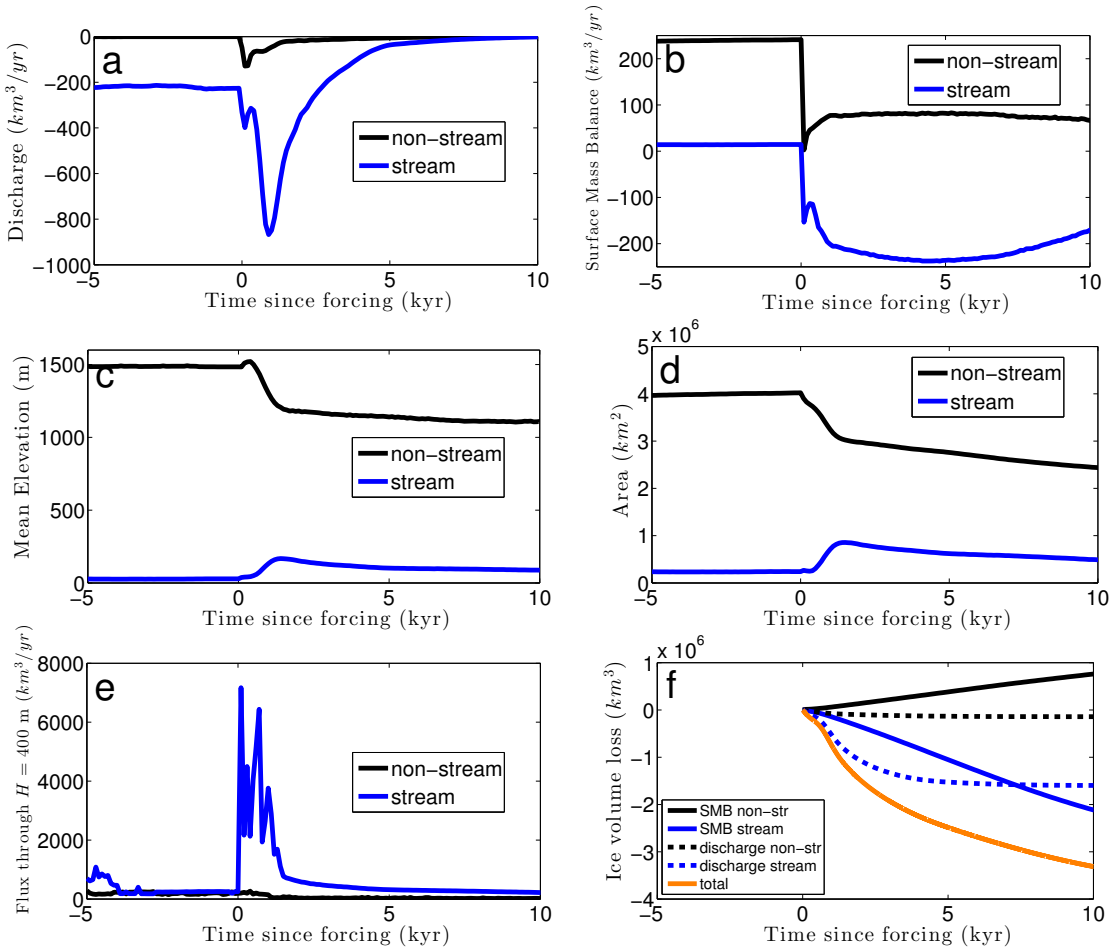

Figure 5.5: Decomposition of ice sheet diagnostics into ice stream and non-ice stream components. (a) Contribution to mass balance by discharge due to calving following forcing. (b) Surface mass balance following forcing. (c) Mean elevation following forcing. (d) Area following forcing. (e) Ice volume flux through the $H = 400$ m elevation contour following forcing. (f) Ice volume loss following forcing decomposed into components due to: surface mass balance in non-ice stream regions (black solid line), surface mass balance in ice stream regions (blue solid line), discharge from non-ice stream regions (black dashed line), discharge from ice stream regions (blue dashed line) and the total mass loss (orange line, as in Figure 5.2b). In all panels black line is in non-streaming regions defined as basal velocity less than 100 m/yr, blue line is in streaming regions defined as basal velocity greater than 100 m/yr.

for 4 kyr after the change in forcing is applied, surface mass balance in ice stream regions continues to decrease and becomes more negative, while remaining nearly constant (and positive) in non-ice stream regions (Figure 5.5b). The different response of surface mass balance in ice stream areas is partly the result of upstream expansion of ice streams, bringing more of the ablating ice sheet area into the ice streaming region (Figure 5.5d). Additionally, ice stream acceleration transports an enhanced flux of ice through the upward-shifted ELA, bringing ice from accumulation regions to the ablation zone (Figure 5.5e). What little volumetric ice flux is conducted through non-ice stream regions is not enhanced after the change in forcing, and in fact it diminishes to almost zero within 2 kyr following forcing (Figure 5.5e).

In Figure 5.5f, the ice sheet volume during the rapid deglaciation identified in section 5.3.2 (orange line) is decomposed into contributions due to accumulated surface mass loss and discharge due to ice-stream and non-stream regions of the ice sheet. The total volume loss is explained almost entirely by increased ice stream discharge (blue dashed line) and surface mass loss (blue solid line) in the first 3 kyr and thereafter is maintained by continuing surface mass loss in ice streams. Even after the change to climate forcing, non-ice stream regions continue to gain ice volume through a positive surface mass balance (black solid line in Figure 5.5f). Ultimately, we conclude that it is enhanced ice stream discharge which accounts the rapid deglaciation of large ice sheets. Not until 8 kyr after the change to climate forcing does ongoing surface mass loss in low-elevation ice stream regions overtakes discharge as the source of the majority of mass loss during deglaciation (where the solid and dashed blue lines cross in Figure 5.5f).

5.3.5 Robustness to the temporal structure of the specified forcing

The climate forcing used in this study thus far has been a step function in ELA and sea level atmospheric temperature. In reality, the change in climate forcing due to changing orbital parameters, say precession effect on summer insolation, takes approximately 10 kyr. It is possible that ice stream

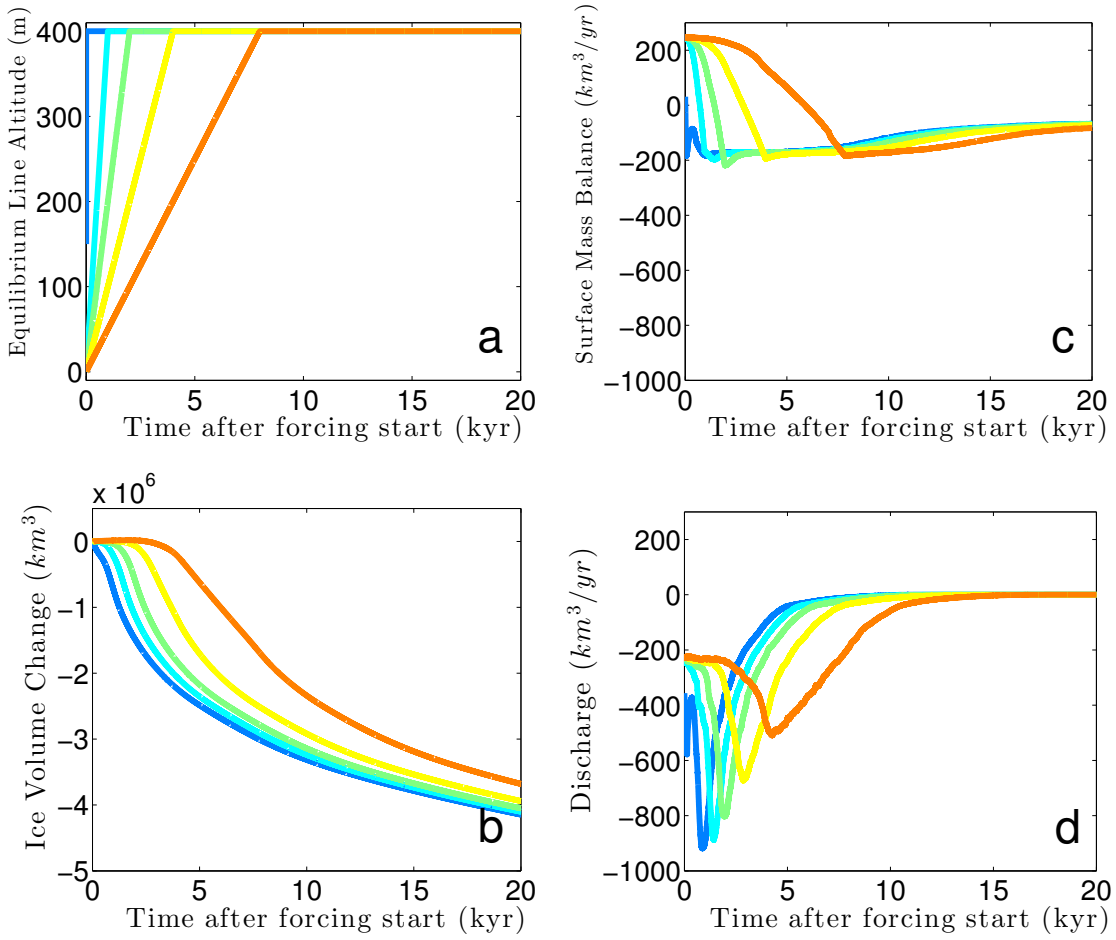

Figure 5.6: Ice sheet response in simulations with differing rates of changing climate forcing. (a) Specified equilibrium line altitude. (b) Change in ice volume following start of forcing change. (c) Surface mass balance following start of forcing change. (d) Discharge due to calving at the ice sheet margin following start of forcing. All curves in panels c and d are smoothed with a 100 year filter from raw model output to eliminate sub-centennial numerical noise.

adjustment in response to steepening may occur faster than the time scale of the change in forcing, thus potentially negating the ice stream acceleration mechanism. To test the robustness of our previous results to the time scale of the specified forcing, we perform a series of simulations where the same change in climate forcing as in earlier simulations is linearly ramped up over some time period. Figure 5.6 shows the ice sheet response to a series of such climate forcing scenarios. Accelerated ice stream discharge is still present, though it is slightly delayed from the start of forcing, spread out

more over the period of ongoing forcing (Figure 5.6d) and longer lasting after forcing is over. The rate of surface mass loss increases gradually over the forcing ramping period (Figure 5.6c), including the enhancement due to ice stream stream acceleration. Regardless, enhanced ice stream discharge results in the same total mass loss throughout the ramping period of climate forcing and in the following 5 kyr, with a slightly delayed onset. We find that the earlier conclusions are therefore robust to these slower and more realistic forcing scenarios.

5.4 The importance of resolving ice streams

We demonstrate above that the acceleration of narrow ice streams strongly contributes to rapid deglaciation. Geomorphological observations (Stokes and Clark, 2001) indicate that though there were some large ice streams ($>$ 50 km wide) active in paleo-ice sheets, most paleo-ice streams were smaller ($<$ 50 km) and more similar to those currently found in the Siple Coast region of the West Antarctic Ice Sheet. However, model studies of paleo ice sheets require long integrations of 10^4 to 10^5 years and consequently tend to use coarse horizontal resolution of 20-100 km. Thus, they may not able to fully resolve most of the ice streams known to contribute to paleo ice sheet flow. Furthermore, most paleoclimate studies use shallow ice models which are only capable of resolving topographically constrained ice streams (e.g., Stokes and Tarasov, 2010; Ganopolski and Calov, 2011; Abe-Ouchi et al., 2013). Simulating ice streams which arise due to weak frictional resistance at the bed and low driving stress requires the inclusion of lateral viscous stresses (Hindmarsh, 2009), which have only recently been incorporated in paleo ice sheet models (Golledge et al., 2012; Pollard et al., 2015). We now demonstrate explicitly the importance of fine horizontal model resolution to resolve ice streams and simulate the full ice sheet volume decrease associated with rapid deglaciation.

We replicate the ice sheet simulation with change in climate forcing applied at 50 kyr (orange line in Figure 5.2) at different horizontal grid resolutions. Figure 5.7 shows the response in simulated

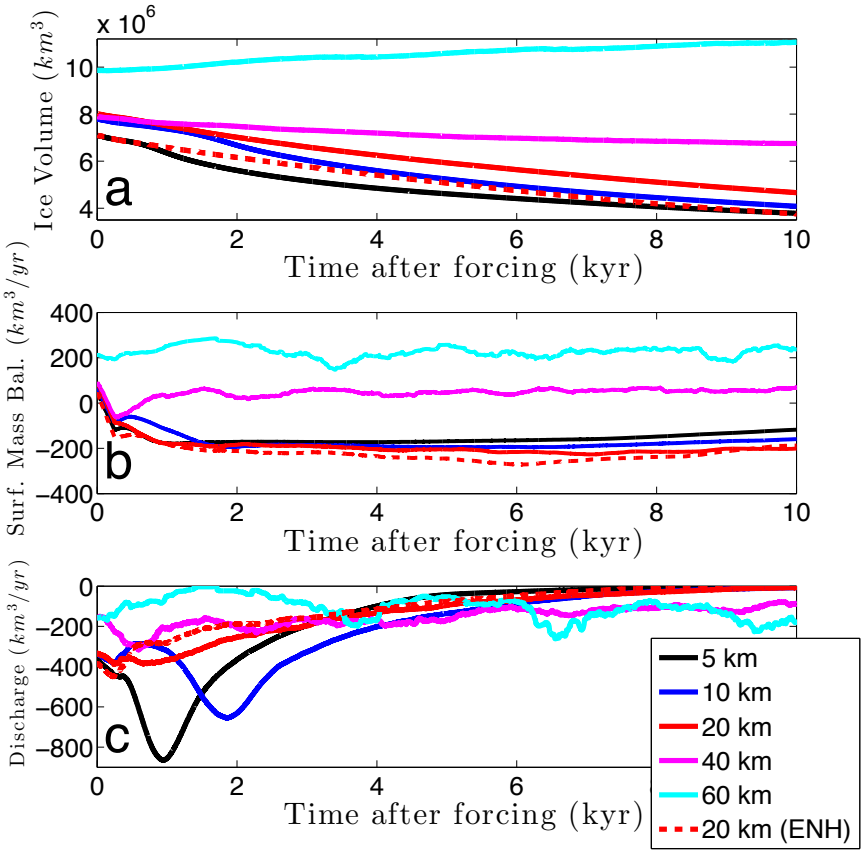

Figure 5.7: Ice sheet response in simulations with differing horizontal model resolution. (a) Change in ice volume following forcing. (b) Discharge due to calving at the ice sheet margin following forcing. All curves in panels b are smoothed from raw model output to eliminate sub-centennial numerical noise.

ice volume, surface mass balance and calving discharge for different horizontal resolutions. The ice volume loss in coarse resolution model simulations (cyan and magenta lines in Figure 5.7a) is considerably slower and more muted or absent entirely in these coarse resolution simulations. This occurs because, at horizontal resolutions coarser than 20 km, the strips of weak till that are specified in the bed configuration (see section 5.2) are either a single grid point wide (magenta) or missed entirely by the grid (cyan). An ice sheet simulated using a coarse grid and with poorly-resolved ice

streams is thicker both in the interior and near the margins, and has a higher surface mass balance before the forcing change (Figure 5.7b). After an upward shift in ELA, most of the thicker ice sheet stays in the accumulation zone, resulting in a smaller decrease in surface mass balance. Even in simulations which would be considered "high resolution" by the standards of paleoclimate modeling (e.g., 20 km), the spike in discharge resulting from ice stream acceleration is diminished considerably (red line in Figure 5.7c) compared to higher resolution simulations. Using only a few grid points to simulate the cross-ice stream variation in velocity under-resolves the lateral viscous stresses which contribute to high ice stream velocities (Hindmarsh, 2009). Thus, even if our ice sheet only included large ice streams of 60-80 km width, horizontal resolution of 20 km would likely still be too coarse to accurately simulate the full ice sheet response to forcing. Only the highest resolution (5 and 10 km) appear to capture the full acceleration in ice stream discharge which produces rapid deglaciation following a change in climate forcing.

A frequent problem in coarse-resolution ice sheet modeling is a mismatch between simulated ice sheet volume and proxy measurements (as pointed out by Huybrechts, 1996; Tarasov and Peltier, 2004; Zweck and Huybrechts, 2005; Ganopolski et al., 2010). One common strategy to fix this problem is tuning ice flow "enhancement parameters" which take advantage of the large uncertainty in physical and chemical ice properties to modify effective ice viscosity and obtain a better fit between the modeled ice sheet and observations. Our results offer a complementary perspective on the use of enhancement parameters. We suggest that differences in both the steady state ice sheet volume and the ice sheet evolution during deglaciation can be caused by the ability of the model to resolve ice stream dynamics, rather than by use of an incorrect enhancement parameter.

Figure 5.7a shows that different resolutions lead to a different near steady state ice volume (at $t = 0$ kyr, just before applying the change in climate forcing). At least some of this difference is due to the ability of the model to resolve ice streams. Next, we contrast the use of an enhancement factor with the effect of properly resolving ice streams. To do so we tune the peak ice volume of the

20 km resolution simulation (red solid line in Figure 5.7) to match the 5 km resolution simulation (black line) by using an enhancement parameter of 3.5 both for the shallow ice and shallow shelf effective viscosities. In the first 3 kyr following the change to climate forcing, the deglaciation of the enhanced 20 km simulation (red dashed line) is slower than the 5 km simulation without enhancement. This is due to the absence, in the enhanced 20 km simulation, of a spike in discharge which drives the rapid response in the 5 km simulation (Figure 5.7c). We see that using enhancement parameters may represent the introduction of compensating errors, where an error in the tuned effective viscosity compensates for errors resulting from the under-resolution of ice streams. Although enhancement parameters can be an effective tool for modifying ice sheet volume and topography to match observations at a single point in time, they cannot at the same time effectively replicate the time-dependent ice sheet response to forcing which, as we have shown, is driven by ice stream acceleration.

5.5 Relevance to observations and discussion

The changes in ice stream activity during deglaciation simulated in this study are broadly consistent with ice stream changes inferred from geomorphological observations. We have shown that accelerated ice stream discharge is the dominant source of mass loss in the first few thousands of years of deglaciation following a change in climate that is motivated by Milankovitch forcing. In simulations of Laurentide Ice Sheet deglaciation that are constrained by geological observations, Stokes and Tarasov (2010) found a similar ice stream acceleration due to increased surface slopes in onset zones, though the steepening mechanism there is not made explicit. As we argue in section 5.4, such coarse resolution ice sheet simulations only resolve very large ice streams and so likely underestimate the rate of deglaciation. Additionally, as we show in section 5.3.4, ice streams decelerate and retreat about 5 kyr after the change in climate forcing that induces the deglaciation (Figure 5.5). This is con-

sistent with the geomorphological observations of ice stream activity during Laurentide deglaciation (Shaw et al., 2006; Margold et al., 2015), which suggest that ice streams decelerated during the latter half of deglaciation, once they retreated off the continental shelf. It is difficult to compare our simulations to observations of ice sheet change during deglaciation more closely than discussed here. While qualitative geomorphological estimates of ice stream size and activity have greatly advanced our knowledge of ice streaming in paleo-ice sheets (Margold et al., 2015), they cannot yet provide reliable chronologies of ice stream velocity for comparison to model simulations.

The highly idealized change in climate forcing applied here, as well as in some previous studies (Pfeffer et al., 1997; Cutler et al., 2000; Oerlemans, 2003), consists of a shift in the ELA, while maintaining the shape of $\mathcal{M}(H)$ (equation 5.3). In comparison, Ullman et al. (2015) explicitly simulated the surface mass balance of the deglaciating Laurentide Ice Sheet with a full climate model under realistic orbital forcing, and found that slow surface mass accumulation at high elevation changes very little through deglaciation while surface mass loss at low-elevations increases considerably. This is consistent with the consequences of the shifted ELA on the surface mass balance in our simulations, which leads to the interesting dynamic ice stream response.

We also find that ice stream response dominates the mass balance during the beginning of the deglaciation, while surface mass balance only becomes negative during the later part of the deglaciation. This transition happens after about 8 kyr in our gradually ramping climate forcing simulations (section 5.3.5, Figure 5.6). Ullman et al. (2015) also argue that the first half of deglaciation must have been dominated by dynamical losses which we interpret here as the possible effect of ice stream acceleration. They find that surface mass balance (melting) can account for the mass loss during the later parts of the deglaciation, again consistent with our findings.

Our model simulations can also be compared to modern observations. In the last few decades, an acceleration in many Greenland outlet glaciers has been observed. Studies attribute this acceleration in some large outlet glaciers, such as Helheim (Howat et al., 2005) and Jakobshaven (Joughin et al.,

2008; van der Veen et al., 2011), to thinning at low elevations enhancing driving stress upstream. This mechanism is very similar to that shown in this study, though previous studies have not explored an explicit link to the shape of the surface mass balance profile ($\mathcal{M}(H)$ in 5.3). It is possible that the same steepening in ice stream onset regions process which is currently ongoing in some parts of Greenland in response to external changes in climate was also active in marine-terminating ice streams in the Laurentide Ice Sheet during the last deglaciation.

Our idealized modeling approach yields a strong and rapid deglaciation, but it also neglects many other internal feedbacks in the earth system which may interact with and amplify ice stream acceleration. For example, slow isostatic depression of the Earth's surface could potentially lower large portions of an ice stream trunk below sea level, prolonging the period over which ice streams remain marine-terminating and active. Through this mechanism, even a relatively fast adjustment time scale for the bed (i.e., 3 kyr) could prolong the period of ice stream acceleration enough to further enhance the rate of deglaciation. Other feedbacks in the climate system, reviewed in section 5.1, may also amplify ELA changes and sea level atmospheric temperature changes. However, such feedbacks are considered external in this study, as we are focused on identifying and understanding feedbacks internal to the ice sheet system.

Other ice sheet processes not considered here likely contributed to rapid deglaciation in response to a change in climate forcing. Enhanced circulation of warm ocean water in contact with ice shelves and with grounding lines is thought to play a major role in the ongoing acceleration of many Greenland and West Antarctic ice streams (Joughin et al., 2012). Understanding such ocean-forced acceleration requires simulating realistic sub-ice shelf melt rates and changes in the sub-shelf cavity geometry on climatic time scales (Timmermann et al., 2012). Additionally, meltwater produced at the ice sheet surface may drain to the base and cause changes in till strength or subglacial drainage networks which may be present. Such supraglacial lake drainage events (Stevens et al., 2015) and the evolution of subglacial conduits (Schoof, 2010) are though to play an important role in the ongoing evolution

of the Greenland Ice Sheet and possibly in past deglaciations.

5.6 Conclusions

The main finding of this study is that an acceleration in ice stream discharge greatly enhances the deglaciation of large ice sheets in response to changes in climate forcing, such at those driven by orbital variations. Ice stream acceleration is a direct consequence of increased driving stresses in ice stream onset regions, which are caused by a faster rate of surface melting at low ice stream elevations than at high elevations in the ice sheet interior, following a change in climate forcing. We find that only sufficiently large ice sheets undergo such a rapid deglaciation, because ice streams are activated once there is a sufficiently thick, marine-terminating margin and temperate basal ice. This can potentially help explain why ice sheets experience several precession and obliquity cycles before responding with a full deglaciation when the ice sheet is large. We also find that accurately simulating a rapid deglaciation requires sufficiently fine model resolution that allows ice streams to be resolved. The idealized model simulations showing this ice stream acceleration and rapid deglaciation are broadly consistent with geological observations of the last deglaciation, including a greater importance of ice stream discharge early in deglaciation.

This study highlights the fact that ice flow and surface mass balance are inextricably intertwined and only when coupled together, do they produce the full ice sheet response to a change in climate forcing. The acceleration in ice stream discharge discussed above is induced by a change in the surface mass balance that causes enhancement of driving stress in ice stream onset regions. In turn, ice streams play a role in determining the evolution of surface mass balance. The presence of active ice streams late in ice sheet growth produces a thinner, flatter ice sheet which is then more susceptible to changes in climate. After a change in climate forcing, ice stream acceleration modifies the surface mass balance by rapidly transporting mass from high-elevation accumulation regions to low-

elevation ablation regions. This interplay between ice flow and surface mass balance can inform the interpretation of studies which simulate deglaciation by relying on surface mass balance and neglecting ice streams, by noting that some changes in surface mass balance are due to ice stream acceleration.

6

Conclusions

This dissertation has investigated the dynamics of ice streams, regions of fast flow in ice sheets. As the main conduit by which ice is transported from accumulating regions in the ice sheet interior to calving regions at the ice sheet margin, ice streams are often hotspots of rapid ice sheet change. However, debate remains concerning the dynamical processes controlling ice stream flow on long time scales. Using a range of mathematical tools and a hierarchy of numerical models, this dissertation strived to advance understanding of ice stream variability and dynamical interactions with climate.

In chapter 2, we described a simple mechanism for internal ice stream variability in which variations in the subglacial thermal state can cause centennial- to millennial-scale oscillations in ice stream flow. The mechanism is reproduced in a simple ice stream box model that couples ice flow to subglacial meltwater production. We showed that ice streams exhibit either steady or oscillatory behavior. If geothermal heat flux is high or the ice surface temperature is warm, sufficient meltwater is produced at the ice-till interface to reduce the importance of thickness variations in vertical conductive heat flux, leading to steady-streaming behavior. Alternately, if geothermal heat flux is low or ice surface temperature is cold, then the ice stream will undergo oscillations between active and stagnant flow states. Linear stability analysis confirmed that the occurrence and amplitude of such behavior depends primarily on the ratio of geothermal heat flux to a scaled vertical conductive heat flux. The simplicity of the model enables the derivation of analytic approximations for the stability boundary, amplitude and period of oscillations, which were demonstrated to match sufficiently well to numerical estimates.

Thermally-regulated oscillations in our simple model have period of centuries to millennia, which accords with observations of ice stream variability from both the modern West Antarctic Ice Sheet and Heinrich Events which took place during the last glacial period. We suggested that ice streams in the Siple Coast region of West Antarctica may reside in an oscillatory region of parameter space that is close to the transition to steady-streaming behavior. This transition between steady and oscillatory regimes takes the form of a subcritical Hopf bifurcation. The practical result of such a bi-

furcation is that the transition from a steady to oscillatory ice stream regime takes place at a different location in parameter space than the transition from an oscillatory to steady regime. This theory of thermally-regulated internal ice stream variability can serve as a useful framework for guiding more complex modeling and interpreting observations of ice stream activity.

In chapter 3, we showed how rapid ice stream grounding line migration can be caused by the same thermal-regulation mechanism shown to cause internal ice stream variability in chapter 2. We first described a depth-integrated ice stream flowline model which includes lateral shear stresses and basal shear stresses set by an undrained Coulomb plastic till layer which varies in strength depending on meltwater content. The model exhibits steady and oscillatory behaviors with a subcritical transition between them that can be predicted by the analytic stability boundary approximation from chapter 2. Ice stream activation propagates upstream to the ice divide and downstream to the grounding line, where it initiates ice thickening and advance. Grounding line excursions during activation can exceed 100 km and proceed at rates exceeding 1 km/yr.

On a prograde slope, grounding line retreat is always caused by a negative mass balance near the grounding line, which is not necessarily indicative of a negative mass balance over the entire ice stream. Observations of grounding line retreat, therefore, do not imply net ice stream mass loss, but rather just ice thinning near the grounding line when on a prograde bed. Consequently, when evaluating the possibility of external forcing in modern observations of grounding line migration, the potential for unforced grounding line migration due to internal ice stream variability should also be considered. Additionally, when interpreting glaciological and geomorphological evidence for past grounding line positions, unforced variability of the grounding line position should be considered in addition to externally-forced changes.

In chapter 4, we demonstrated how the interaction of unforced thermally-regulated ice stream variability (explored in chapters 2 and 3) with retrograde bed slopes, can produce grounding line behavior that is unexplained by established steady-state theories of grounding line stability. To do so,

we used the flowline model described in chapter 3 with the addition of a section of retrograde slope placed within the idealized bed configuration. Typical approaches to understanding grounding line behavior on retrograde slopes have maintained bed properties static in time. We showed that allowing bed properties to dynamically evolve significantly changes the range of attainable grounding line behavior.

We found that the grounding line of an ice stream exhibiting unforced variability may stagnate on a retrograde slope for hundreds to thousands of years before reversing its direction of migration. The possibility of this type of behavior must be evaluated when determining whether the retreat of an ice stream grounding line onto a retrograde slope is irreversible. Such a task is complicated by the short observational record, and so we concluded that numerical models used for prediction must include spatiotemporal variations in bed properties which produce the widest possible range of ice stream behavior.

In chapter 5, we suggested that ice streams play a critical role in the rapid deglaciation of large ice sheets. Previous studies have indicated that internal feedbacks within the Earth system are necessary to produce rapid deglaciation. We proposed that ice stream acceleration contributes to rapid deglaciation due to physical processes which have not been previously explored in this context. An idealized configuration of the Parallel Ice Sheet Model which permits the formation of ice streams was used, and was subjected to changes in ELA and sea level temperature motivated by ice age orbital variations. We showed that ice sheets undergo a rapid deglaciation in response to orbital variations only when they are large enough that ice streams have formed. Large ice sheets are sensitive to such forcing due to the acceleration in ice stream discharge. We showed that the rapid deglaciation in response to a change in climate forcing is further enhanced by the contribution of ice stream dynamics to surface melting. We also suggested that resolving ice streams at a sufficiently fine horizontal resolution ($<$ 20 km) is necessary to fully capture the rapid deglaciation. Our simulations showed that ice stream acceleration early in deglaciation is followed by enhanced melting later in

deglaciation, which is broadly consistent with observational studies of Laurentide deglaciation.

We concluded that ice streams, in spite of their relatively small scale, play an important and interesting role in ice sheet variability and stability, and therefore in global climate variability on multiple time scales. To fully represent and understand past and future climate changes, the effects of ice streams must be included.

A

Appendix A (Chapter 2)

A.1 Scaling the reduced model

We write the variables in their scaled forms

$$h = [h]h^* \tag{A.1}$$

$$t = [t]t^* \tag{A.2}$$

$$\tau_d = [\tau_d]\tau_d^* \tag{A.3}$$

$$\tau_b = [\tau_b]\tau_b^* \tag{A.4}$$

$$u_b = [u_b]u_b^*, \tag{A.5}$$

where dimensional scales are bracketed and dimensionless variables are starred.

The first choice of scales is

$$[\tau_d] = \frac{\varrho_i g[h]^2}{L}, \tag{A.6}$$

such that

$$\tau_d^* = (h^*)^2 . \tag{A.7}$$

The form of (equation for sliding velocity) indicates that τ_d and τ_b will have the same scale. Thus, we set $[\tau_b] = [\tau_d]$

$$\tau_b^* = \nu \exp(-c(e - e_c)), \tag{A.8}$$

With $\nu = \dfrac{a'}{[\tau_d]}$. Leading to an expression for $[u_b]$

$$[u_b] = \frac{A_g W^{n+1}}{4^n(n+1)} \left(\frac{[\tau_d]}{[h]}\right)^n, \tag{A.9}$$

and the dimensionless velocity is

$$u^* = \max\left[\left(h^* - \frac{\tau_b^*}{b^*}\right), 0\right]^n. \tag{A.10}$$

We can also go about setting the ice thickness scale using the steady state of the ice thickness equation, which gives

$$a_c L = [h][u_b], \tag{A.11}$$

and then solving for $[h]$

$$[h] = L\left[\frac{A_g W^{n+1}\left(\varrho_i g\right)^n}{4^n(n+1)a_c}\right]^{-\frac{1}{n+1}}. \tag{A.12}$$

A timescale can also be chosen by balancing accumulation with ice thickness change

$$[t] = \frac{[h]}{a_c}. \tag{A.13}$$

These non-dimensionalizations give rise to the scaled form of the undrained system

$$\frac{dh^*}{dt^*} = 1 - h^* u_b^* \tag{A.14}$$

$$m = \begin{cases} \tau_b^* u_b^* + \beta - \dfrac{\gamma}{h^*} & \text{if } w^* > 0 \\ \beta - \dfrac{\gamma}{h^*} & \text{if } w^* = 0 \end{cases} \tag{A.15}$$

$$\alpha\frac{dw^*}{dt^*} = \begin{cases} m & \text{if } w^* > 0 \text{ or } m > 0 \\ 0 & \text{otherwise} \end{cases} \tag{A.16}$$

$$\tau_b^* = \begin{cases} \nu\exp(-c(e^* - e_c^*)) & \text{if } w^* > 0 \\ \infty & \text{otherwise} \end{cases} \tag{A.17}$$

$$u^* = \max\left[\left(h^* - \frac{\tau_b^*}{h^*}\right), 0\right]^n, \tag{A.18}$$

$$e^* = \max\left[e_c^*, w^*\right], \tag{A.19}$$

with the dimensionless parameters

$$\alpha = \frac{\varrho_i L_f}{[t][\tau_d][u_b]} = \frac{L_f}{g[h]^2} = \frac{L_f}{L^2 g}\left[\frac{A_g W^{n+1}\left(\varrho_i g\right)^n}{4^n(n+1)a_c}\right]^{\frac{2}{n+1}} \tag{A.20}$$

$$\beta = \frac{G}{[\tau_d][u_b]} = \frac{G}{a_c \varrho_i g[h]} = \frac{G}{a_c \varrho_i g L}\left[\frac{A_g W^{n+1}\left(\varrho_i g\right)^n}{4^n(n+1)a_c}\right]^{\frac{1}{n+1}} \tag{A.21}$$

$$\gamma = \frac{k_i \Delta T}{[h][\tau_d][u_b]} = \frac{k_i \Delta T}{a_c \varrho_i g[h]^2} = \frac{k_i \Delta T}{a_c \varrho_i g L^2}\left[\frac{A_g W^{n+1}\left(\varrho_i g\right)^n}{4^n(n+1)a_c}\right]^{\frac{2}{n+1}}. \tag{A.22}$$

(The common bracketed term on the right-hand side above represents the inverse of the frictional heating scale.)

α is the ratio of bed relaxation rate to frictional heating rate. β is the ratio of geothermal heating to frictional heating. γ is the ratio of vertical heat conduction to frictional heating. Hereafter asterisks are dropped in subsequent calculations with the non-dimensional system.

A.2 Location of Hopf bifurcation (stability boundary)

The transition in between the two modes highlighted in the text is a Hopf bifurcation. Assuming that the system is not degenerate (which numerical simulations indicate is not the case), then we can determine the stability from the trace of the jacobian (which is also proportional to the real parts of

the eigenvalues)

$$S_t \equiv \mathrm{Tr}(\mathrm{Jac}) = \left.\frac{dF_1}{dh}\right|_{h_\circ, w_\circ} + \left.\frac{dF_2}{dw}\right|_{h_\circ, w_\circ} \tag{A.23}$$

where $F_1 = \frac{dh}{dt}$, $F_2 = \frac{dw}{dt}$ and $h_\circ$ and $w_\circ$ are fixed points. When $S_t = 0$ the system undergoes a Hopf bifurcation from a stable fixed point ($S_t < 0$) to a stable limit cycle ($S_t > 0$). We can find where this transition occurs by solving for $S_t = 0$.

We start by solving for the fixed points. This is simply done by combining equations (A.68) and (A.69), resulting in

$$(h_\circ)^2 + \beta h_\circ - (h_\circ)^{\frac{n-1}{n}} - \gamma = 0 \tag{A.24}$$

This is not trivially solved for $h_\circ$ (though it is nearly quadratic). We will return to this later on in this section.

Next we turn to the stability parameter itself

$$S_t = \frac{d}{dh}(1 - hu) + \frac{d}{dw}\left(\frac{\tau_b u_b + \beta - \frac{\gamma}{h}}{\alpha}\right) \tag{A.25}$$

Before proceeding with calculation of the stability parameter, we will find the scale of each term to determine if one can be dropped. Having scaled the variables, we can easily see that

$$\frac{d}{dh}(1 - hu) \sim O(1) \tag{A.26}$$

The second term is different:

$$\frac{d}{dw}\left(\frac{\tau_b u_b + \beta - \frac{\gamma}{h}}{\alpha}\right) \sim O(\alpha^{-1}) \tag{A.27}$$

for typical parameter values (as in Table 1), $\alpha \sim O(10^{-1})$. So, we see that this second term dominates the first term, which can be dropped from the stability calculation.

Utilizing equations (A.17) and (A.19), we can proceed with the calculation of the stability parameter

$$S_t = \frac{d}{dw}\left(\frac{\tau_b u_b + \beta - \frac{\gamma}{h}}{\alpha}\right) \tag{A.28}$$

$$= \frac{1}{\alpha}\left[-c\tau_b u_b + \frac{nc\left(\tau_b\right)^2}{h}\left(h - \frac{\tau_b}{h}\right)^{n-1}\right] \tag{A.29}$$

$$= \frac{c\tau_b u_b}{\alpha}\left[\frac{n\tau_b}{(h)^2 - \tau_b} - 1\right] \tag{A.30}$$

To find the stability boundary, we set this to zero and rearrange

$$0 = \frac{c\tau_b u_b}{\alpha}\left[\frac{n\tau_b}{(h)^2 - \tau_b} - 1\right] \tag{A.31}$$

$$(h)^2 - (n+1)\tau_b = 0 \tag{A.32}$$

Substituting in equation (A.69)

$$(h)^2 - (n+1)(\gamma - \beta h) = 0 \tag{A.33}$$

$$(h)^2 - \gamma(n+1) + \beta(n+1)h = 0 \tag{A.34}$$

$$\beta = \frac{\gamma}{h} - \frac{h}{n+1}. \tag{A.35}$$

Returning now to equation (A.24), we can substitute in the above expression for β and solve for

h

$$(h_\circ)^2 + \left(\frac{\gamma}{h_\circ} - \frac{h_\circ}{n+1}\right) h_\circ - (h_\circ)^{\frac{n-1}{n}} - \gamma = 0 \tag{A.36}$$

$$(h_\circ)^2 - \frac{(h_\circ)^2}{n+1} - (h_\circ)^{\frac{n-1}{n}} = 0 \tag{A.37}$$

$$h = \left(\frac{n+1}{n}\right)^{\frac{n}{n+1}}. \tag{A.38}$$

On the parameter plane, the stability boundary is thus found at

$$\beta = \left(\frac{n+1}{n}\right)^{-\frac{n}{n+1}} \gamma - \frac{\left(\frac{n+1}{n}\right)^{\frac{n}{n+1}}}{n+1}. \tag{A.39}$$

A.3 The form of the Hopf bifurcation

When (h, w) are near $(h_\circ, w_\circ)$, the dynamics are (generically) governed by the linearization of equations (A.15) and (A.16) about these points. Thus we let $h = h_\circ + h'$ and $w = w_\circ + w'$ and consider the linear system

$$\frac{d}{dt}\begin{pmatrix} h' \\ w' \end{pmatrix} = \begin{pmatrix} M_{11} & M_{12} \\ M_{21} & M_{22} \end{pmatrix} \begin{pmatrix} h' \\ w' \end{pmatrix}, \tag{A.40}$$

where the matrix M depends on α, β, and γ. Explicitly,

$$M = \begin{pmatrix} -\left(nh_\circ^{1/n}(1 + \tau_\circ/h_\circ^2) + 1/h_\circ\right) & nh_\circ^{-1+1/n} \\ -\dfrac{cw_\circ\tau_\circ}{\alpha h_\circ^2}\left(\gamma + n\tau_\circ h_\circ^{1+1/n}(1 + \tau_\circ/h_\circ^2)\right) & -\dfrac{cw_\circ\tau_\circ}{\alpha h_\circ}(1 - n\tau_\circ h_\circ^{-1+1/n}) \end{pmatrix}, \tag{A.41}$$

where $\tau_\circ = ae^{-be_\circ}$ and $\tau' = ae^{-be'}$.

The next step is to make a linear transformation

$$\begin{pmatrix} x \\ y \end{pmatrix} = \begin{pmatrix} a & b \\ c & d \end{pmatrix} \begin{pmatrix} h' \\ \tau' \end{pmatrix} \tag{A.42}$$

such that, along the stability boundary, the system of equations (A.15) and (A.16) takes the form

$$\frac{d}{dt} \begin{pmatrix} x \\ y \end{pmatrix} = \begin{pmatrix} 0 & -\omega \\ \omega & 0 \end{pmatrix} \begin{pmatrix} x \\ y \end{pmatrix} + \begin{pmatrix} f(x,y) \\ g(x,y) \end{pmatrix}, \tag{A.43}$$

with f and g strictly nonlinear functions of x and y. Straightforward computations lead to the simple choice

$$\begin{pmatrix} ab \\ cd \end{pmatrix} = \begin{pmatrix} \mathcal{M}_{21} - \mathcal{M}_{11} \\ -\mathcal{M}_{11} - \mathcal{M}_{12} \end{pmatrix} \tag{A.44}$$

$$\omega = \det \mathcal{M} \tag{A.45}$$

The coefficient which indicates whether the transition is supercritical or subcritical is (Wiggins, 2003)

$$a = \partial_x^3 f + \partial_x \partial_y^2 f + \partial_x^2 \partial_y g + \partial_y^3 g + \frac{1}{\omega} \left[(\partial_x \partial_y f)\Delta f - (\partial_x \partial_y g)\Delta g - (\partial_x^2 f)(\partial_{xg}^2 g) + (\partial_y^2 f)(\partial_{yg}^2 g) \right], \tag{A.46}$$

where everything is evaluated at $h' = w' = 0$. If $a > 0$ ($a < 0$), then the transition is subcritical (supercritical). Here we compute a to leading order in α.

The basic observation is that along $Tr(\mathcal{M}) = 0$ we have

$$\begin{pmatrix} \mathcal{M}_{11} & \mathcal{M}_{12} \\ \mathcal{M}_{21} & \mathcal{M}_{22} \end{pmatrix} = \begin{pmatrix} O(1) & O(1) \\ O(\alpha^{-1}) & O(1) \end{pmatrix} \tag{A.47}$$

$$\begin{pmatrix} ab \\ cd \end{pmatrix} = \begin{pmatrix} O(\alpha^{-1})O(1) \\ O(1)O(1) \end{pmatrix} \tag{A.48}$$

This implies

$$\frac{dx}{dt} = O(\alpha^{-1}) \tag{A.49}$$

$$\frac{dy}{dt} = O(\alpha^{-1}) \tag{A.50}$$

$$\frac{\partial}{\partial x} = O(\alpha) \tag{A.51}$$

$$\frac{\partial}{\partial y} = O(1) \tag{A.52}$$

Noting that $\omega = O(\alpha^{-1})$, we count powers of α and see that only $\partial_y^3 g$ and $(\partial_y^2 f)(\partial_y^2 g)$ can contribute to a. To leading order,

$$a = \partial_y^3 g + \frac{1}{\omega}(\partial_y^2 f)(\partial_y^2 g). \tag{A.53}$$

To leading order, $\partial/\partial y = (\mathcal{M}_{21}/\omega)(\partial/\partial\tau')$, $f = \mathcal{M}_{21}(dh'/dt) - \mathcal{M}_{11}(d\tau'/dt)$, and $g = -\mathcal{M}_{12}(d\tau'/dt)$, where we ignore linear terms in f and g which will vanish after differentiation in a. Hence we need to compute

$$a = -\left(\frac{\mathcal{M}_{21}}{\omega}\right)^3 \mathcal{M}_{12}\frac{\partial^3\varphi}{\partial(\tau')^3} + \left(\frac{\mathcal{M}_{21}}{\omega}\right)^4 \frac{\mathcal{M}_{12}^2}{\omega}\left[\frac{\partial^2\varphi}{\partial(\tau')^2}\right]\left[\mathcal{M}_{21}\frac{\partial^2\psi}{\partial(\tau')^2} - \mathcal{M}_{11}\frac{\partial^2\varphi}{\partial(\tau')^2}\right] \tag{A.54}$$

where $\psi = dh'/dt$ and $\varphi = d\tau'/dt$. Because we take two derivatives of τ', not all terms in ψ and φ

are needed. It is sufficient to take

$$\psi(h', \tau') = -h_0 u'(h', \tau') \tag{A.55}$$

$$\varphi(h', \tau') = -\frac{cw_0}{\alpha}(\tau_0 + \tau')^2(u_0 + u'(h', \tau')), \tag{A.56}$$

with

$$u_0 + u'(h', \tau') = \frac{1}{h_0^n}(h_0^2 - \tau_0 - \tau')^n \tag{A.57}$$

$$u_0 + u'(h', \tau') = \frac{1}{h_0^n}(h_0^{(n-1)/n} - \tau')^n \tag{A.58}$$

$$u_0 + u'(h', \tau') = \frac{1}{h_0}\left(1 - \frac{\tau'}{h_0^{1-1/n}}\right)^n. \tag{A.59}$$

Note that

$$\frac{\partial^2 \varphi}{\partial(\tau')^2} = -\frac{cw_0}{\alpha}\left[2h_0^{-1} + 4\tau_0\frac{\partial u'}{\partial \tau'} + \tau_0^2\frac{\partial^2 u'}{\partial(\tau')^2}\right] \tag{A.60}$$

$$\frac{\partial^3 \varphi}{\partial(\tau')^3} = -\frac{cw_0}{\alpha}\left[6\frac{\partial u'}{\partial \tau'} + 6\tau_0^2\frac{\partial^2 u'}{\partial(\tau')^2} + 3\tau_0^3\frac{\partial^3 u'}{\partial(\tau')^3}\right] \tag{A.61}$$

$$\frac{\partial^2 \psi}{\partial(\tau')^2} = -h_0\frac{\partial^2 u'}{\partial(\tau')^2}, \tag{A.62}$$

up to terms which vanish at $h' = \tau' = 0$.

We notice that the Newtonian case ($n = 1$) is singular. Indeed, in this case

$$a(n=1) = -\frac{cw_0}{\alpha}\left(\frac{M_{21}}{\omega}\right)^3 M_{12}h_0^{-1} - \frac{c^2 w_0^2}{\alpha^2}\left(\frac{M_{21}}{\omega}\right)^4 \frac{M_{11}M_{12}^2}{\omega}\left[2h_0^{-1} - 4\tau_0 h_0^{-1}\right]^2 \tag{A.63}$$

Since $\mathcal{M}_{11} < 0$, $\mathcal{M}_{21} < 0$, and $\mathcal{M}_{12} > 0$, both terms are positive. Hence $a(n = 1) > 0$ and the transition is always subcritical.

In the limit $n \to \infty$ (implicitly we are assuming $n < 1/\alpha$), we can count powers of n to see the dominant terms. With respect to n, $h_0 = O(1)$, $\tau_0 = O(1)$, and all elements of $\mathcal{M}$ are $O(n)$. Each derivative of u' brings down a power of n, hence we see that both terms in a are $O(n)$. We find

$$a(n \to \infty) = -\frac{cw_0}{\alpha}\left(\frac{\mathcal{M}_{21}}{\omega}\right)^3 \mathcal{M}_{12}\frac{3\tau_0^3 n^3}{h_0^{4-3/n}} + \frac{c^2 w_0^2}{\alpha^2}\left(\frac{\mathcal{M}_{21}}{\omega}\right)^4 \frac{\mathcal{M}_{12}^2}{\omega}\left(\frac{\tau_0^2 n^2}{h_0^{3-2/n}}\right)^2 \times \left[-h_0\mathcal{M}_{21} + \mathcal{M}_{11}\frac{cw_0}{\alpha}\tau_0^2\right] + O(1). \tag{A.64}$$

One can compute that $-h_0\mathcal{M}_{21} + \mathcal{M}_{11}\frac{cw_0}{\alpha}\tau_0^2 = O(1)$, rather than $O(n)$ as expected, and hence only the first term in a contributes as $n \to \infty$. This is positive, hence the transition is again subcritical.

Calculation of this parameter for $n = 3$ is non-trivial and likely does not have an analytic form. Numerical experiments appear to indicate that for all $n > 1$ there is a subcritical Hopf bifurcation.

A.4 Boundary between steady-streaming with and without drainage

To find the condition dividing the steady-streaming with drainage from steady-streaming without drainage regimes, we start by looking for fixed points in the undrained limiting case which satisfy

$$0 = 1 - hu \tag{A.65}$$

$$0 = \tau_b u_b + \beta - \frac{\gamma}{h} \tag{A.66}$$

$$u = \left(h - \frac{\tau_b}{h}\right)^n. \tag{A.67}$$

We combine equations (A.65) and (A.67) to

$$\tau_b = (h)^2 - (h)^{\frac{n-1}{n}} \tag{A.68}$$

and combine equations (A.65) and (A.66) to

$$\tau_b = \gamma - \beta h. \tag{A.69}$$

We know that in the steady-streaming regime without drainage, $\tau_b > 0$. From equations A.68 and A.69 we can say

$$h > 1 \tag{A.70}$$

$$h < \frac{\gamma}{\beta}. \tag{A.71}$$

Ultimately, we find a condition for the steady-streaming regime without drainage

$$\gamma > \beta. \tag{A.72}$$

When this condition is violated, we are in the steady-streaming with drainage regime that results in $\tau_b \to 0$, a zero-strength bed.

A.5 Approximating steady-streaming velocity without drainage

We need to solve for the fixed point of u in the case that $\tau_b > 0$ in order to determine the steady streaming velocity in the case without drainage. We start by combining equations A.68 and A.69 to get

$$h^2 + \beta h - \gamma - h^{1-\frac{1}{n}} = 0. \tag{A.73}$$

This is a quadratic equation in h with an extra term. Equation (A.65) gives us $u = h^{-1}$, so all we need in order to solve for u is an expression for h.

Our approach here is to solve equation (A.73) using a perturbation method. For an overview of this approach see Bender and Orszag (1978). This follows from the observation that if we replace the last term in equation (A.73) with $h^{1+\text{eps}}$ where $\varepsilon = -\frac{1}{n}$, then we can find an exact solution in the limit that $\varepsilon \to 0$. That is, the solution of

$$h^2 + \beta h - \gamma - h = 0, \tag{A.74}$$

is

$$h_0 = \frac{1}{2}(1 - \beta) + \frac{1}{2}\sqrt{(\beta - 1)^2 + 4\gamma}. \tag{A.75}$$

We can now find corrections to this zero-order approximation by assuming that equation (A.73) has the following solution

$$h(\varepsilon) = h_0 + a_1\varepsilon + a_2\varepsilon^2 + \dots \tag{A.76}$$

Retaining just the $O(\varepsilon^2)$ terms

$$h(\varepsilon) \approx h_0 + a_1\varepsilon + a_2\varepsilon^2, \tag{A.77}$$

we insert this expression into equation (A.73), collecting terms in orders of ε

$$h_0^2 + \beta h_0 - \gamma + (2h_0a_1 + \beta a_1)\,\varepsilon + (2h_0a_2 + a_1^2 + \beta a_2)\,\varepsilon^2 - (h_0 + a_1\varepsilon + a_2\varepsilon^2)^{(1+\text{eps})} = 0. \tag{A.78}$$

The last term on the LHS of this equation requires more care in expansion. We first expand the

generic expression h^{1+eps} with a Taylor series retaining only $O(\varepsilon^2)$ terms

$$h^{1+eps} \approx h + \varepsilon h ln h + \frac{1}{2}\varepsilon^2 h ln^2 h. \tag{A.79}$$

Inserting equation (A.77) above, collecting terms in ε and neglecting higher order terms, we have

$$h^{1+eps} \approx h_0 + (a_1 + h_0 ln h_0)\,\varepsilon + \left(a_2 + a_1 ln h_0 + a_1 + \frac{1}{2} h_0 ln^2 h_0\right)\varepsilon^2. \tag{A.80}$$

Combining this back with equation (A.78)

$$\begin{aligned}&[h_0^2 + (\beta - 1)\,h_0 - \gamma] + (2h_0 a_1 + \beta a_1 - a_1 - h_0 ln h_0)\,\varepsilon + \\ &(2h_0 a_2 + a_1^2 + \beta a_2)\,\varepsilon^2 + h_0 + (a_1 + h_0 ln h_0)\,\varepsilon + \left(a_2 + a_1 ln h_0 + a_1 + \frac{1}{2} h_0 ln^2 h_0\right)\varepsilon^2 = 0.\end{aligned} \tag{A.81}$$

The first bracketed term on the LHS here is exactly zero, from equation (A.74). Thus, we can now set each of the ε coefficients to zero and solve for a_1 and a_2

$$a_1 = \frac{h_0 ln h_0}{2h_0 + \beta - 1} \tag{A.82}$$

$$a_2 = \frac{a_1\,(ln h_0 + 1 - a_1) + \frac{1}{2} h_0 ln^2 h_0}{2h_0 + \beta - 1} \tag{A.83}$$

Together with equations (A.75) and (A.77), keeping in mind that $\varepsilon = -\frac{1}{n}$ and $u = h^{-1}$ this gives us zero, first and second order approximations on the non-dimensional equilibrium sliding velocity for steady-streaming without drainage (accurate, respectively to 5%, 1% and 0.1% of numerically determined values). The zero-order approximation is reproduced in the text.

A.6 Asymptotics of small α relaxation oscillations

Below, we sketch the leading order structure of the solution to our ice stream model in more detail for the case of a rapidly-adjusting bed water content (small α). This allows us to show that oscillatory solutions consists of two distinct phases, one in which the ice stream is stagnant and thickening, and another in which the ice stream is active and thinning, with velocity computable simply as a function of ice thickness on both. This is analogous to the glacier surge model proposed by Fowler (1987). The details of the relationship between basal shear stress and water content of the bed are then no longer germane to the the structure of the ice thickness oscillation, except during brief transients when the ice stream switches on or off. In fact, even our choice of a Coulomb friction law rather than a power law to relate τ_b to velocity and bed water content is largely irrelevant. These simplifications also allows us to derive some simplified formulas for oscillation period and amplitude in some parametric limits.

We neglect drainage and basal cooling, treat the heat capacity of basal ice as negligible, take β, γ, τ_0 and c as $O(1)$ constants, and treat α as small. The reduced model is then given by equations (A.15)-(A.22).

A.6.1 Stagnant and active branches

With $\alpha \ll 1$, equation (A.16) will be reduced to its steady-state version except during brief transients. There are two such steady states, corresponding to a stagnant and an active ice stream, respec-

tively. For a stagnant ice stream,

$$u = 0 \tag{A.84a}$$

$$\tau_b < h^2 \tag{A.84b}$$

$$h < \gamma/\beta \tag{A.84c}$$

in which case equation (A.15) becomes

$$\dot{h} = 1 \tag{A.84d}$$

so h increases linearly with time. We call this the zero-velocity or stagnant branch.

The other case is the active ice stream with $u > 0$ so $h^2 > \tau_b > 0$, In this case $h^2 - \tau_b = hu^{1/n}$ so $\tau_b = h^2 - hu^{1/n}$. Substituting for τ_b in equation (A.16) yields, at leading order in α

$$(h^2 - hu^{1/n})u = \gamma/h - \beta, . \tag{A.85}$$

Note that the friction law, equation (A.17), was not involved at all in this calculation, so the fact that τ_b is independent of u (which is one of the defining characteristics of a Coulomb friction law) is irrelevant to the behaviour of u for the active ice stream. In particular, equation (A.85) defines $u = U(h)$ implicitly as a function of h for some range of h. Note that $\tau_b = h^2 - hu^{1/n} \geq 0$ and so we require $h \leq \gamma/\beta$. We will show next that there is also a lower bound h_c on h for a solution to equation (A.85) to exist. This is the ice thickness attained at surge termination.

In equation (A.85), the left-hand side has a global maximum with respect to u at $u = (n/(n+1))^n h^n$, where the left-hand side attains a value of $(n^n/(n+1)^{n+1})h^{n+2}$. In order for equation (A.85) to have a solution, this must be greater than $\gamma/h - \beta$. In other words, we must have

$$\frac{n^n}{(n+1)^{n+1}} h^{n+3} + \beta h \geq \gamma, \tag{A.86}$$

which defines the critical value h_c by turning the weak inequality sign into an equality. There is a single, non-zero solution $u_c = U(h_c) = (n/(n+1))^n h_c^n$ to equation (A.85) at $h = h_c$.

The left-hand side of equation (A.85) is a concave function (with negative second derivative) for $u > 0$, and is positive for $0 < u < h^n$, attaining 0 at the end points of that interval. Therefore, in general, there will be either two values of u in $(0, h^n)$ that satisfy equation (A.85), or none at all. It is straightforward to show that, in order to ensure stability on the fast α^{-1} time scale for changes in w, we must choose the larger of the two solutions where solutions exist, and that this solution also satisfies $\mathrm{d}U/\mathrm{d}h > 0$.

Note that from equation (A.17), we also require $h^2 - hu^{1/n} = \tau_b < \tau_0$. It is therefore possible that the non-zero steady state velocity $U(h)$ will cease to exist at values $h > h_c$, namely if $\tau_0 u_c < \gamma/h_c - \beta$. Physically, this would correspond to an inability to generate sufficient friction to keep dissipation rates high enough to balance conductive heat loss. For simplicity, we ignore this possibility below, assuming that τ_0 is large enough for this possiblity not to become an issue.

Given $u = U(h)$, h then evolves according to

$$\dot{h} = 1 - hU(h) \tag{A.87}$$

on this solution branch, which we call the surge or active branch of the solution. Repeated oscillations can only occur if this evolution equation does not have a stable steady-state solution. This requires that we have $hU(h) > 1$ for all thicknesses that admit a non-zero velocity solution $U(h)$. since U increases with h, this is tantamount to $h_c U(h_c) > 0$.

The two evolution equations (A.84) and (A.87) combined with the requirement that $h > h_c$ on the active branch and $h < \gamma/\beta$ on the stagnant branch are sufficient to describe the overall dynamics predicted in our model. We exploit this in the next section to show how in certain limits of β and γ, we are able to give estimates of the oscillation amplitude and period, or able to predict that no

oscillations will occur. We then still need to show that rapid transitions can indeed occur between the two branches as envisaged, which we defer to the end of our discussion as the relevant analysis is a great deal more complicated than the material that follows immediately below.

Before we proceed, we note that the structure of the solution we are constructing is that of a standard relaxation oscillation such as that produced by the van der Pol osillator (Hinch, 1991). In both cases, the solution remains on the nullcline for the rapidly evolving variable during most of the limit cycle except for the rapid transition phases we are about to describe below. In the present case, this rapidly evolving variable is w. The primary difference between our oscillator and the canonical van der Pol oscillator is that our variable w satisfies an evolution equation that is non-smooth, as $\dot{w}$ changes discontinuously when w reaches zero from above (in which case $\tau_b u + \beta - \gamma/h > 0$).

A.6.2 The stagnant and active branches in parametric limits of β and γ

Next, we show that if β and γ are large or small (but not so much as to invalidate the asymptotic structure developed for small α above), we can draw several conclusions about the resulting surge cycle (or indeed, whether surges occur at all) from the behaviour of the active and stagnant branches in those parametric limits. We work through several of these limits in turn. For the case of β, $\gamma = O(1)$, no such results are possible analytically, as the active branch solution cannot be found analytically.

Our arguments below are built around four observations. First, transitions from stagnant to active occur at at $h = \gamma/\beta$. Second, the reverse transition occurs at some value $h = h_c$ at which equation (A.86) holds with equality. Third, a solution to equation (A.85) that corresponds to $\tau_b > 0$ must have $h < \gamma/\beta$. Hence solutions on the stagnant branch have $h < \gamma/\beta$, while solutions on the active branch have $h_c < h < \gamma/\beta$. Fourth, in order for oscillations to occur, we must also have $hU(h) > 1$, or a stable steady state can form on the active branch.

$\gamma \sim \beta \ll 1$

When $\gamma \sim \beta \ll 1$, the transition from stagnant to active occurs at an $O(1)$ value γ/β. However, the active branch exists down to small values of h; from equation (A.86), we see that $h_c = O(\gamma^{1/(n+3)})$, and correspondingly, $u_c = O(\gamma^{n/(n+3)})$. But this implies that $u_c h_c = O(\gamma^{(n+1)/(n+3)}$, and hence $u_c h_c < 1$. A stable solution therefore exists on the active branch, corresponding to steady ice stream flow.

$\gamma = O(1), \beta \ll 1$

The stagnant to active transition now occurs at a large ($O(\beta^{-1})$) thickness γ/β, while from equation (A.86) we estimate that $h_c = O(1)$, and correspondingly $u_c = O(1)$. In this parameter regime, it is therefore possible that $u_c h_c < 1$ and that there is a stable on the active branch, but equally, there may not be. In the latter case, there will be oscillations, and we can find leading order expressions for their amplitude and period.

Both are dominated by the stagnant phase. First, the ampltidue of the oscillation is $\gamma/\beta - h_c \sim \gamma/\beta(1 - O(\beta))$ at leading order. Meanwhile equation (A.84) shows that, to build ice to a thickness γ/β from an initial thickness $h_c = O(1)$ takes a length of time $\sim \gamma/\beta(1 + O(\beta))$. By contrast, the surge phase has a much shorter duration. Initially, thickness h in the surge phase is $O(\beta^{-1})$, and correspondingly $u \sim h^n = O(\beta^{-n})$. The time scale for thinning early in the surge phase scales as $u^{-1} \sim \beta^n$. Subsequently, near the transition from active to stagnant, we have u and h of $O(1)$, corresponding to an $O(1)$ time scale. Both of these are much smaller than the length of time γ/β required at leading order for the stagnant phase, which therefore gives the leading order estimate for the period of oscillation as γ/β.

$\gamma \ll 1, \beta = O(1)$

Here, the transition from stagnant to fast occurs at a small thickness $h = \gamma/\beta = O(\gamma)$, corresponding to a small velocity $u = (\gamma^n)$. The velocity after transition to the active branch is therefore too *small*, and the ice stream will actually thicken rather than thin. This falls outside the remit of the asymptotic model we have formulated above. To allow hu to increase beyond γ/β is possible if, instead of insisting on equation (A.85) as the steady state version of equation (A.16), we allow $w \to \infty$. In that case, $\tau_b \sim 0$ from equation (A.17) and at leading order $u = h^n$ from equation (A.19). A steady state for h will then be attained when $uh = h^{n+1} = 1$, so $h = 1$, with w going to infinity. Allowing drainage in the model would potentially alleviate w growing without bound.

$\gamma \gg 1, \beta = O(1)$

The transition from stagnant to active occurs at a large $h = \gamma/\beta = O(\gamma)$. From equation (A.86), we have $h_c = O(\gamma^{1/(3+n)})$ with $u_c = O(\gamma^{n/(3+n)})$. Hence $h_c u_c$ is large and oscillations are bound to occur. We can again find leading order expressions for amplitude and period, as we did for the case $\gamma = O(1), \beta \ll 1$.

Specifically, the stagnant phase dominates again, h has to increase from $h_c = O(\gamma^{1/(n+3)})$ to γ/β, which at leading order takes an amount of time $\gamma/\beta(1 + O(\gamma^{-(n+2)/(n+3)})$, and the amplitude of the oscillation is also $\gamma/\beta - h_c = \gamma/\beta(1 + O(\gamma^{-(n+2)/(n+3)})$. Velocities at the beginning of the surge phase are of $O(\gamma^n)$, so the time scale for initial thinning is $O(\gamma^{-n})$. The transition from active to stagnant occurs when u is reduced to $O(\gamma^{1/(3+n)})$, with associated time scale $O(\gamma^{-1/(n+3)})$, which is still much less than the error in the computation of the length of the stagnant phase above. The entire cycle therefore takes length $\gamma/\beta(1 + O(\gamma^{-(n+2)/(n+3)})$.

$\gamma = O(1), \beta \gg 1$

As in the case $\gamma \ll 1, \beta = O(1)$, the transition from stagnant to active occurs at a small thickness $\gamma/\beta = O(\beta^{-1})$, and as in that previous case, we again expect a solution that settles into a steady state $h = 1$ for h, with w diverging to infinity.

$\gamma \sim \beta \gg 1$

The transition from stagnant to active now happens at an $O(1)$ value γ/β, corresponding to an $O(1)$ velocity. However, the range between h_c and γ/β is now very narrow: from equation (A.86), we can see that $h_c \sim \gamma/\beta + \beta^{-1} n^n/(n+1)^{n+1}(\gamma/\beta)^{n+3}$. There are three possiblities: either $hU(h) < 1$ at $h = \gamma/\beta$, and we have a situation analogous to the case $\gamma = O(1), \beta \gg 1$ above, with h settling to a steady state at unity and w growing without bound. Alternatively, there could be an value of h between h_c and γ/β such that $hU(h) = 1$, with the ice stream settling into a steady state there. However, given that h_c is close to γ/β, this is an unlikely outcome. Lastly, it is possible that $h_c U(h_c) > 1$ and the ice stream will undergo oscillations. This will have very small amplitude $\gamma/\beta - h_c \sim \beta^{-1}$, with a period that also scales as β^{-1}.

A.6.3 Transitions between stagnant and active branches

Next, we look again at the case of oscillations, and complete the asymptotic analysis of limit cycle solutions by describing the leading order structure of the transitions between stagnant and active branches.

Transition from stagnant to active

At the time when h reaches γ/β, w will have attained 0 as $\beta < \gamma/h$ during the stagnant phase and, with $u = 0$, only the second case in equation (A.16) can be attained on setting the left-hand side to

zero.

Suppose for simplicity that $\tau_0 > (\gamma/\beta)^2$. Physically, this means that the strength of the bed at the critical void ratio e_c is large enough to prevent sliding from recommencing at the critical thickness $h = \gamma/\beta$ at which melting begins. To reactivate sliding with h close to γ/β then requires a finite ($O(1)$) amount of melt to be generated first, so that τ_b drops to the critical value $(\gamma/\beta)^2$ at which sliding recommences. Label the finite amount of melt required to attain $\tau_b = \tau_0 \exp(-c(w-e_c)) = (\gamma/\beta)^2$ by $w_s = e_c + c^{-1}\log[(\gamma/\beta)^2/\tau_0]$. This finite amount of melt is generated by h rising slightly above γ/β, reducing conductive loss sufficiently to allow melt to take place.

Let $t = t_s$ be the time at which $h = \gamma/\beta$ is attained. Then define a fast time scale for this initial melt process as $T_1 = \alpha^{-1/2}(t - t_s)$, and let $h = \gamma/\beta + \alpha^{1/2}h_1$. With these rescalings, at leading order

$$\frac{\mathrm{d}h_1}{\mathrm{d}T_1} = 1, \qquad \frac{\mathrm{d}w}{\mathrm{d}T_1} = \frac{\beta^2}{\gamma}h_1.$$

Clearly h_1 and therefore w increase linearly with T_1. Eventually w_s is attained at a finite $T_1 = T_s = \gamma w_s/\beta^2$.

Sliding recommences at $T_1 = T_s$. There is an initial interval over which both frictional dissipation and conductive heating play similar roles, as velocity starts from zero so there is at first no dissipation. This is analogous to the corner layer of the van der Pol oscillator solution (Hinch, 1991). In this initial sliding stage, we can rescale as $w = w_s + \alpha^{1/2n}W_2$, $T_2 = \alpha^{-1+(n-1)/2n}(t - t_s - \alpha^{1/2}T_s)$, $h = \gamma/\beta + \alpha^{1/2}T_s + O(\alpha^{-1-(n-1)/2n})$. equation (A.16) becomes at leading order

$$\frac{\mathrm{d}W_2}{\mathrm{d}T_2} = \left(\frac{\gamma}{\beta}\right)^{n+1} c^n W_2^n + \left(\frac{\beta^2}{\gamma}\right) h_1.$$

This solution to this equation initially grows linearly due to the second (conductive heating) term on the right hand side, but eventually the first (dissipation) term on the right-hand side becomes

dominant. With $n > 1$, this eventually leads to finite-time blow-up at some $T_2 = T_b$, with W_2 behaving as

$$W_2 \sim \frac{\beta^{(n+1)/(n-1)}}{\gamma^{(n+1)/(n-1)} c^{n/(n-1)} [(n-1)(T_b - T_2)]^{1/(n-1)}} \tag{A.88}$$

This blow-up of course in reality corresponds to the main transition from the zero-velocity branch to the surge branch, during which w becomes much larger than w_s.

To capture this requires a further rescaling to the fast time scale α. for which we put $T_3 = \alpha^{-1}(t - t_s - \alpha^{1/2} T_s - \alpha^{-1+(n-1)/2n} T_b)$, $W_3 = w$, $U_3 = u$, $h = \gamma/\beta + \alpha^{1/2}$. With this rescaling, we get at leading order that $\tau_b = h^2 - hU^{n/n} = (\gamma/\beta)^2 - (\gamma/\beta) U^{n/n}$ and $\beta - \gamma/h = 0$ so that equation (A.16) becomes

$$\frac{\mathrm{d}W_3}{\mathrm{d}T} = [(\gamma/\beta)^2 - (\gamma/\beta) U^{n/n}] U, \tag{A.89}$$

with W_3 and U linked through equations (A.17) and (A.19) by $U = (\gamma/\beta)[1 - \exp(c(w_s - W))]^n$. U is therefore an increasing function of W, and the fixed point $U = 0$, $W = w_s$ is unstable. Matching with the corner layer solution through equation (A.88) leads to an initial condition

$$W_3 \sim \frac{\beta^{(n+1)/(n-1)}}{\gamma^{(n+1)/(n-1)} c^{n/(n-1)} [-(n-1) T_3]^{1/(n-1)}} \tag{A.90}$$

as $T_3 \to -\infty$ that describes the initial evolution away from the fixed point. The large T_3 solution is given by $U = (\gamma/\beta)^n$; this is the solution obtained from equation (A.19) by setting $\tau_b = 0$, and actually corresponds to $W_3 \to \infty$. $u = U = (\gamma/\beta)^n$ is also the larger of the two solutions to equation (A.85) when $h = \gamma/\beta$, and the large T_3 behavior therefore corresponds to $h \sim \gamma/\beta$, $U \sim U(h)$ as expected in order to match with the surge branch.

Transition from active to stagnant

The reverse transition from a surging to a non-surging ice stream occurs when h computed through equation (A.87) on the surge branch reaches the critical value h_c below which equation (A.85) has no solution. This transition is harder to describe as we cannot compute h_c analytically. However, generically we can write equation (A.85) in the form

$$F(u, h) = (h^2 - hu^{1/n})u + \gamma/h - \beta = 0,$$

and the critical thickness h_c corresponds to a saddle-node bifurcation point (h_c, u_c) at which

$$F(u_c, h_c) = 0, \qquad \frac{\partial F}{\partial u}(u_c, h_c) = 0. \tag{A.91}$$

With $u > 0$, the evolution equation equation (A.16) can also be written as

$$\alpha \frac{\mathrm{d}w}{\mathrm{d}t} = F(u, h), \tag{A.92}$$

with $w = e_c - c^{-1} \log[(h^2 - hu^{1/n})/\tau_0]$, so that $\mathrm{d}w/\mathrm{d}u > 0$.

Define

$$F_{uu} = \frac{\partial^2 F}{\partial u^2}(u_c, h_c), \qquad F_h = \frac{\partial F}{\partial h}(u_c, h_c), \qquad w_u = \frac{\mathrm{d}w}{\mathrm{d}u}(u_c, w_c).$$

We have $F_{uu} < 0$ while $F_h > 0$ and $u_w > 0$.

Let t_c be the time at which h computed from equation (A.87) reaches h_c. First, we need to describe the onset of shutdown, when the increase in conductive heating due to ongoing thinning contributes equally to reduction in bed water content as does the reduction in dissipative heating as u 'falls off' the surge branch. This is again analogous to the corner layer in the van der Pol oscillator.

Rescale as

$$T_4 = \alpha^{-2/3}(t - t_c), \qquad (u - u_c) = \alpha^{1/3} U_4, \qquad h - h_c = \alpha^{2/3} H_4. \tag{A.93}$$

By Taylor expanding around (u_c, h_c), we can then show that the leading order form of equation (A.92) is now

$$w_u \frac{\mathrm{d}U_4}{\mathrm{d}T_4} = \frac{1}{2} F_{uu} U_4^2 + F_h H_4 \tag{A.94a}$$

$$\frac{\mathrm{d}H_4}{\mathrm{d}T} = 1 - u_c h_c. \tag{A.94b}$$

By assumption, we have $u_c h_c > 1$, so H_4 decreases linearly with time. As a matching condition with the surge branch computed from equations (A.85) and (A.87), we have $H_4 \sim (1 - u_c h_c) T_4$ as $T_4 \to -\infty$, and this therefore remains the solution for H_4 in time throughout the corner layer. We also have the matching condition

$$U_4 \sim \left[-\frac{2F_h}{F_{uu}} \right]^{1/2} H_4^{1/2}$$

as $T_4 \to -\infty$. When T_4 and hence H_4 is positive, U_4 will grow increasingly negative, initially due to the second term in equation (A.97) and later due to the first, quadratic term that once again leads to finite time blow-up at some time T_t, with U_4 behaving as

$$U_4 \sim \frac{F_{uu}}{2w_u(T_t - T_4)}. \tag{A.95}$$

Once more, finite time blow-up actually corresponds to a rapid transition, this time to the zero velocity branch. This is captured by the rescaling

$$T_s = \alpha^{-1}(t - t_c - \alpha^{2/3} T_t), \qquad W_s = w, \qquad h = h_c + O(\alpha^{2/3}), \tag{A.96}$$

which leads to the equivalent of equation (A.89), at leading order

$$\frac{\mathrm{d}W_s}{\mathrm{d}T_s} = [h_c^2 - h_c U^{1/n}]U + \gamma/h_c - \beta \tag{A.97}$$

now with $W_s = e_c - c^{-1}\log[(h_c^2 - h_c U^{1/n})/\tau_0]$, so W_s is again an increasing function of U. Matching with the solution of equation (A.94a) gives $U_s \sim u_c - F_{uu}/(2w_u T_s)$ as $T_s \to -\infty$. With $U < u_c$, the right-hand side of equation (A.97) will be negative (recall that it is zero when $U = u_c$). Hence W_s will decrease, as will U. U reaches zero in finite time, completing the transition to the zero-velocity branch at $h = h_c$. This completes the limit cycle solution.

A.7 Approximating binge-purge period and critical thicknesses for realistic $\alpha = O(10^{-1})$

A.7.1 Critical stagnation thickness

Equation (A.86) gives us the exact location of the critical stagnation thickness on the active branch (for small α, though this applies equally well here). Here we rearrange and place a term ε on the linear term (perturbation expansions in other terms either fail or yield worse asymptotic approximation on h_s)

$$\eta h_s^{n+3} + \varepsilon\beta h_s - \gamma = 0 \tag{A.98}$$

with $\eta = \frac{n^n}{(n+1)^{n+1}}$.

As above, in section 5, use a perturbation method. (For an overview of this approach see Bender and Orszag (1978).) We solve the $\varepsilon = 0$, zero-order approximation first

$$\eta h_0^{n+3} - \gamma = 0 \tag{A.99}$$

$$\eta h_0 = \left(\frac{\gamma}{\eta}\right)^{\frac{1}{n+3}}. \tag{A.100}$$

We can now find corrections to this zero-order approximation by assuming that equation (A.86) has the following solution

$$h_s(\varepsilon) = h_0 + a_1\varepsilon + a_2\varepsilon^2 + \dots \tag{A.101}$$

Retaining just the $O(\varepsilon^2)$ terms

$$h_s(\varepsilon) \approx h_0 + a_1\varepsilon + a_2\varepsilon^2, \tag{A.102}$$

We substitute this into equation equation (A.98)

$$\eta\left(h_0 + a_1\varepsilon + a_2\varepsilon^2\right)^{n+3} + \varepsilon\beta\left(h_0 + a_1\varepsilon + a_2\varepsilon^2\right) - \gamma = 0, \tag{A.103}$$

expanding and only retaining terms in $O(\varepsilon^2)$

$$\left[\eta h_0^{n+3} - \gamma\right] + (n+3)a_1\eta h_0^{n+2}\varepsilon + (n+3)a_2\eta h_0^{n+2}\varepsilon^2 + \binom{n+3}{2} a_1^2 h_0^{n+1}\varepsilon^2 + \varepsilon\beta h_0 + \beta a_1\varepsilon^2 = 0. \tag{A.104}$$

The first bracketed term on the LHS is exactly the solution of the zero-order approximation. Otherwise, we collect terms in ε^1 and solve for a_1

$$\left[(n+3)a_1\eta h_0^{n+2} + \beta h_0\right]\varepsilon = 0 \tag{A.105}$$

Substituting in h_0 and collecting terms in the relevant parameters yields

$$a_1 = -\frac{\beta}{n+3}\left(\eta^2\gamma^{n+1}\right)^{-\frac{1}{n+3}} \tag{A.106}$$

Similarly, we collect terms in ε^2 and solve for a_2

$$\left[(n+3)a_2\eta h_o^{n+2} + \binom{n+3}{2} a_1^2 h_o^{n+1}\varepsilon^2 + \beta a_1\right]\varepsilon^2 = 0 \tag{A.107}$$

Substituting in h_o and a_1, we collecting terms in the relevant parameters and solve for a_2

$$a_2 = -\frac{n}{2(n+3)^2}\beta^2\left(\eta^3\gamma^{2n+3}\right)^{-\frac{1}{n+3}} \tag{A.108}$$

With these three terms in hand, we take $\varepsilon \to 1$ and construct an approximation for (non-dimensional) h_s:

$$h_s = \left(\frac{\gamma}{\eta}\right)^{\frac{1}{n+3}} - \frac{\beta}{n+3}\left(\eta^2\gamma^{n+1}\right)^{-\frac{1}{n+3}} - \frac{n}{2\left(n+3\right)^2}\beta^2\left(\eta^3\gamma^{2n+3}\right)^{-\frac{1}{n+3}} \tag{A.109}$$

A.7.2 Stagnation period

When the ice stream falls off the active branch at h_s and onto the stagnant branch, the dynamics of the ice stream model become considerably simpler (as $u* = 0$). Notably, we have the following evolution of the till water content:

$$\alpha\frac{dw}{dt} = \beta - \frac{\gamma}{h}, \tag{A.110}$$

and a linear evolution in ice thickness:

$$h(t) = h_s + t, \tag{A.111}$$

(assuming that there is not any considerable change in h^* during the transition from the active to stagnant branch). We see that we can solve exactly for the evolution in till water content:

$$\alpha \frac{dw}{dt} = \beta - \frac{\gamma}{h_s + t} \tag{A.112}$$

$$w(t) = \frac{\beta}{\alpha}(h_s + t) - \frac{\gamma}{\alpha} \ln(h_s + t) + w_0 \tag{A.113}$$

Or rather, in reference to a time Δt since stagnation:

$$w(\Delta t) = \frac{\beta}{\alpha} \Delta t - \frac{\gamma}{\alpha} \ln\left(1 + \frac{\Delta t}{h_s}\right) \tag{A.114}$$

A quick estimate of period

To derive a quick estimate on the period (which we will use later to derive a more accurate estimate) we note that the change in driving stress, h^2, during the stagnant phase is relatively small in comparison to the change in basal shear strength. Thus, we attempt to find Δt by looking for the roots of equation (A.114). Also, we note that the trajectory of till water content is almost symmetric with a minimum value attained when $h = \frac{\gamma}{\beta}$. Thus, we can approximate equation (A.114) as the quadratic

$$w(\Delta t) = \Delta t^2 - 2\left(\frac{\gamma}{\beta} - h_s\right) \Delta t \tag{A.115}$$

This equation readily admits two roots, the first being $\Delta t = 0$ and the second being:

$$\Delta t = 2\left(\frac{\gamma}{\beta} - h_s\right) \tag{A.116}$$

Long way around

We now attempt to solve for the time since stagnation, Δt, at which the bed fails critically, which should occur when

$$h^2 = \tau_b, \tag{A.117}$$

or in terms of our time evolution for till water content and a linearly accumulating ice stream thickness:

$$(h_s + \Delta t)^2 = h_s^2 \exp\left(-b\left[\frac{\beta}{\alpha}\Delta t - \frac{\gamma}{\alpha}\ln\left(1 + \frac{\Delta t}{h_s}\right)\right]\right) \tag{A.118}$$

Rearranging and applying various log rules:

$$\Delta t - \left(\frac{\gamma}{\beta} - \frac{2\alpha}{b\beta}\right)\ln\left(1 + \frac{\Delta t}{h_s}\right) = 0 \tag{A.119}$$

Expanding in the first term of log about our earlier estimate of period, $\Delta t = 2\left(\frac{\gamma}{\beta} - h_s\right)$, we have

$$\Delta t - \left(\frac{\gamma}{\beta} - \frac{2\alpha}{b\beta}\right)\left[\ln\left(2\frac{\gamma}{\beta h_s} - 1\right) + \frac{\Delta t - 2\left(\frac{\gamma}{\beta} - h_s\right)}{2\frac{\gamma}{\beta} - h_s} + O(h^2)\right] = 0 \tag{A.120}$$

And then solving for Δt, we get

$$\Delta t = \frac{\gamma - \frac{2\alpha}{b}}{\beta - \frac{1}{2\frac{\gamma}{\beta} - h_s}\left(\gamma - \frac{2\alpha}{b}\right)}\left[\ln\left(2\frac{\gamma}{\beta h_s} - 1\right) - \frac{\frac{\gamma}{\beta} - h_s}{\frac{\gamma}{\beta} - \frac{h_s}{2}}\right] \tag{A.121}$$

For γ that is $O(1)$ it is the case that $\frac{2\alpha}{b} << \gamma$ unless the till layer is $O(10)$. This corresponds to a situation where the change in driving stress during stagnation is small compared to the change in

bed strength, a valid assumption for all but the strongest binge-purge oscillations (for which this entire derivation does not apply anyway). The following simplification can be made:

$$\Delta t = \frac{\gamma}{\beta - \dfrac{\gamma}{2\dfrac{\gamma}{\beta} - h_s}} \left[\ln\left(2\frac{\gamma}{\beta h_s} - 1 \right) - \frac{\dfrac{\gamma}{\beta} - h_s}{\dfrac{\gamma}{\beta} - \dfrac{h_s}{2}} \right] \tag{A.122}$$

This provides a good estimate on the period of binge-purge oscillations. In this approximation, we have neglected the purge phase, which only contributes significantly to the period near the stability boundary. Also, in the reduced model we are not taking into account any till-freezing or basal cooling, thus these approximations becomes increasingly poor for large REHF (in the strong binge-purge regime). However, this approximation is still within 10% of numerically derived period estimates in the weak binge-purge parameter regime away from the stability boundary.

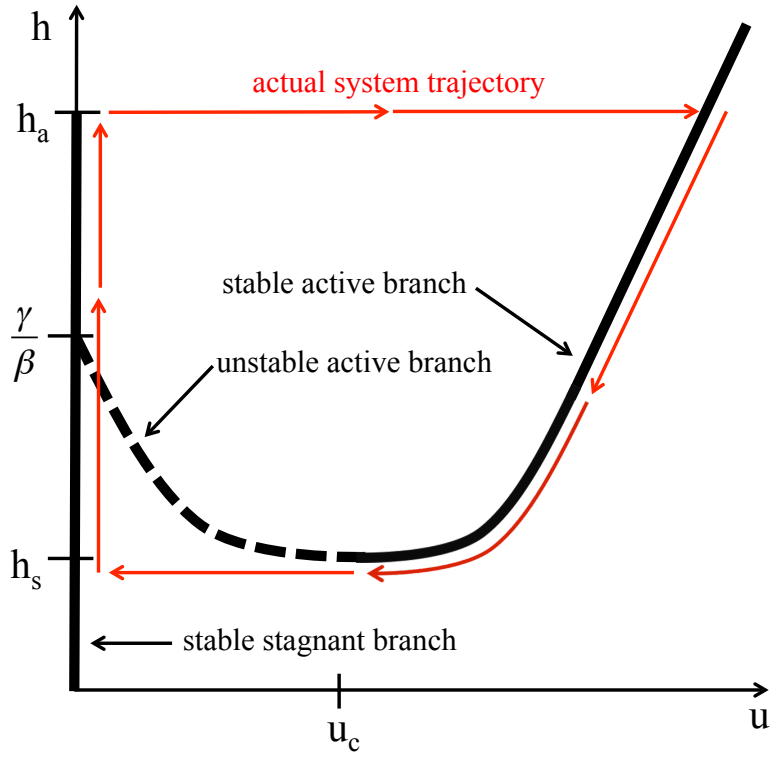

Figure A.1: Phase portrait of the reduced model.

B

Appendix B (Chapter 3)

B.1 Model Details

B.1.1 Stretch Coordinates

One of the primary purposes of this model is to accurately capture the grounding line position as the ice stream evolves. Our approach here is based off of that of Schoof (2007a). We adopt a system

of dimensionless stretch coordinates in the $x - z$ plane

$$\sigma = \frac{x}{x_g} \tag{B.1}$$

$$\eta = \frac{z - b}{h}, \tag{B.2}$$

where x_g is the grounding line position, b is the bedrock elevation and h is the ice stream thickness. In this system, the grounding line is always at $\sigma = 1$ and the ice surface is always at $\eta = 1$.

B.1.2 Horizontal Velocity

We start by considering the x-directed momentum balance for an ice stream

$$\partial_x \left(2hA^{-\frac{1}{n}} \left|\partial_x u_b\right|^{\frac{1}{n}-1} \partial_x u_b \right) = \tau_d(x,t) + \tau_b(x,t) + G_s h |u_b|^{\frac{1}{n}-1} u_b, \tag{B.3}$$

where $u_b(x,t) = u(z = b; x, t)$ is the basal ice velocity. The term on the LHS is the longitudinal stress and the three terms on the RHS are (respectively) the driving stress, basal shear stress and cross-stream integrated lateral shear stress. The basal velocity u_b is assumed to result from till deformation. A is the vertically integrated Glen's law coefficient which is a function of ice temperature and n is the Glen's law exponent.

Driving stress has its usual form

$$\tau_d(x,t) = \varrho_i g h \partial_x h, \tag{B.4}$$

where ϱ_i is the density of glacial ice and g is the acceleration due to gravity.

As in Dupont and Alley (2005), the parameter G_s arises from assuming that cross-stream variation in velocity primarily occurs in the shear margins and then scaling away the parameters that arise

in this margin, yielding

$$G_s = W^{-1}(A_s W_s)^{-\frac{1}{n}} \tag{B.5}$$

where A_s is the Nye-Glen Law coefficient in shear margins, W is the ice stream half-width and W_s is the shear margin width.

Vertical shear of horizontal velocity is calculated separately by following the shallow ice approximation and assuming simple shear

$$u(\eta) = u_b + \frac{2A}{n+1}\tau_d^n H\left[1 - (1-\eta)^{n+1}\right]. \tag{B.6}$$

where η is the scaled vertical coordinate, u_b is the basal velocity calculated using the momentum balance from above and A is the vertically averaged Glen's law coefficient.

B.1.3 Vertical Velocity

We expect that our model may develop large gradients in horizontal velocity as horizontal variations in till water content lead to large variations in bed strength (see section B.1.6). Without enforcing mass continuity, these local divergences will lead to significant losses of heat from the ice in locations where the heat balance is critical. Thus, we enforce x-z mass continuity

$$\partial_x u + \partial_z w = 0. \tag{B.7}$$

Adopting stretch coordinates, this becomes

$$\frac{1}{x_g}\frac{\partial u}{\partial \sigma} - \frac{\left(\eta\dfrac{\partial h}{\partial \sigma} + \dfrac{\partial b}{\partial \sigma}\right)\dfrac{\partial u}{\partial \eta}}{h x_g} + \frac{\dfrac{\partial w}{\partial \eta}}{h} = 0, \tag{B.8}$$

subject to $w + u\frac{\partial b}{\partial x} = 0$ at $z = b$, now $w = \frac{u}{x_g}\frac{\partial b}{\partial \sigma}$ at $\eta = 0$. For constant σ, we choose to integrate from the bed upwards to solve for $w(\eta)$ as a function of $u(\eta)$ (pre-computed above)

$$w(x, z, t) = \int_0^1 \left[\frac{\left(\eta \frac{\partial h}{\partial \sigma} + \frac{\partial b}{\partial \sigma}\right) \frac{\partial u}{\partial \eta}}{h x_g} - \frac{\frac{\partial u}{\partial \sigma}}{x_g} \right] d\eta, \tag{B.9}$$

evaluated at $\sigma = \sigma_0$.

B.1.4 Ice Thickness

Ice thickness evolution is the result of a simple mass balance with constant accumulation as a source everywhere and an advective flux moving ice within and out of the domain. The resulting prognostic equation for ice thickness is simply

$$\dot{h} + \partial_x \left(\bar{u} h\right) = a_c \tag{B.10}$$

where $\bar{u}(x, t) = \frac{1}{h}\int_b^{b+h} u(x, z, t) dz$ is the vertically averaged velocity.

Again, adopting stretch coordinates, the advection equation for ice thickness will change to

$$\dot{h} - \frac{\sigma \dot{x}_g}{x_g} \partial \quad h + \frac{\frac{\partial (\bar{u} h)}{\partial \sigma}}{x_g} = a \tag{B.11}$$

where the extra terms are the result of the changing coordinate system.

We can rewrite this in a more natural divergence form

$$\dot{h} + \frac{1}{x_g} \frac{\partial \left[\left(\bar{u} - \sigma \dot{x}_g\right) h\right]}{\partial \sigma} + \frac{\dot{x}_g}{x_g} h = a \tag{B.12}$$

where $\bar{u} - \sigma \dot{x}_g$ is the "effective" horizontal velocity less the rate of coordinate stretching.

B.1.5 Ice Temperature

Calculating temperature along the flowline and in the vertical is necessary in order to accurately determine the basal heat budget and attendant meltwater production rate. We begin with the advection-diffusion equation for temperature in the x-z plane

$$\dot{T} + \nabla \cdot (\vec{u}T) = \kappa \nabla^2 T \tag{B.13}$$

$$\dot{T} + \partial_x (uT) + \partial_z (wT) = \kappa (\partial_{xx} T + \partial_{zz} T) \tag{B.14}$$

We now transform to the same stretch coordinates as above. In a full expansion, we are left with the following unwieldy heat equation

$$\dot{T} - \frac{\sigma \dot{x}_g}{x_g}\frac{\partial T}{\partial \sigma} - \frac{\eta}{h}\left(\dot{h} - \frac{\sigma \dot{x}_g}{x_g}\frac{\partial h}{\partial \sigma}\right)\frac{\partial T}{\partial \eta} + \frac{1}{x_g}\frac{\partial (uT)}{\partial \sigma} - \frac{1}{h x_g}\left(\eta \frac{\partial h}{\partial \sigma} + \frac{\partial b}{\partial \sigma}\right)\frac{\partial (uT)}{\partial \eta} + \frac{1}{h}\frac{\partial (wT)}{\partial \eta} =$$
$$\kappa \left[\frac{1}{x_g^2}\frac{\partial^2 T}{\partial \sigma^2} + \frac{\eta^2 \left(\frac{\partial h}{\partial \sigma}\right)^2}{h^2 x_g^2}\frac{\partial^2 T}{\partial \eta^2} - \frac{2\eta}{h x_g^2}\frac{\partial h}{\partial \sigma}\frac{\partial^2 T}{\partial \eta \partial \sigma} + \frac{2\eta}{h^2 x_g}\frac{\partial h}{\partial \sigma}\frac{\partial T}{\partial \eta} - \frac{\eta}{h x_g^2}\frac{\partial^2 h}{\partial \sigma^2}\frac{\partial T}{\partial \eta} + \frac{1}{h^2}\frac{\partial^2 T}{\partial \eta^2} \right] \tag{B.15}$$

Then, within the brackets on the RHS, we can perform some scaling, assuming that: $\sigma \sim O(1)$, $\eta \sim O(1)$, $x_g \sim O(10^5)$, $h \sim O(10^3)$. This leaves only the vertical diffusion term, and so our heat equation reduces to

$$\dot{T} - \frac{\sigma \dot{x}_g}{x_g}\frac{\partial T}{\partial \sigma} - \frac{\eta}{h}\left(\dot{h} - \frac{\sigma \dot{x}_g}{x_g}\frac{\partial h}{\partial \sigma}\right)\frac{\partial T}{\partial \eta} + \frac{1}{x_g}\frac{\partial (uT)}{\partial \sigma} - \frac{1}{h x_g}\left(\eta \frac{\partial h}{\partial \sigma} + \frac{\partial b}{\partial \sigma}\right)\frac{\partial (uT)}{\partial \eta} + \frac{1}{h}\frac{\partial (wT)}{\partial \eta} = \frac{\kappa}{h^2}\frac{\partial^2 T}{\partial \eta^2} \tag{B.16}$$

In divergence form this becomes

$$\frac{\partial T}{\partial \tau} + \frac{1}{x_g}\frac{\partial}{\partial \sigma}\left[(u - \sigma \dot{x}_g)T\right] + \frac{1}{h}\frac{\partial}{\partial \eta}\left[\left(w - \eta\left\{\frac{\partial h}{\partial \tau} + \frac{(u - \sigma \dot{x}_g)}{x_g}\frac{\partial h}{\partial \sigma}\right\} - \frac{u}{x_g}\frac{\partial b}{\partial \sigma}\right)T\right] + \frac{\dot{x}_g}{x_g}T + \frac{1}{h}\left[\frac{\partial h}{\partial \tau} + \frac{(u - \sigma \dot{x}_g)}{x_g}\frac{\partial h}{\partial \sigma}\right]T = \frac{k}{h^2}T \quad . \tag{B.17}$$

The advective velocity in the η-direction turns out to be

$$w - \eta\left\{\frac{\partial h}{\partial \tau} + \frac{(u - \sigma \dot{x}_g)}{x_g}\frac{\partial h}{\partial \sigma}\right\} - \frac{u}{x_g}\frac{\partial b}{\partial \sigma}. \tag{B.18}$$

This accounts for the tilting of the element boundaries through the last term as well as for the motion of the element as the domain is stretched.

B.1.6 Till Properties

Since till water content is determined solely by local meltwater production, it is dealt with in a similar way as in chapter 2, which adopts a slightly modified form of the undrained plastic bed model of Tulaczyk et al. (2000b). The basal heat budget is

$$m = \frac{1}{\varrho_i L_f}\left(G + \tau_b(x)u_b(x) + \frac{k_i}{h(x)}\frac{\partial T(x, \eta = 0)}{\partial \eta}\right) \tag{B.19}$$

where, on the RHS, the first term is the geothermal heat flux, the second term is the frictional heat flux and the third term is the conductive heat flux at the bed.

Till void ratio, $e = \frac{Z_w}{Z_s}$, is a ratio of the thickness of void spaces in the till column (Z_w) to unfrozen solid till thickness without void spaces (Z_s). Assuming that meltwater always fills the void spaces in the till column, the till water content can then be defined as $Z_w = eZ_s$. e and Z_s then vary as a function of the ice stream state.

Void ratio is assumed to evolve freely when either above or increasing from a specified lower consolidation threshold, e_c

$$Z_s \frac{\partial e}{\partial t} = \begin{cases} m & \text{if } e > e_c \\ m & \text{if } e = e_c \text{ and } Z_s = Z_o \text{ and } m > 0 \\ 0 & \text{otherwise} \end{cases} \tag{B.20}$$

where Z_o is the maximum available till thickness.

When the void ratio reaches e_c from above, till begins freezing on as a frozen fringe (Rempel, 2007). Z_s, the current thickness of unfrozen till (without void space) can be modeled accordingly

$$e \frac{\partial Z_s}{\partial t} = \begin{cases} m & \text{if } e = e_c \text{ and } 0 < Z_s < Z_o \\ m & \text{if } e = e_c \text{ and } Z_s = Z_o \text{ and } m < 0 \\ 0 & \text{otherwise} \end{cases} \tag{B.21}$$

The basal shear stress is calculated from the basal velocity and void ratio assuming that the till behaves as a Coulomb plastic material

$$\tau_b = \tau_c \frac{u_b}{\sqrt{u_b^2 + \varepsilon_u^2}}, \tag{B.22}$$

where ε_u is the velocity scale over which till transitions from a quasi-linear to Coulomb friction law. The critical failure strength of the till follows the empirical form of Tulaczyk et al. (2000a)

$$\tau_c = \tau_o \exp[-b(e - e_c)], \tag{B.23}$$

where τ_o and b are empirical parameters.

B.1.7 Boundary Conditions

Flotation at the Grounding Line

Ice begins to float at the grounding line ($\sigma = 1$), so the flotation condition must apply

$$\varrho_i h = \varrho_w b \tag{B.24}$$

where, ϱ_i is the density of ice, ϱ_w is the density of water, h is the ice thickness, and b is the bed elevation.

Longitudinal stress is assumed to balance water pressure at the grounding line (Shumskiy and Krass, 1976)

$$\left[2\mathcal{A}^{-\frac{1}{n}} h \left| \frac{\partial u_b}{\partial x} \right|^{\frac{1}{n}-1} \frac{\partial u_b}{\partial x} \right] \Bigg|_{x=x_g} = \frac{1}{2}\varrho_i \left(1 - \frac{\varrho_i}{\varrho_w} \right) g h(x_g)^2. \tag{B.25}$$

Ice Divide

By definition, the upstream boundary ($\sigma = 0$) is the ice divide. Here, we have $u_b = 0$.

Temperature

There are Dirichlet boundary conditions on temperature at the upper and lower ice surfaces

$$T(z = b) = T_{MP} \tag{B.26}$$

$$T(z = b + h) = T_s \tag{B.27}$$

where T_{MP} is the melting point of ice and T_s is a prescribed ice surface temperature.

At the up- and downstream boundaries, we have set zero Neumann boundary conditions

$$\left.\frac{\partial T}{\partial x}\right|_{x=0} = \left.\frac{\partial T}{\partial x}\right|_{x=x_g} = 0 \tag{B.28}$$

B.2 Numerics

Keep in mind that we use τ (without a subscript) in this section to indicate time. It is a placeholder in the transformed coordinate system, though we still say that $\tau = t$.

B.2.1 Horizontal Velocity

Following Schoof (2006a), we use a variational approach to calculate horizontal velocity at the bed. The key difference here is that we have replaced the resolved lateral velocity variation with the integrated form of Dupont and Alley (2005) in our momentum balance (equation B.3). We also remind the reader that τ_d is defined as in equation B.4. To obtain the weak variational form, we start by multiplying the momentum balance by a test function, q

$$q\partial_x\left(2h\nu\partial_x u\right) - G_s h u^{\frac{1}{n}} q - \tau_b(u,\ldots)q - \tau_d q = 0. \tag{B.29}$$

Integrating over the domain (in dimensional coordinates)

$$\int_0^{x_g}\left[q\partial_x\left(2h\nu\partial_x u\right) - G_s h u^{\frac{1}{n}} q - \tau_b(u,\ldots)q - \tau_d q\right] dx = 0, \tag{B.30}$$

and then integrating by parts in the first term

$$\int_0^{x_g} q\partial_x\left(2h\nu\partial_x u\right) dx = \int_0^{x_g} -2h\nu\partial_x u\partial_x q dx + 2qh\nu\partial_x u\big|_0^{x_g}. \tag{B.31}$$

If the test function q satisfies zero dirichlet conditions where u has Dirichlet conditions ($u(x=0)=0$), then: $q(x=0)=0$. So

$$2qhv\partial_x u|_0^{x_g} = 2qhv\partial_x u|_{x=x_g} \tag{B.32}$$

where we know the RHS from our stress condition at the downstream boundary (equation B.25). This term can now be written as

$$T_f q = \frac{1}{2}\varrho_i\left(1-\frac{\varrho_i}{\varrho_w}\right)gh^2 q. \tag{B.33}$$

Now, substituting back into equation B.30, we arrive at the weak variational form

$$\int_0^{x_g}\left[-2hv\partial_x u\partial_x q dx - G_s h u^{\frac{1}{n}} q - \tau_b(u,\ldots)q - \tau_d q\right]dx + T_f q = 0. \tag{B.34}$$

This gives a continuous functional of the form (now re-expanding the effective viscosity)

$$J(u) = -T_f u(x_g) + \int_0^{x_g}\left[\frac{2h\bar{B}}{\frac{1}{n}+1}\left|\frac{\partial u}{\partial x}\right|^{\frac{1}{n}+1} + \frac{G_s}{\frac{1}{n}+1}h|u|^{\frac{1}{n}+1} + \int_0^u \tau_b(u',\ldots)du' + \tau_d u\right]dx \tag{B.35}$$

We assume that u varies piecewise linearly between nodes, and calculate the integrals over nonlinear functions of u using a composite trapezoidal rule

$$J(u_i) = -T_f u_N + \sum_{i=1}^{N-1}\left[\frac{2}{\frac{1}{n}+1}\left(\frac{h_i\bar{B}_i + h_{i+1}\bar{B}_{i+1}}{2}\right)\left|\frac{u_{i+1}-u_i}{x_{i+1}-x_i}\right|^{\frac{1}{n}+1} + \right.$$
$$\left.\frac{G_s}{\frac{1}{n}+1}\left(\frac{h_i|u_i|^{\frac{1}{n}+1} + h_{i+1}|u_{i+1}|^{\frac{1}{n}+1}}{2}\right) + \int_0^u\left(\frac{\tau_b(u_i',\ldots)+\tau_b(u_{i+1}',\ldots)}{2}\right)du' + \tau_d\left(\frac{u_i+u_{i+1}}{2}\right)\right] \tag{B.36}$$

The resulting minimization problem is straightforward to solve using a Newton method with a Brent-type line search algorithm (Press et al., 1988).

B.2.2 Ice Thickness

To discretize the ice thickness ODE (equation B.12), we upwind the effective velocity $u - \sigma \dot{x}_g$. We use a regularized Heavyside function to switch the direction of upwinding depending on the sign of the effective velocity. The resulting discretization looks like

$$\Delta\sigma \frac{h_i^{k+1} - h_i^k}{\Delta\tau} + \left[\frac{\bar{u}^k_{i+\frac{1}{2}} - \sigma_{i+\frac{1}{2}}(x_g^{k+1} - x_g^k)/\Delta\tau}{x_g^{k+1}} \right] \left[h^{k+1}_{i+1} \left(1 - \vartheta^k_{i+\frac{1}{2}} \right) + h_i^{k+1} \vartheta^k_{i+\frac{1}{2}} \right] - \left[\frac{\bar{u}^k_{i-\frac{1}{2}} - \sigma_{i-\frac{1}{2}}(x_g^{k+1} - x_g^k)/\Delta\tau}{x_g^{k+1}} \right] \left[h^{k+1}_{i-1} \vartheta^k_{i-\frac{1}{2}} + h_i^{k+1} \left(1 - \vartheta^k_{i-\frac{1}{2}} \right) \right] + \frac{h_i^{k+1}}{\Delta\tau} \left(1 - \frac{x_g^k}{x_g^{k+1}} \right) \Delta\sigma = a\left(\sigma_i, x_g^{k+1} \right) \Delta\sigma \quad \text{(B.37)}$$

We evaluate ϑ using the previous time step to avoid non-convergence of a Newton scheme due to the large derivatives of H when the effective advection velocity $u - \sigma \dot{x}_g$ changes direction (at the expense of a few more iterations in the solver in the rare case when the effective velocity switches direction - typically during activation). ϑ is a regularized Heavyside function looking like

$$\vartheta^k_{i+\frac{1}{2}} = \frac{1}{2} \left[1 - \tanh \left(u^k_{i+\frac{1}{2}} - \sigma_{i+\frac{1}{2}} \left(\frac{x_g^k - x_g^{k-1}}{\Delta\tau} \right) \right) \right] \quad \text{(B.38)}$$

In using a backward Euler scheme, we have nonlinear terms in h^{k+1} and x_g^{k+1}. Thus, we utilize a straightforward Newton scheme to solve simultaneously for ice thickness and grounding line position at each time step.

B.2.3 Ice Temperature

Temperature can be discretized in much the same fashion as ice thickness, though here we have not adopted a finite volume form. We use upwinding schemes in both x and z

$$\begin{aligned}
&\frac{T_{i,j}^{k+1} - T_{i,j}^{k}}{\Delta\tau} + \left[\frac{u_{i+\frac{1}{2},j}^{k+1} - \sigma_{i+\frac{1}{2}}(x_g^{k+1} - x_g^{k})/\Delta\tau}{x_g^{k+1}\Delta\sigma}\right]\left[T_{i+1,j}^{k+1}\left(1 - \vartheta_{i+\frac{1}{2}}^{k}\right) + T_{i,j}^{k+1}\vartheta_{i+\frac{1}{2}}^{k}\right] \\
&\qquad - \left[\frac{u_{i-\frac{1}{2},j}^{k+1} - \sigma_{i-\frac{1}{2}}(x_g^{k+1} - x_g^{k})/\Delta\tau}{x_g^{k+1}\Delta\sigma}\right]\left[T_{i-1,j}^{k+1}\vartheta_{i-\frac{1}{2}}^{k} + T_{i,j}^{k+1}\left(1 - \vartheta_{i-\frac{1}{2}}^{k}\right)\right] + \\
&\left[w_{i,j+\frac{1}{2}}^{k+1} - \eta_{j+\frac{1}{2}}\left\{\frac{h_i^{k+1} - h_i^{k}}{\Delta\tau} + \left(\frac{u_{i,j+\frac{1}{2}}^{k+1} - \sigma_i(x_g^{k+1} - x_g^{k})/\Delta\tau}{x_g^{k+1}}\right)\left(\frac{h_{i+1}^{k+1} - h_{i-1}^{k+1}}{2\Delta\sigma}\right)\right\}\right] \times \\
&\qquad \left[T_{i,j+1}^{k+1}\left(1 - \vartheta'^{k}_{i,j+\frac{1}{2}}\right) + T_{i,j}^{k+1}\vartheta'^{k}_{i,j+\frac{1}{2}}\right] + \\
&\left[w_{i,j-\frac{1}{2}}^{k+1} - \eta_{j-\frac{1}{2}}\left\{\frac{h_i^{k+1} - h_i^{k}}{\Delta\tau} + \left(\frac{u_{i,j-\frac{1}{2}}^{k+1} - \sigma_i(x_g^{k+1} - x_g^{k})/\Delta\tau}{x_g^{k+1}}\right)\left(\frac{h_{i+1}^{k+1} - h_{i-1}^{k+1}}{2\Delta\sigma}\right)\right\}\right] \times \\
&\qquad \left[T_{i,j}^{k+1}\left(1 - \vartheta'^{k}_{i,j-\frac{1}{2}}\right) + T_{i,j-1}^{k+1}\vartheta'^{k}_{i,j-\frac{1}{2}}\right] + \frac{T_{i,j}^{k+1}}{\Delta\tau}\left(1 - \frac{x_g^{k}}{x_g^{k+1}}\right) + \\
&\frac{1}{h_i^{k+1}}\left[\frac{h_i^{k+1} - h_i^{k}}{\Delta\tau} + \left(\frac{u_{i,j}^{k+1} - \sigma_i(x_g^{k+1} - x_g^{k})/\Delta\tau}{x_g^{k+1}}\right)\left(\frac{h_{i+1}^{k+1} - h_{i-1}^{k+1}}{2\Delta\sigma}\right)\right] = \frac{\varkappa}{h_i}\left(\frac{T_{i,j-1} - 2T_{i,j} + T_{i,j+1}}{\Delta\eta}\right).
\end{aligned} \tag{B.39}$$

Note the introduction of another Heavyside function here, ϑ', for which the operative variable is the vertical effective velocity (equation B.18).

As this system of equations is linear in temperature, it can be solved in a straightforward fashion.

B.2.4 Till Water Content

The basic form of the evolution equation involves only local meltwater production without lateral transport. We use a forward Euler method to allow for enthalpy corrections to be made at grid

points that are transitioning from meltwater production to till freezing and vice-versa. We begin by discretizing the equations B.20 and B.21

$$Z_{s,i}^{k}\frac{e'^{k+1}_{i}-e_{i}^{k}}{\Delta\tau}=\begin{cases} m & \text{if } e_{i}^{k}>e_{c} \\ m & \text{if } e_{i}^{k}=e_{c} \text{ and } Z_{s,i}^{k}=Z_{o} \text{ and } m>0 \\ 0 & \text{otherwise} \end{cases} \tag{B.40}$$

$$e_{i}^{k}\frac{Z'^{k+1}_{s,i}-Z_{s,i}^{k}}{\Delta\tau}=\begin{cases} m & \text{if } e_{i}^{k}=e_{c} \text{ and } 0<Z_{s,i}^{k}<Z_{o} \\ m & \text{if } e_{i}^{k}=e_{c} \text{ and } Z_{s,i}^{k}=Z_{o} \text{ and } m<0 \\ 0 & \text{otherwise} \end{cases} \tag{B.41}$$

Here we have introduced a prime notation on void ratio and till thickness that indicates these variables have not yet been corrected for crossing over thresholds. We do not want to overshoot and make $e<e_{c}$ or $Z_{s}>Z_{o}$. The corrected cases are based on the idea that we would like to take the change past a threshold in one variable and translate to a change from a threshold in another variable. To do so, we start with the following equality

$$Z_{o}\frac{e'-e_{c}}{\Delta\tau}=e_{c}\frac{Z'_{s}-Z_{o}}{\Delta\tau} \tag{B.42}$$

If $Z'_{s}>Z_{o}$, then we need to translate this extra change to a change in e', which we can solve for

$$e'=e_{c}\left(\frac{Z'_{s}}{Z_{o}}\right). \tag{B.43}$$

If $e'<e_{c}$, then we need to translate this extra change to a change in Z'_{s}, which we can solve for

$$Z'_{s}=Z_{o}\left(\frac{e'}{e_{c}}\right) \tag{B.44}$$

We can write these into case-by-case corrections

$$e_i^{k+1} = \begin{cases} e_c & \text{if } e'^{k+1}_i < e_c \\ e_c \left(\frac{Z'^{k+1}_{s,i}}{Z_o} \right) & \text{if } Z'^{k+1}_{s,i} > Z_o \\ e'^{k+1}_i & \text{otherwise} \end{cases} \tag{B.45}$$

$$Z_{s,i}^{k+1} = \begin{cases} Z_o \left(\frac{e'^{k+1}_i}{e_c} \right) & \text{if } e'^{k+1}_i < e_c \\ Z_o & \text{if } Z'^{k+1}_{s,i} > Z_o \\ Z'^{k+1}_{s,i} & \text{otherwise} \end{cases} \tag{B.46}$$

B.2.5 Discretization

In this model, the grid is staggered in the horizontal. Most variables which are only defined in the x direction (h, e, Z_s) are located on the elements. Horizontal velocity u, is defined on grid box corners. T is defined on grid box centers. w is defined on grid box edges.

Thickness at the grounding line is used in order to maintain the flotation condition at the outer boundary. However, because thickness is defined on elements in our discretization scheme, we must add an additional equation to solve for thickness and grounding line position simultaneously (as detailed in section B.2.2. Ice thickness in the two grid points near the grounding line is relaxed to the grounding line thickness (which is determined through the flotation condition)

$$h_{GL} = \frac{1}{2} h_{N-\frac{1}{2}} - \frac{3}{2} h_{N-\frac{3}{2}}. \tag{B.47}$$

This approach is also described in the appendix of Schoof (2007a).

B.2.6 Horizontal Grid Refinement

The approach we have taken here allows us to define an arbitrary mesh in $\sigma - \eta$ space. For simplicity, we use equally-spaced η coordinates.

As Schoof (2007a) has shown, in order to accurately simulate transient grounding line migration, we must resolve the mechanical grounding zone transition from ice sheet to ice shelf flow. The σ coordinates are correspondingly refined in a fashion similar to Schoof (2007a), by defining a grounding zone in sigma (here we use $\sigma \in [0.97\ \ 1]$) where the resolution is high (~100 m). In most of the ice stream not in the grounding zone a lower resolution is used. We explore the convergence of solutions in increasing upstream resolution in section 3.3.

B.3 Comparison to Robel et al. 2013 (Figure 1)

In order to make a valid comparison between the flowline model described here and that described in chapter 2, we need to be able to map parameters between both models. In the case of most parameters (see table of parameters in both studies), this is fairly straightforward. For some parameters there is no direct translation between models.

In chapter 2, there is an ice stream length, L, which does not translate to this model, which has a migrating grounding line. Here we will assume that ice stream length is the grounding line position in the steady-streaming regime, before oscillations are induced $L = 770$ km. This remains within about 15% of the grounding line position during oscillations.

In chapter 2, there is an ice stream width, W, which is not explicitly set in this model. However, we do use an ice stream half-width of $W = 25$ km to set the lateral shear stress parameter, $G_s = 400$, and so we use this as a comparison to chapter 2. Additionally, we note that the Glen's flow law coefficient, A_g that shows up in both chapter 2 and G_s are both taken in the shear margins, so we set them to $A_g = 2.7 \times 10^{-24}$ Pa^{-3} s^{-1}, appropriate for temperate shear margins.

The one parameter (with dynamical significance) that does not have an equivalent between these two studies is bed slope, b_x. Chapter 2 assumes that the ice stream rests on a flat bed. Setting a flat bed in this study would lead the implicit thickness solver to find non-unique solutions for the grounding line position. As such we must have some non-zero bed slope. This study only includes simulations with bedslope $b_x = 5 \times 10^{-4}$. In order to adapt the analytic prediction of stability boundary location from chapter 2 (refer to appendix A), we can add a bed slope term, α, into the driving stress scaling

$$[\tau_d] = \varrho_i g [h] \left(\frac{[h]}{L} + \alpha \right). \tag{B.48}$$

We use the same steady-state balance between accumulation and mass loss from ice streaming: $a_c L = [h][u_b]$, which leads to an equation for the thickness scale

$$a_c L = \frac{A_g W^{n+1} [h]}{4^n (n+1)} \left[\frac{\varrho_i g [h]}{L} \left(1 + \frac{\alpha L}{[h]} \right) \right]^n. \tag{B.49}$$

This does not permit an exact closed-form solution for $[h]$ as before, so we solve numerically for $[h]$ for the purposes of this comparison.

Though we have numerically solved for exact $[h]$ to produce Figure 1 of this study, there are perturbation methods for developing closed-form approximations for the case when α is small. We start with the following form for the approximation (dropping brackets)

$$h(\alpha) \approx h_0 + h_1 \alpha + h_2 \alpha^2. \tag{B.50}$$

We plug this into equation B.49 and start by setting $\alpha = 0$, and deriving the same zero-slope approximation that is in equation 12 of the supplementary material of chapter 2

$$h_0 = L \left[\frac{A_g W^{n+1} \left(\varrho_i g \right)^n}{4^n (n+1) a_c} \right]^{-\frac{1}{n+1}}. \tag{B.51}$$

We then expand equation B.49, canceling the terms corresponding to the $\alpha = 0$ approximation, and then retaining terms in α^1

$$0 = Q\left[4h_0^3 h_1 \alpha + 3\alpha L h_0^3\right]. \tag{B.52}$$

Solving for h_1 gives

$$h_1 = -\frac{3L}{4}. \tag{B.53}$$

Moving onto the second order approximation, we return to the expanded version of B.49, retaining only terms in α^2

$$0 = Q\left[4h_0^3 h_2 \alpha^2 + 6h_0^2 h_1^2 \alpha^2 + 3\alpha L\left(3h_0^2 h_1 \alpha\right) + 3\alpha^2 L^2 h_0^2\right]. \tag{B.54}$$

Solving for h_2

$$h_2 = \frac{3}{32}\frac{L^2}{h_0}. \tag{B.55}$$

These give the following second-order approximation for h

$$h \approx h_0 - \frac{3L}{4}\alpha + \frac{3}{32}\frac{L^2}{h_0}\alpha^2, \tag{B.56}$$

which gives an approximation that is less than 1% from the exact solution for the parameters used in this study. We can then plug this into our approximation for the stability boundary location.

References

Abe-Ouchi, A., Saito, F., Kawamura, K., Raymo, M. E., Okuno, J., Takahashi, K., and Blatter, H. (2013). Insolation-driven 100,000-year glacial cycles and hysteresis of ice-sheet volume. *Nature*, 500(7461):190–193.

Albrecht, T., Martin, M., Haseloff, M., Winkelmann, R., and Levermann, A. (2011). Parameterization for subgrid-scale motion of ice-shelf calving fronts. *The Cryosphere*, 5(1):35–44.

Alley, R., Blankenship, D., Bentley, C., and Rooney, S. (1986). Deformation of till beneath ice stream B, West Antarctica. *Nature*, 322(6074):57–59.

Alley, R. B., Anandakrishnan, S., Dupont, T. K., Parizek, B. R., and Pollard, D. (2007). Effect of sedimentation on ice-sheet grounding-line stability. *Science*, 315(5820):1838–1841.

Alley, R. B. and Clark, P. U. (1999). The deglaciation of the northern hemisphere: A global perspective. *Annual Review of Earth and Planetary Sciences*, 27:149–182.

Anandakrishnan, S. and Alley, R. (1997). Stagnation of ice stream C, West Antarctica by water piracy. *Geophys. Res. Lett.*, 24(3):265–268.

Anandakrishnan, S., Alley, R., Jacobel, R., and Conway, H. (2001). The flow regime of ice stream c and hypotheses concerning its recent stagnation. *The West Antarctic Ice Sheet: Behavior and Environment*, pages 283–296.

Anandakrishnan, S., Catania, G., Alley, R., and Horgan, H. (2007). Discovery of till deposition at the grounding line of Whillans Ice Stream. *Science*, 315(5820):1835–1838.

Andrews, J., Barry, R., Bradley, R., Miller, G., and Williams, L. (1972). Past and present glaciological responses to climate in eastern baffin island. *Quaternary Research*, 2(3):303–314.

Andrews, J. and Maclean, B. (2003). Hudson Strait ice streams: a review of stratigraphy, chronology and links with North Atlantic Heinrich events. *Boreas*, 32(1):4–17.

Austermann, J., Mitrovica, J. X., Latychev, K., and Milne, G. A. (2013). Barbados-based estimate of ice volume at last glacial maximum affected by subducted plate. *Nature geoscience*, 6(7):553–557.

Bamber, J., Vaughan, D., and Joughin, I. (2000). Widespread complex flow in the interior of the Antarctic ice sheet. *Science*, 287(5456):1248–1250.

Bard, E., Hamelin, B., and Fairbanks, R. G. (1990). U-th ages obtained by mass spectrometry in corals from barbados: sea level during the past 130, 000 years. *Nature*, 346(6283):456–458.

Bender, C. M. and Orszag, S. A. (1978). *Advanced mathematical methods for scientists and engineers*. McGraw-Hill.

Bennett, M. (2003). Ice streams as the arteries of an ice sheet: their mechanics, stability and significance. *Earth Science Reviews*, 61(3-4):309–339.

Bindschadler, R., Harrison, W. D., Raymond, C. F., and Gantet, C. (1976). Thermal regime of a surge-type glacier. *Journal of Glaciology*, 16(74).

Bindschadler, R. A., King, M. A., Alley, R. B., Anandakrishnan, S., and Padman, L. (2003). Tidally controlled stick-slip discharge of a west antarctic ice stream. *Science*, 301(5636):1087–1089.

Blankenship, D., Bentley, C., Rooney, S., and Alley, R. (1986). Seismic measurements reveal a saturated porous layer beneath an active Antarctic ice stream. *Nature*, 322(6074):54–57.

Blatter, H. (1995). Velocity and stress fields in grounded glaciers - a simple algorithm for including deviatoric stress gradients. *J. Glaciol.*, 41.

Bougamont, M., Price, S., Christoffersen, P., and Payne, A. (2011). Dynamic patterns of ice stream flow in a 3-D higher-order ice sheet model with plastic bed and simplified hydrology. *Journal of Geophysical Research-Earth Surface*, 116.

Bougamont, M., Tulaczyk, S., and Joughin, I. (2003a). Numerical investigations of the slowdown of Whillans Ice Stream, West Antarctica: Is it shutting down like Ice Stream C? *Ann. Glaciol.*, 37(1):239–246.

Bougamont, M., Tulaczyk, S., and Joughin, I. (2003b). Response of subglacial sediments to basal freeze-on: 2. Application in numerical modeling of the recent stoppage of Ice Stream C, West Antarctica. *J. Geophys. Res.*, 108(B4):2223.

Briner, J. P., Bini, A. C., and Anderson, R. S. (2009). Rapid early holocene retreat of a laurentide outlet glacier through an arctic fjord. *Nature Geoscience*, 2(7):496–499.

Broecker, W. S. and Denton, G. H. (1989). The role of ocean-atmosphere reorganizations in glacial cycles. *Geochim. Cosmochim. Acta*, 53:2465–2501.

Budyko, M. I. (1969). The effect of solar radiation variations on the climate of the earth. *Tellus*, 21:611–619.

Bueler, E. and Brown, J. (2009). Shallow shelf approximation as a "sliding law" in a thermomechanically coupled ice sheet model. *J. Geophys. Res.*, 114:F03008.

Calov, R., Ganapolski, A., Petoukhov, V., Claussen, M., and Greve, R. (2002). Large-scale instabilities of the Laurentide ice sheet simulated in a fully coupled climate-system model. *Geophys. Res. Lett.*, 29(24).

Calov, R., Greve, R., Abe-Ouchi, A., E, B., Huybrechts, P., Johnson, J., Pattyn, F., Pollard, D., Ritz, C., Saito, F., and Tarasov, L. (2010). Results from the Ice-Sheet Model Intercomparison Project?Heinrich Event INtercOmparison (ISMIP HEINO). *J. Glaciol.*, 56(197):371–383.

Catania, G., Conway, H., CF, R., and Scambos, T. (2005). Surface morphology and internal layer stratigraphy in the downstream end of Kamb Ice Stream, West Antarctica. *J. Glaciol.*, 51(174):423–431.

Catania, G., Hulbe, C., and Conway, H. (2010). Grounding-line basal melt rates determined using radar-derived internal stratigraphy. *J. Glaciol.*, 56(197):545–554.

Catania, G., Hulbe, C., Conway, H., Scambos, T., and CF, R. (2012). Variability in the mass flux of the Ross ice streams, West Antarctica, over the last millennium. *J. Glaciol.*, 58(210):741–752.

Christianson, K., Parizek, B. R., Alley, R. B., Horgan, H. J., Jacobel, R. W., Anandakrishnan, S., Keisling, B. A., Craig, B. D., and Muto, A. (2013). Ice sheet grounding zone stabilization due to till compaction. *Geophysical Research Letters*, 40(20):5406–5411.

Christoffersen, P. and Tulaczyk, S. (2003). Response of subglacial sediments to basal freeze-on 1. Theory and comparison to observations from beneath the West Antarctic Ice Sheet. *Journal of Geophysical Research*, 108(B4).

Christoffersen, P., Tulaczyk, S., and Behar, A. (2010). Basal ice sequences in antarctic ice stream: Exposure of past hydrologic conditions and a principal mode of sediment transfer. *Journal of Geophysical Research: Earth Surface (2003–2012)*, 115(F3).

Chugunov, V. A. and Wilchinsky, A. V. (1996). Modelling of a marine glacier and ice-sheet–ice shelf transition zone based on asymptotic analysis. *Annals of Glaciology*, 23:59–67.

Clark, P. U., Alley, R. B., and Pollard, D. (1999). Northern hemisphere ice-sheet influences on global climate change. *Science*, 286(5442):1104–1111.

Clarke, G. (1976). Thermal Regulation of Glacier Surging. *J. Glaciol.*, 16(74):231–250.

Cornford, S. L., Martin, D. F., Graves, D. T., Ranken, D. F., Le Brocq, A. M., Gladstone, R. M., Payne, A. J., Ng, E. G., and Lipscomb, W. H. (2013). Adaptive mesh, finite volume modeling of marine ice sheets. *Journal of Computational Physics*, 232(1):529–549.

Cutler, P. M., MacAyeal, D. R., Mickelson, D. M., Parizek, B. R., and Colgan, P. M. (2000). A numerical investigation of ice-lobe–permafrost interaction around the southern laurentide ice sheet. *Journal of Glaciology*, 46(153):311–325.

Docquier, D., Pollard, D., and Pattyn, F. (2014). Thwaites glacier grounding-line retreat: influence of width and buttressing parameterizations. *Journal of Glaciology*, 60(220):305.

Dowdeswell, J., Ottesen, D., Evans, J., Cofaigh, C., and Anderson, J. (2008). Submarine glacial landforms and rates of ice-stream collapse. *Geology*, 36:819–822.

Dunse, T., Greve, R., Schuler, T., and Hagen, J. (2011). Permanent fast flow versus cyclic surge behaviour: numerical simulations of the Austfonna ice cap, Svalbard. *J. Glaciol.*, 57(202):247–259.

Dupont, T. and Alley, R. (2005). Assessment of the importance of ice-shelf buttressing to ice-sheet flow. *Geophys. Res. Lett.*, 32(L04503).

Dupont, T. K. and Alley, R. B. (2006). Role of small ice shelves in sea-level rise. *Geophysical Research Letters*, 33(9).

Durand, G., Gagliardini, O., De Fleurian, B., Zwinger, T., and Le Meur, E. (2009). Marine ice sheet dynamics: Hysteresis and neutral equilibrium. *Journal of Geophysical Research: Earth Surface (2003–2012)*, 114(F3).

Echelmayer, K., Harrison, W., Larsen, C., and Mitchell, J. (1994). The role of the margins in the dynamics of an active ice stream. *J. Glaciol.*, 40(136):527–538.

Echelmeyer, K., Harrison, W., Larsen, C., and Mitchell, J. (1994). The role of the margins in the dynamics of an active ice stream. *J. Glaciol.*, 40:527–538.

Engelhardt, H., Humphrey, N., Kamb, B., and Fahnestock, M. (1990). Physical conditions at the base of a fast moving Antarctic ice stream. *Science*, 248(4951):57–59.

Engelhardt, H. and Kamb, B. (1993). Vertical temperature profile of Ice Stream B. *Antarctic Journal of the US*, 28(5):63–66.

Engelhardt, H. and Kamb, B. (1997). Basal hydraulic system of a West Antarctic ice stream: constraints from borehole observations. *J. Glaciol.*, 43(144):207–230.

Fahnestock, M., Scambos, T., Bindschadler, R., and Kvaran, G. (2000). A millennium of variable ice flow recorded by the Ross Ice Shelf, Antarctica. *J. Glaciol.*, 46(155):652–664.

Fatland, D. and Lingle, C. (1998). Analysis of the 1993-5 Bering Glacier (Alaska) surge using differential SAR interferometry. *J. Glaciol.*, 45:532–546.

Favier, L., Durand, G., Cornford, S., Gudmundsson, G., Gagliardini, O., Gillet-Chaulet, F., Zwinger, T., Payne, A., and Le Brocq, A. (2014). Retreat of pine island glacier controlled by marine ice-sheet instability. *Nature Climate Change*.

Forel, F.-A. (1895). *L'éboulement du glacier de l'Altels*.

Fowler, A. (1987). A theory of glacial surges. *Journal of Geophysical Research-Solid Earth and Planets*, 92(B9):9111–9120.

Fowler, A. and Johnson, C. (1996). Ice-sheet surging and ice-stream formation. *Annals of glaciology*, 23:68–73.

Fowler, A. and Larson, D. (1978). On the flow of polythermal glaciers. i. model and preliminary analysis. In *Proceedings of the Royal Society of London A: Mathematical, Physical and Engineering Sciences*, volume 363, pages 217–242. The Royal Society.

Fowler, A., Murray, T., and Ng, F. (2001). Thermally controlled glacier surging. *J. Glaciol.*, 47(159):527–538.

Fowler, A. and Schiavi, E. (1998). A theory of ice-sheet surges. *J. Glaciol.*, 44(146):104–118.

Fricker, H., Scambos, T., Bindschadler, R., and Padman, L. (2007). An active subglacial water system in West Antarctica Mapped from space. *Science*, 315:1544–1548.

Fried, M., Hulbe, C., and Fahnestock, M. (2014). Grounding-line dynamics and margin lakes. *Ann. Glaciol.*, 55(56):87–96.

Ganopolski, A. and Calov, R. (2011). The role of orbital forcing, carbon dioxide and regolith in 100 kyr glacial cycles. *Climate of the Past*, 7(4):1415–1425.

Ganopolski, A., Calov, R., and Claussen, M. (2010). Simulation of the last glacial cycle with a coupled climate ice-sheet model of intermediate complexity. *Climate of the Past*, 6(2):229–244.

Ghil, M. (1994). Cryothermodynamics: the chaotic dynamics of paleoclimate. *Physica D*, 77:130–159.

Ghil, M. and Treut, H. L. (1981). A climate model with cryodynamics and geodynamics. *J. Geophys. Res.*, 86:5262–5270.

Gildor, H. and Tziperman, E. (2000). Sea ice as the glacial cycles climate switch: role of seasonal and orbital forcing. *Paleoceanography*, 15:605–615.

Gildor, H., Tziperman, E., and Toggweiler, R. J. (2002). The sea-ice switch mechanism and glacial-interglacial CO_2 variations. *Global Biogeochem. Cycles*, 16:10.1029/ 2001GB001446.

Glen, J. (1955). The creep of polycrystalline ice. *Proceedings of the Royal Society of London Series A-Mathematical and Physical Sciences*, 228(1175):519–538.

Goldberg, D., Holland, D., and Schoof, C. (2009). Grounding line movement and ice shelf buttressing in marine ice sheets. *J. Geophys. Res.*, 114(F04026).

Golledge, N. R., Fogwill, C. J., Mackintosh, A. N., and Buckley, K. M. (2012). Dynamics of the last glacial maximum antarctic ice-sheet and its response to ocean forcing. *Proceedings of the National Academy of Sciences*, 109(40):16052–16056.

Gomez, N., Mitrovica, J. X., Huybers, P., and Clark, P. U. (2010a). Sea level as a stabilizing factor for marine-ice-sheet grounding lines. *Nature Geoscience*, 3(12):850–853.

Gomez, N., Mitrovica, J. X., Huybers, P., and Clark, P. U. (2010b). Sea level as a stabilizing factor for marine-ice-sheet grounding lines. *Nature Geoscience*, 3(12):850–853.

Gomez, N., Pollard, D., Mitrovica, J. X., Huybers, P., and Clark, P. U. (2012). Evolution of a coupled marine ice sheet–sea level model. *Journal of Geophysical Research: Earth Surface (2003–2012)*, 117(F1).

Gow, A., Ueda, H., and Garfield, D. (1968). Antarctic ice sheet: preliminary results of first core hole to bedrock. *Science*, 161(3845):1011–1013.

Graham, A., Larter, R., Gohl, K., Dowdeswell, J., Hillenbrand, C., JA, S., Evans, J., Kuhn, G., and Deen, T. (2010). Flow and retreat of the Late Quaternary Pine Island-Thwaites palaeo-ice stream, West Antarctica. *J. Geophys. Res.*, 115(F03025).

Greenberg, J. and Shyong, W. (1990). Surging glacial flows. *IMA journal of applied mathematics*, 45(3):195–223.

Gregoire, L. J., Payne, A. J., and Valdes, P. J. (2012). Deglacial rapid sea level rises caused by ice-sheet saddle collapses. *Nature*, 487(7406):219–222.

Greve, R. and Blatter, H. (2009). *Dynamics of ice sheets and glaciers*. Springer Science & Business Media.

Gudmundsson, G., Krug, J., Durand, G., Favier, L., and Gagliardini, O. (2012). The stability of grounding lines on retrograde slopes. *The Cryosphere*, 6(4):2597–2619.

Gudmundsson, G. H. (2006). Fortnightly variations in the flow velocity of rutford ice stream, west antarctica. *Nature*, 444(7122):1063–1064.

Hays, J. D., Imbrie, J., and Shackleton, N. J. (1976). Variations in the earth's orbit: Pacemakers of the ice ages. *Science*, 194:1121–1132.

Heinrich, H. (1988). Origin and consequences of cyclic ice rafting in the Northeast Atlantic Ocean during the past 130,000 years. *Quat. Res.*, 29:142–152.

Hemming, S. R. (2004). Heinrich events: Massive late pleistocene detritus layers of the north atlantic and their global climate imprint. *Rev. Geophys.*, 42(1).

Herterich, K. (1987). On the flow within the transition zone between ice sheet and ice shelf. In van der Veen, C. and Oerlemans, J., editors, *Dynamics of the West Antarctic ice sheet*, Dordrecht. D. Reidel.

Hinch, E. (1991). *Perturbation Methods*. Cambridge University Press.

Hindmarsh, R. and Le Meur, E. (2001). Dynamical processes involved in the retreat of marine ice sheets. *J. Glaciol.*, 47(157):271–282.

Hindmarsh, R. C. A. (2009). Consistent generation of ice-streams via thermo-viscous instabilities modulated by membrane stresses. *Geophys. Res. Lett.*, 36.

Hoffmann, J. and Clarke, G. (1973). Periodic temperature instabilities in sub-polar glaciers. *IN: THE ROLE OF SNOW AND ICE IN HYDROLOGY*.

Hollin, J. T. (1962). On the glacial history of antarctica. *Journal of Glaciology*, 4:172–195.

Horgan, H. and Anandakrishnan, S. (2006). Static grounding lines and dynamic ice streams: Evdience from the Siple Coast, West Antarctica. *Geophys. Res. Lett.*, 33(L18502).

Howat, I. M., Joughin, I., Tulaczyk, S., and Gogineni, S. (2005). Rapid retreat and acceleration of helheim glacier, east greenland. *Geophysical Research Letters*, 32(22).

Hughes, T. (1973). Is the west antarctic ice sheet disintegrating? *Journal of Geophysical Research*, 78(33):7884–7910.

Hulbe, C. and Fahnestock, M. (2004). West Antarctic ice-stream discharge variability: mechanism, controls and pattern of grounding-line retreat. *J. Glaciol.*, 50(171):471–484.

Hulbe, C. and Fahnestock, M. (2007). Century-scale discharge stagnation and reactivation of the Ross ice streams, West Antarctica. *Journal of Geophysical Research-Earth Surface*, 112(F3).

Hulbe, C. and Whillans, I. (1997). Weak bands within Ice Stream B, West Antarctica. *J. Glaciol.*, 43(145):377–386.

Huybers, P. (2007). Glacial variability over the last two million years: an extended depth-derived agemodel, continuous obliquity pacing, and the pleistocene progression. *Quaternary Science Reviews*, 26(1-2):37–55.

Huybers, P. and Tziperman, E. (2008). Integrated summer insolation controls 40,000 year glacial cycles in an ice-sheet energy-balance model. *Paleoceanography*, 23:PA1208, doi:10.1029/2007PA001463.

Huybrechts, P. (1996). Basal temperature conditions of the greenland ice sheet during the glacial cycles. *Annals of Glaciology*, 23:226–236.

Hyde, W. T. and Peltier, W. R. (1987). Sensitivity experiments with a model of the ice-age cycle: The response to milankovitch forcing. *J. Atmos. Sci.*, 44(10):1351–1374.

Imbrie, J., Berger, A., Boyle, E. A., Clemens, S. C., Duffy, A., Howard, W. R., Kuklas, G., Kutzbach, J., Martinson, D. G., McIntyre, A., Mix, A. C., Molfino, B., Morley, J. J., Peterson, L. C., Pisias, N. G., Prell, W. L., Raymo, M. E., Shackleton, N. J., and Toggweiler, J. R. (1993). On the structure and origin of major glaciation cycles 2. the 100,000–year cycle. *Paleoceanog.*, 8:699–735.

Jackson, M. and Kamb, B. (1997). The marginal shear stress of Ice Stream B, West Antarctica. *J. Glaciol.*, 43:415–426.

Jamieson, S., Vieli, A., Livingstone, S., Cofaigh, C., Stokes, C., Hillenbrand, C., and Dowdeswell, J. (2012). Ice-stream stability on a reverse bed slope. *Nature Geoscience*, 5(11):799–802.

Jamieson, S. S., Vieli, A., Cofaigh, C. Ó., Stokes, C. R., Livingstone, S. J., and Hillenbrand, C.-D. (2014). Understanding controls on rapid ice-stream retreat during the last deglaciation of marguerite bay, antarctica, using a numerical model. *Journal of Geophysical Research: Earth Surface*, 119(2):247–263.

Jiskoot, H., Murray, T., and Boyle, P. (2000). Controls on the distribution of surge-type glaciers in svalbard. *Journal of Glaciology*, 46(154):412–422.

Joughin, I., Alley, R. B., and Holland, D. M. (2012). Ice-sheet response to oceanic forcing. *Science*, 338(6111):1172–1176.

Joughin, I., Binschadler, R., King, M., Voigt, D., Alley, R., Anandakrishnan, S., Horgan, H., Peters, L., Winberry, P., Das, S., and G, C. (2005). Continued deceleration of Whillans Ice Stream, West Antarctica. *Geophys. Res. Lett.*, 32:L22501.

Joughin, I., Gray, L., Bindschadler, R., Price, S., Morse, D., Hulbe, C., Mattar, K., and Werner, C. (1999). Tributaries of west antarctic ice streams revealed by radarsat interferometry. *Science*, 286(5438):283–286.

Joughin, I., Howat, I. M., Fahnestock, M., Smith, B., Krabill, W., Alley, R. B., Stern, H., and Truffer, M. (2008). Continued evolution of jakobshavn isbrae following its rapid speedup. *Journal of Geophysical Research: Earth Surface (2003–2012)*, 113(F4).

Joughin, I., Smith, B. E., and Holland, D. M. (2010). Sensitivity of 21st century sea level to ocean-induced thinning of Pine Island Glacier, Antarctica. *Geophysical Research Letters*, 37(20).

Joughin, I., Smith, B. E., and Medley, B. (2014). Marine ice sheet collapse potentially under way for the thwaites glacier basin, west antarctica. *Science*, 344(6185):735–738.

Joughin, I. and Tulaczyk, S. (2002). Positive mass balance of the Ross ice stream, West Antarctica. *Science*, 295:476–452.

Joughin, I., Tulaczyk, S., Bamber, J. L., Blankenship, D., Holt, J. W., Scambos, T., and Vaughan, D. G. (2009). Basal conditions for pine island and Thwaites Glaciers, West Antarctica, determined using satellite and airborne data. *Journal of Glaciology*, 55(190):245–257.

Joughin, I., Tulaczyk, S., MacAyeal, D., and Engelhardt, H. (2004). Melting and freezing beneath the Ross ice streams, Antarctica. *J. Glaciol.*, 50(168):96–108.

Kamb, B. and Echelmeyer, K. A. (1986). Stress-gradient coupling in glacier flow: I. longitudinal averaging of the influence of ice thickness and surface slope. *Journal of Glaciology*, 32(111):267–284.

Kamb, B., Raymond, C., Harrison, W., Engelhardt, H., Echelmeyer, K., Humphrey, N., Brugman, M., and Pfeffer, T. (1985). Glacier surge mechanism: 1982–1983 surge of variegated glacier, alaska. *Science*, 227(4686):469–479.

Katz, R. and Worster, M. (2010). Stability of ice-sheet grounding lines. *Proc. R. Soc. A*.

Kleman, J. and Applegate, P. (2013). Durations and propagation patterns of ice sheet instability events. *Quat. Sci. Rev.*, page http://dx.doi.org/10.1016/j.quascirev.2013.07.030.

Kyrke-Smith, T., Katz, R., and Fowler, A. (2013). Subglacial hydrology and the formation of ice streams. *Proc. R. Soc. A*.

Kyrke-Smith, T., Katz, R., and Fowler, A. (2015). Subglacial hydrology as a control on emergence, scale and spacing of ice streams. *Journal of Geophysical Research: Earth Surface*.

Li, C., Battisti, D. S., Schrag, D. P., and Tziperman, E. (2005). Abrupt climate shifts in greenland due to displacements of the sea ice edge. *Geophys. Res. Lett.*, 32(19).

Lingle, C. and Brown, T. (1987). A subglacial aquifer bed model and water pressure dependent basal sliding relationship for a West Antarctic ice stream. In van der Veen, C. and Oerlemans, J., editors, *Dynamics of the West Antarctic Ice Sheet*. D. Reidel.

Livingstone, S., Cofaigh, C., Stokes, C., Hillenbrand, C., Vieli, A., and Jamieson, S. (2012). Antarctic palaeo-ice streams. *Earth-Science Reviews*, 111:90–128.

Luthra, T., Alley, R., and Anadakrishnan, S. (2013). Seismic imaging of former grounding lines beneath Whillans Ice Stream, West Antarctica. *AGU Abstract*, C33B-0719.

MacAyeal, D. (1989). Large-Scale Ice Flow Over a Viscous Basal Sediment - Theory and Application to Ice Stream B, Antarctica. *Journal of Geophysical Research-Solid Earth and Planets*, 94(B4):4071–4087.

MacAyeal, D. (1993). Binge/purge oscillations of the laurentide ice sheet as a cause of the north atlantic heinrich events. *Paleoceanography*, 8(6):775–784.

Marcott, S. A., Clark, P. U., Padman, L., Klinkhammer, G. P., Springer, S. R., Liu, Z., Otto-Bliesner, B. L., Carlson, A. E., Ungerer, A., Padman, J., et al. (2011). Ice-shelf collapse from subsurface warming as a trigger for heinrich events. *Proceedings of the National Academy of Sciences*, 108(33):13415–13419.

Margold, M., Stokes, C. R., and Clark, C. D. (2015). Ice streams in the laurentide ice sheet: Identification, characteristics and comparison to modern ice sheets. *Earth-Science Reviews*, 143:117–146.

Marshall, S. J. and Clark, P. U. (2002). Basal temperature evolution of north american ice sheets and implications for the 100-kyr cycle. *Geophysical Research Letters*, 29(24):67–1.

Marshall, S. J. and Clarke, G. K. C. (1997). A continuum mixture model of ice stream thermomechanics in the laurentide ice sheet .2. application to the hudson strait ice stream. *J. Geophys. Res.*, 102(B9):20615–20637.

Mercer, J. (1978). West antarctic ice sheet and co2 greenhouse effect: a threat of disaster. *Nature*, 27:26.

Mercer, J. H. (1968). Antarctic ice and sangamon sea level. *IAHS Publ.*, 179.

Morland, L. (1987). Unconfined ice-shelf flow. In van der Veen, C. and Oerlemans, J., editors, *Dynamics of the West Antarctic Ice Sheet*. D. Reidel, Boston.

Mosola, A. B. and Anderson, J. B. (2006). Expansion and rapid retreat of the west antarctic ice sheet in eastern ross sea: possible consequence of over-extended ice streams? *Quaternary Science Reviews*, 25(17-18):2177 – 2196.

Nick, F., Vieli, A., Howat, I., and Joughin, I. (2009). Large-scale changes in Greenland outlet glacier dynamics triggered at the terminus. *Nature Geoscience*, 2(2):110–114.

Nye, J. (1957). The distribution of stress and velocity in glaciers and ice-sheets. In *Proceedings of the Royal Society of London A: Mathematical, Physical and Engineering Sciences*, volume 239, pages 113–133. The Royal Society.

O'Brien, P., Santis, L. D., Harris, P., Domack, E., and Quilty, P. (1999). Ice shelf grounding zone features of western prydz bay, antarctica: sedimentary processes from seismic and sidescan images. *Antarctic Science*, 11:78–91.

Oerlemans, J. (1980). Model Experiments on the 100,000-yr Glacial Cycle. *Nature*, 287(5781):430–432.

Oerlemans, J. (1982a). Glacial cycles and ice-sheet modeling. *Clim. Change*, 4:353–374.

Oerlemans, J. (1982b). Glacial cycles and ice-sheet modelling. *Climatic Change*, 4(4):353–374.

Oerlemans, J. (2002). On glacial inception and orography. *Quaternary International*, 95:5–10.

Oerlemans, J. (2003). A quasi-analytical ice-sheet model for climate studies. *Nonlinear processes in geophysics*, 10(4/5):441–452.

Paillard, D. (1998). The timing of Pleistocene glaciations from a simple multiple-state climate model. *Nature*, 391:378–381.

Papa, B., Mysek, L., and Wang, Z. (2006). Intermittent ice sheet discharge events in northeastern North America during the last glacial period. *Clim. Dyn.*, 26:201–206.

Parizek, B., Christianson, K., Anandakrishnan, S., Alley, R., Walker, R., Edwards, R., Wolfe, D., Bertini, G., Rinehart, S., Bindschadler, R., et al. (2013). Dynamic (in) stability of Thwaites Glacier, West Antarctica. *Journal of Geophysical Research: Earth Surface*, 118(2):638–655.

Pattyn, F. (2002). Transient glacier response with a higher-order numerical ice-flow model. *J. Glaciol.*, 48.

Pattyn, F., Schoof, C., Perichon, L., Hindmarsh, R., Bueler, E., Fleurian, B. d., Durand, G., Gagliardini, O., Gladstone, R., Goldberg, D., et al. (2012). Results of the marine ice sheet model intercomparison project, mismip. *The Cryosphere*, 6(3):573–588.

Payne, A. (1995). Limit cycles in the basal thermal regime of ice sheets. *J. Geophys. Res.*, 100(B3):4249–4263.

Payne, A. and Dongelmans, P. (1997). Self-organization in the thermomechanical flow of ice sheets. *Journal of Geophysical Research: Solid Earth (1978–2012)*, 102(B6):12219–12233.

Payne, A. J., Vieli, A., Shepherd, A. P., Wingham, D. J., and Rignot, E. (2004). Recent dramatic thinning of largest west antarctic ice stream triggered by oceans. *Geophysical Research Letters*, 31(23).

Peltier, W. and Marshall, S. (1995). Coupled energy-balance/ice-sheet model simulations of the glacial cycles: a possible connection between terminations and terrigenous dust. *J. Geophys. Res.*, 100:14,269–14,289.

Perol, T. and Rice, J. R. (2015). Shear heating and weakening of the margins of west antarctic ice streams. *Geophysical Research Letters*.

Pfeffer, W., Dyurgerov, M., Kaplan, M., Dwyer, J., Sassolas, C., Jennings, A., Raup, B., and Manley, W. (1997). Numerical modeling of late glacial laurentide advance of ice across hudson strait: Insights into terrestrial and marine geology, mass balance, and calving flux. *Paleoceanography*, 12(1):97–110.

Pollard, D. (1978). An investigation of the astronomical theory of the ice ages using a simple climate-ice sheet model. *Nature*, 272(5650):233–235.

Pollard, D. (1982). A simple ice sheet model yields realistic 100 kyr glacial cycles. *Nature*, 296:334–338.

Pollard, D. and DeConto, R. (2009). Modelling West Antarctic ice sheet growth and collapse through the past five million years. *Nature*, 458(7236):329–332.

Pollard, D. and DeConto, R. M. (2005). Hysteresis in cenozoic antarctic ice-sheet variations. *Global and Planetary Change*, 45(1):9–21.

Pollard, D., DeConto, R. M., and Alley, R. B. (2015). Potential antarctic ice sheet retreat driven by hydrofracturing and ice cliff failure. *Earth and Planetary Science Letters*, 412:112–121.

Press, W., Teukolsky, S., Vetterline, W., and Flannery, B. (1988). *Numerical Recipes in C*. Cambridge university press.

Price, S., Conway, H., Waddington, E., and Bindschadler, R. (2008). Model investigations of inland propagation of fast-flowing outlet glaciers and ice streams. *J. Glaciol.*, 54(184):49–60.

Pritchard, H. D., Arthern, R. J., Vaughan, D. G., and Edwards, L. A. (2009). Extensive dynamic thinning on the margins of the greenland and antarctic ice sheets. *Nature*, 461(7266):971–975.

Raymond, C. (1996). Shear margins in glaciers and ice sheets. *J. Glaciol.*, 42(140):90–102.

Raymond, C. (2000). Energy balance of ice streams. *J. Glaciol.*, 46(155):665–674.

Rempel, A. (2007). A theory for ice-till interaction and sediment entrainment beneath glaciers. *J. Geophys. Res.*, 113:F01009, 1–17, doi:10.1029/2010JF001839.

Retzlaff, R. and Bentley, C. (1993). Timing of stagnation of Ice Stream C, West Antarctica, from short pulse radar studies of buried surface crevasses. *J. Glaciol.*, 39(133):553–561.

Rignot, E., Bamber, J., van den Broeke, M., Davis, C., Li, Y., van de Berg, W., and van Meijgaard, E. (2008). Recent Antarctic ice mass loss from radar interferometry and regional climate modeling. *Nature Geoscience*, 1(2):106–110.

Rignot, E., Mouginot, J., and Scheuchl, B. (2011a). Antarctic grounding line mapping from differential satellite radar interferometry. *Geophys. Res. Lett.*, 38(L10504).

Rignot, E., Mouginot, J., and Scheuchl, B. (2011b). Ice flow of the antarctic ice sheet. *Science*, 333(6048):1427–1430.

Robel, A., DeGiuli, E., Schoof, C., and Tziperman, E. (2013). Dynamics of ice stream temporal variability: Modes, scales and hysteresis. *J. Geophys. Res.*, 118:925–936.

Robel, A., Schoof, C., and Tziperman, E. (2014). Rapid grounding line migration induced by internal ice stream variability. *J. Geophys. Res.*, 119:2430–2447.

Robin, G. d. Q. (1955). Ice movement and temperature distribution in glaciers and ice sheets. *Journal of Glaciology*, 2(18):523–532.

Robison, R. A., Huppert, H. E., and Worster, M. (2010). Dynamics of viscous grounding lines. *Journal of Fluid Mechanics*, 648:363–380.

Rose, K. (1979). Characteristics of ice flow in Marie Byrd Land, Antarctica. *J. Glaciol.*, 24(90):63–75.

Sayag, R. and Tziperman, E. (2009). Spatiotemporal dynamics of ice streams due to a triple valued sliding law. *J. Fluid Mech.*, 640:483–505.

Sayag, R. and Tziperman, E. (2011). Interaction and variability patterns of ice streams under a triple-valued sliding law and a non-newtonian rheology. *J. Geophys. Res.*, 116:F01009, 1–17, doi:10.1029/2010JF001839.

Schmeltz, M., Rignot, E., Dupont, T. K., and Macayeal, D. R. (2002). Sensitivity of Pine Island Glacier, West Antarctica, to changes in ice-shelf and basal conditions: a model study. *Journal of Glaciology*, 48(163):552–558.

Schofield, A. and Wroth, P. (1968). *Critical state soil mechanics*. McGraw-Hill London.

Schoof, C. (2004). Bed topography and surges in ice streams. *Geophys. Res. Lett.*, 31(6).

Schoof, C. (2006a). A variational approach to ice stream flow. *J. Fluid Mech.*, 556:227–251.

Schoof, C. (2006b). Variational methods for glacier flow over plastic till. *J. Fluid Mech.*, 555:299–320.

Schoof, C. (2007a). Ice sheet grounding line dynamics: Steady states, stability, and hysteresis. *Journal of Geophysical Research - Earth Surface*, 112(F3).

Schoof, C. (2007b). Marine ice-sheet dynamics. Part 1. The case of rapid sliding. *J. Fluid Mech.*, 573:27–55.

Schoof, C. (2010). Ice-sheet acceleration driven by melt supply variability. *Nature*, 468(7325):803–806.

Schoof, C. (2012a). Marine ice sheet stability. *Journal of Fluid Mechanics*, 698:62–72.

Schoof, C. (2012b). Thermally driven migration of ice-stream shear margins. *Journal of Fluid Mechanics*, 712:552–578.

Schoof, C. (2012c). Thermally driven migration of ice-stream shear margins. *Journal of Fluid Mechanics*, 712:552–578.

Schroeder, D. M., Blankenship, D. D., and Young, D. A. (2013). Evidence for a water system transition beneath Thwaites Glacier, West Antarctica. *Proceedings of the National Academy of Sciences*, 110(30):12225–12228.

Shabtaie, S. and Bentley, C. (1987). West Antarctic ice stream draining into the Ross Ice Shelf: Configuration and mass balance. *J. Geophys. Res.*, 92(B2):1311–1336.

Shaw, J., Piper, D., Fader, G., King, E., Todd, B., Bell, T., Batterson, M., and Liverman, D. (2006). A conceptual model of the deglaciation of atlantic canada. *Quaternary Science Reviews*, 25(17):2059–2081.

Shumskiy, P. and Krass, M. (1976). Mathematical models of ice shelves. *J. Glaciol.*, 17(77):419–432.

Smith, A. M., Jordan, T. A., Ferraccioli, F., and Bingham, R. G. (2013). Influence of subglacial conditions on ice stream dynamics: Seismic and potential field data from Pine Island Glacier, West Antarctica. *Journal of Geophysical Research: Solid Earth*, 118(4):1471–1482.

Stearns, L. A., Smith, B. E., and Hamilton, G. S. (2008). Increased flow speed on a large East Antarctic outlet glacier caused by subglacial floods. *Nature Geoscience*, 1(12):827–831.

Stephens, B. B. and Keeling, R. (2000). The influence of Antarctic sea ice on glacial-interglacial CO_2 variations. *Nature*, 404:171–174.

Stevens, L. A., Behn, M. D., McGuire, J. J., Das, S. B., Joughin, I., Herring, T., Shean, D. E., and King, M. A. (2015). Greenland supraglacial lake drainages triggered by hydrologically induced basal slip. *Nature*, 522(7554):73–76.

Stokes, C. and Clark, C. (2001). Palaeo-ice streams. *Quat. Sci. Rev.*, 20(13):1437–1457.

Stokes, C. R., Clark, C. D., and Storrar, R. (2009). Major changes in ice stream dynamics during deglaciation of the north-western margin of the laurentide ice sheet. *Quaternary Science Reviews*, 28(7):721–738.

Stokes, C. R. and Tarasov, L. (2010). Ice streaming in the Laurentide Ice Sheet: A first comparison between data-calibrated numerical model output and geological evidence. *Geophysical Research Letters*, 37(1).

Stokes, C. R., Tarasov, L., and Dyke, A. S. (2012). Dynamics of the north american ice sheet complex during its inception and build-up to the last glacial maximum. *Quaternary Science Reviews*, 50:86–104.

Strogatz, S. (1994). *Nonlinear dynamics and chaos*. Westview Press.

Suckale, J., Platt, J. D., Perol, T., and Rice, J. R. (2014). Deformation-induced melting in the margins of the west antarctic ice streams. *Journal of Geophysical Research: Earth Surface*, 119(5):1004–1025.

Swithinbank, C. (1954). Ice streams. *Polar Record*, 7(48):185–186.

Tarasov, L. and Peltier, W. R. (2004). A geophysically constrained large ensemble analysis of the deglacial history of the north american ice-sheet complex. *Quaternary Science Reviews*, 23(3):359–388.

Thomas, R., Stephenson, S., Bindschadler, R., Shabtaie, S., and Bentley, C. (1988). Thinning and Grounding-Line Retreat on Ross Ice Shelf Antractica. *Ann. Glaciol.*, 11:165–172.

Timmermann, R., Wang, Q., and Hellmer, H. (2012). Ice-shelf basal melting in a global finite-element sea-ice/ice-shelf/ocean model. *Annals of Glaciology*, 53(60):303–314.

Toggweiler, J. R. (1999). Variation of atmospheric CO_2 by ventilation of the ocean's deepest water. *Paleoceanography*, 14:572–588.

Truffer, M., Echelmeyer, K. A., and Harrison, W. D. (2001). Implications of till deformation on glacier dynamics. *Journal of Glaciology*, 47(156):123–134.

Tsai, V. C. and Gudmundsson, G. H. (2015). An improved model for tidally modulated grounding-line migration. *Journal of Glaciology*, 61(226).

Tsai, V. C., Rice, J. R., and Fahnestock, M. (2008). Possible mechanisms for glacial earthquakes. *Journal of Geophysical Research: Earth Surface (2003–2012)*, 113(F3).

Tsai, V. C., Stewart, A. L., and Thompson, A. F. (2015). Marine ice-sheet profiles and stability under coulomb basal conditions. *Journal of Glaciology*, 61(226):205–215.

Tulaczyk, S., Kamb, W., and Engelhardt, H. (2000a). Basal mechanics of Ice Stream B, West Antarctica 1. Till mechanics. *Journal of Geophysical Research-Solid Earth*, 105(B1):463–481.

Tulaczyk, S., Kamb, W., and Engelhardt, H. (2000b). Basal mechanics of Ice Stream B, West Antarctica 2. Undrained plastic bed model. *Journal of Geophysical Research-Solid Earth*, 105(B1):483–494.

Tziperman, E., Raymo, M., Huybers, P., and Wunsch, C. (2006). Consequences of pacing the pleistocene 100 kyr ice ages by nonlinear phase locking to milankovitch forcing. *Paleoceanography*, 21(PA4206):doi:10.1029/2005PA001241.

Ullman, D. J., Carlson, A. E., Anslow, F. S., LeGrande, A. N., and Licciardi, J. M. (2015). Laurentide ice-sheet instability during the last deglaciation. *Nature Geoscience*.

van der Veen, C. and Whillans, I. (1996). Model experiments on the evolution and stability of ice streams. *Ann. Glaciol.*, 232:129–137.

van der Veen, C. J., Plummer, J., and Stearns, L. (2011). Controls on the recent speed-up of jakobshavn isbræ, west greenland. *Journal of Glaciology*, 57(204):770–782.

van der Wel, N., Christoffersen, P., and Bougamont, M. (2013). The influence of subglacial hydrology on the flow of Kamb Ice Stream, West Antarctica. *J. Geophys. Res.*, 118:1–14.

Van Pelt, W. and Oerlemans, J. (2012). Numerical simulations of cyclic behaviour in the Parallel Ice Sheet Model (PISM). *J. Glaciol.*, 58(208):347–360.

Vieli, A. and Payne, A. (2005). Assessing the ability of numerical ice sheet models to simulate grounding line migration. *J. Geophys. Res.*, 110:F01003.

Vogel, S., Tulaczyk, S., Kamb, B., Engelhardt, H., Carsey, F., Behar, A., Lane, A., and Joughin, I. (2005). Subglacial conditions during and after stoppage of an Antarctic Ice Stream: Is reactivation imminent? *Geophys. Res. Lett.*, 32(14).

Weertman, J. (1961). Stability of ice-age ice sheets. *Journal of Geophysical Research*, 66(11):3783–3792.

Weertman, J. (1974). Stability of the junction of an ice sheet and an ice shelf. *J. Glaciol.*, 13:3–11.

Wiggins, S. (2003). *Introduction to Applied Nonlinear Dynamical Systems and Chaos*. Springer.

Wilchinsky, A. V. (2001). Studying ice sheet stability using the method of separation of variables. *Geophysical & Astrophysical Fluid Dynamics*, 94(1-2):15–45.

Wilchinsky, A. V. (2009). Linear stability analysis of an ice sheet interacting with the ocean. *Journal of Glaciology*, 55(189):13–20.

Winberry, J., Anandakrishnan, S., and Alley, R. (2009). Seismic observations of transient subglacial water-flow beneath MacAyeal Ice Stream, West Antarctica. *Geophys. Res. Lett.*, 36.

Wingham, D. J., Ridout, A. J., Scharroo, R., Arthern, R. J., and Shum, C. (1998). Antarctic elevation change from 1992 to 1996. *Science*, 282(5388):456–458.

Winsborrow, M. C., Stokes, C. R., and Andreassen, K. (2012). Ice-stream flow switching during deglaciation of the southwestern barents sea. *Geological Society of America Bulletin*, 124(3-4):275–290.

Zweck, C. and Huybrechts, P. (2005). Modeling of the northern hemisphere ice sheets during the last glacial cycle and glaciological sensitivity. *Journal of Geophysical Research: Atmospheres (1984–2012)*, 110(D7).

This thesis was typeset using LaTeX, originally developed by Leslie Lamport and based on Donald Knuth's TeX. The body text is set in 12 point Egenolff-Berner Garamond, a revival of Claude Garamont's humanist typeface. The above illustration, "Science Experiment 02", was created by Ben Schlitter and released under CC BY-NC-ND 3.0. A template that can be used to format a PhD thesis with this look and feel has been released under the permissive MIT (X11) license, and can be found online at github.com/suchow/Dissertate or from its author, Jordan Suchow, at suchow@post.harvard.edu.